NATIONAL TECHNICAL UNIVERSITY OF ATHENS

SCHOOL OF NAVAL ARCHITECTURE
& MARINE ENGINEERING

DIPLOMA THESIS

Heat transfer enhancement in three-dimensional flow past a circular cylinder using surface hydrophobicity

IOANNIS POLITIS

Thesis Committee:

Supervisor: L. Kaiktsis, Associate Professor N.T.U.A.
Members: C.I. Papadopoulos, Assistant Professor N.T.U.A.
G. Papalambrou, Assistant Professor N.T.U.A.

Athens, June 2018

ΕΘΝΙΚΟ ΜΕΤΣΟΒΙΟ ΠΟΛΥΤΕΧΝΕΙΟ

ΣΧΟΛΗ ΝΑΥΠΗΓΩΝ ΜΗΧΑΝΟΛΟΓΩΝ
ΜΗΧΑΝΙΚΩΝ

ΔΙΠΛΩΜΑΤΙΚΗ ΕΡΓΑΣΙΑ

Ενίσχυση της μεταφοράς θερμότητας στην τριδιάστατη ροή γύρω από κύλινδρο με χρήση επιφανειακής υδροφοβικότητας

ΙΩΑΝΝΗΣ ΠΟΛΙΤΗΣ

Εξεταστική Επιτροπή:

Επιβλέπων: Λ. Καϊκτσής, Αναπληρωτής Καθηγητής Ε.Μ.Π.
Μέλη: Χ.Ι. Παπαδόπουλος, Επίκουρος Καθηγητής Ε.Μ.Π.
Γ. Παπαλάμπρου, Επίκουρος Καθηγητής Ε.Μ.Π.

Αθήνα, Ιούνιος 2018

Acknowledgment

First l, I would like to thank my supervisor and mentor, Associate Professor L. Kaiktsis, for his guidance and support in the course this study.

Also, I would like thank Dr. M. Mastrokalos, for his guidance and instructions on several issues, including the thesis preparation. Without his knowledge of thermofluids and technical support on the computational tools, the completion of the present study would not have been possible.

Finally, I want to thank Mr. A. Charitopoulos, for his willingness to solve immediately all problems related to the computer hardware.

Abstract

Flows past bluff bodies have been studied extensively, due to their significance in the fields of construction and engineering. Typical structures behaving as bluff bodies are skyscrapers, chimneys, offshore pipelines and oil risers. On the other hand, typical engineering devices including bluff bodies are heat exchangers. A main objective in designing such devices is to eliminate the time-dependent forces acting on the bodies, which may lead to structural failure due to fatigue. In heat transfer applications, a main objective is evidently heat transfer enhancement.

The goal of the present study is to study computationally the flow and heat transfer rates in flow past a circular cylinder whose surface is maintained at a constant temperature, using Computational Fluid Dynamics (CFD). It is known from literature studies that implementation of hydrophobicity on the cylinder surface results in the suppression of wake unsteadiness and in heat transfer enhancement. However, the majority of these studies are limited to two-dimensional flow, at low values of Reynolds number. Thus, the present study considers the fully three-dimensional problem, and investigates the effects of implementing different patterns of surface hydrophobicity on flow structure, on the forces acting on the cylinder, and on heat transfer. Here, the low Reynolds number regime is considered, under the assumption of constant fluid thermophysical properties.

First, an extensive parametric analysis is performed concerning the effects of spatial and temporal discretization parameters, as well as of domain size, on the accuracy of results, and a combination of these parameters is selected corresponding to sufficient numerical accuracy at an acceptable computational cost.

In a first stage, surface hydrophobicity is applied on the entire cylinder surface. The results verify a simultaneous suppression of flow unsteadiness and enhancement of heat transfer. The effects are intensified at increasing value of slip length, and become weak in the range of high values of slip length.

Next, in order to investigate whether a proper reduction in control effort could lead to equivalent flow state and heat transfer rates with those corresponding to a fully hydrophobic cylinder, alternating circumferential hydrophobic and non-hydrophobic bands are implemented on the cylinder surface. The computational results demonstrate that proper implementation of hydrophobicity can lead to substantial reduction of forces acting on the cylinder, in comparison to the case of non-hydrophobic cylinder, and an increase in heat transfer rate.

Finally, the effects of implementing partial, spanwise uniform, hydrophobicity are investigated. It is found that proper selection of the spatial distribution of hydrophobicity increases both flow stability and heat transfer rates, in comparison to the to the case of non-hydrophobic cylinder, at a reduced cost of passive control.

Περίληψη

Οι ροές γύρω από μη υδροδυναμικά σώματα είναι αντικείμενο πλήθους μελετών, εξαιτίας της ευρείας εφαρμογής τους στα πεδία των κατασκευών και της μηχανολογίας. Τυπικές κατασκευές που συμπεριφέροντα ως μη υδροδυναμικά σώματα είναι οι ουρανοξύστες, οι καμινάδες, οι θαλάσσιοι αγωγοί και οι αγωγοί άντλησης πετρελαίου. Από την άλλη πλευρά, τυπικές μηχανολογικές συσκευές που περιλαμβάνουν μη υδροδυναμικά σώματα είναι οι εναλλάκτες θερμότητας. Ο κύριος σκοπός των σχετικών μελετών είναι η ελαχιστοποίηση της δυναμικής φόρτισης των σωμάτων, η οποία μπορεί να οδηγήσει σε κατασκευαστική αστοχία λόγω κόπωσης, και η ενίσχυση της μεταφοράς θερμότητας σε εφαρμογές εναλλακτών θερμότητας.

Η παρούσα εργασία αφορά στον χαρακτηρισμό του ροϊκού πεδίου και της μετάδοσης θερμότητας στη ροή γύρω από κύλινδρο η επιφάνεια του οποίου διατηρείται σε σταθερή θερμοκρασία, με χρήση Υπολογιστικής Ρευστοδυναμικής. Είναι γνωστό από πρόσφατες σχετικές μελέτες ότι εφαρμογή υδροφοβικότητας στην επιφάνεια του κυλίνδρου έχει ως αποτέλεσμα τον περιορισμό της αστάθειας στον ομόρρου και την ενίσχυση της μεταφοράς θερμότητας. Ωστόσο, η πλειοψηφία των σχετικών μελετών περιορίζεται στη μελέτη της διδιάστατης ροής, για χαμηλές τιμές του αριθμού Reynolds. Έτσι, στην παρούσα εργασία μελετάται υπολογιστικά το πλήρες τριδιάστατο πρόβλημα, διερευνώντας τις επιπτώσεις της χρήσης επιφανειακής υδροφοβικότητας στη δομή της ροής, στις δυνάμεις που ασκούνται στο σώμα, και στη μεταφορά θερμότητας. Εδώ, μελετάται το πρόβλημα για σχετικά χαμηλές τιμές του αριθμού Reynolds, ενώ οι τιμές των θερμοφυσικών ιδιοτήτων του ρευστού θεωρούνται σταθερές.

Αρχικά, γίνεται μια εκτενής μελέτη της επίδρασης των παραμέτρων της χωρικής και χρονικής διακριτοποίησης, καθώς και του μεγέθους του υπολογιστικού χωρίου, στην ακρίβεια των αποτελεσμάτων. Με βάση τα αποτελέσματα, επιλέγεται ένας κατάλληλος συνδυασμός των σχετικών παραμέτρων, που αντιστοιχεί σε καλή ακρίβεια με ταυτόχρονη διατήρηση του υπολογιστικού κόστους σε αποδεκτά επίπεδα.

Η εφαρμογή υδροφοβικότητας γίνεται αρχικά σε ολόκληρη την επιφάνεια του κυλίνδρου. Τα αποτελέσματα πιστοποιούν τη μείωση της αστάθειας της ροής και την ενίσχυση της μεταφοράς θερμότητας. Η ενίσχυση αυτή αυξάνεται με περαιτέρω αύξηση του μήκους ολίσθησης, και καθίσταται σχετικά μικρή για μεγάλες τιμές του μήκους ολίσθησης.

Στη συνέχεια, με σκοπό να διερευνηθεί εάν η κατάλληλη μείωση της δράσης ελέγχου μπορεί να οδηγήσει σε ισοδύναμη κατάσταση ροής και ρυθμού μεταφοράς θερμότητας με την περίπτωση της πλήρους υδροφοβικότητας, εφαρμόζονται εναλλασσόμενες υδροφοβικές και μη υδροφοβικές λωρίδες στην επιφάνεια του κυλίνδρου. Αποδεικνύεται ότι κατάλληλη χωρική κατανομή της υδροφοβικότητας μπορεί να οδηγήσει σε σημαντική μείωση των δυνάμεων που ασκούνται στον κύλινδρο, σε σύγκριση με την περίπτωση του μη υδροφοβικού κυλίνδρου, και σε αντίστοιχη αύξηση του ρυθμού μεταφοράς θερμότητας.

Τέλος, για τον ίδιο προαναφερθέντα λόγο, διερευνάται η επίδραση της υδροφοβικότητας κατανεμημένης ομοιόμορφα κατά τον άξονα του κυλίνδρου, συμμετρικά περί το εμπρός σημείο ανακοπής. Τα αποτελέσματα δείχνουν ότι κατάλληλη επιλογή της χωρικής κατανομής της υδροφοβικότητας αυξάνει σημαντικά την ευστάθεια της ροής και τους ρυθμούς μεταφοράς θερμότητας, σε σύγκριση με την περίπτωση του μη υδροφοβικού κυλίνδρου.

Table of Contents

List of figures

List of tables

1 Introduction

1.1 Flow past bluff bodies

Flows past bluff bodies are associated with many engineering applications. The term 'bluff body' refers to an object placed to a parallel flow, whose length, measured in the direction of the flow, is of the same order with its width, measured in the direction perpendicular to the flow. In other words, a bluff body is an object whose aspect ratio is close to unity. Typical examples of corresponding structures include skyscrapers, chimneys, offshore pipelines, oil risers and tubes of heat exchangers. Because of their non-aerodynamic shape, placement of these objects to a parallel flow displays a region, downstream to them, termed as 'wake', which exhibits significant slowdown of the flow and simultaneous velocity and pressure fluctuations. These fluctuations are caused by a structure in the wake known as the Karman vortex street. The Karman vortex street is a repeating pattern of vortices, in a row, which have opposite spin two by two, and are generated by the alternating flow separation from the two sides of the body. The latter affects not only the wake but also the object, because it triggers time-dependent forces which may induce oscillations of the structure. If the magnitude of oscillation is high, the structure may undergo failure due to fatigue.

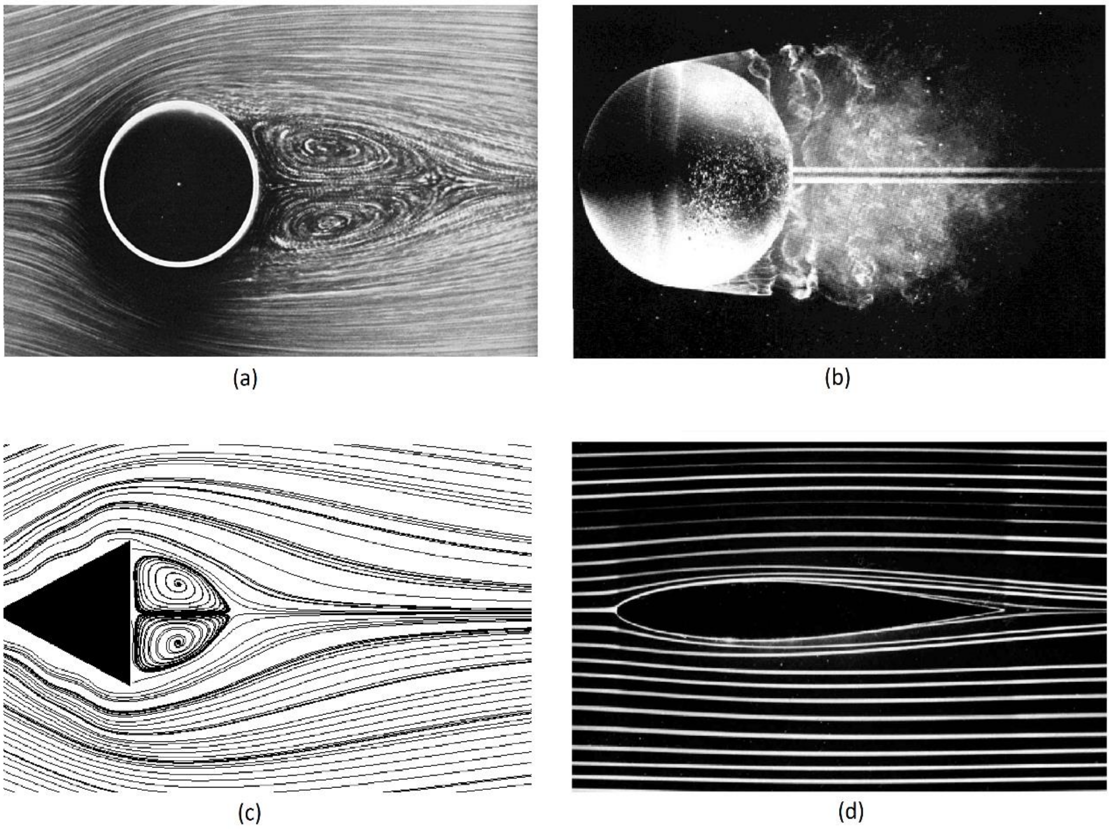

Fig. 1**:** Bluff body prototypes: (a) circular cylinder, (b) sphere, (c) triangular prism. Aerodynamic body: (d) airfoil. (a, b, d Van Dyke 1982, c Shademani et al. 2013.)

Common prototypes of bluff bodies are the circular cylinder, the sphere and the triangular prism (fig.1a-1c). On the other hand, aerodynamic bodies, such as propeller blade and airplane wing (fig.1d), present totally different flow structure because flow follows the geometry of the body to the rear stagnation point, where detached. Therefore, aerodynamic bodies present much smaller drag coefficient, due to relatively lower pressure drag, and the fluid forces acting on the body are constant in time.

1.2 Flow past a circular cylinder

Flow past a circular cylinder has been studied extensively for several decades. This is explained by the fact that cylinder not only has a simple geometry, but also exhibits all the phenomena associated with bluff body flows. In the case of incompressible flow past a very long cylinder, and in the absence of external forces, the only non-dimensional parameter affecting the dynamics is the Reynolds number. Reynolds number, "*Re*", expresses the ratio of inertia forces to viscous forces, and in the case of circular cylinder *Re* is given by the following form:

$$Re = \frac{U_\infty \cdot D}{v} \tag{1}$$

Where:
U_∞: Free steam velocity
D: Cylinder dimeter
v: Kinematic viscosity

In the next sub-sections, an overview of the structure over a wide range of *Re* is presented. In particular, the region of *Re* in which flow transitions from two-dimensional (2-D) to three-dimensional (3-D), is presented in detail, as it is associated with the present study.

1.2.1 Flow structure

As stated before, *Re* is the only parameter affecting the structure of incompressible flow past a circular cylinder. The characteristics of flow in the different flow regimes, corresponding to different values of *Re*, are now well assessed. At low *Re*, the flow remains 2-D and fully stable. As *Re* increases flow continues to be 2-D, but the wake loses its stability, and a time-periodic vortex street is formed. With further increase of *Re* a second instability occurs and the flow becomes 3-D. The wake turns turbulent at higher values of *Re*, followed by the transition of the boundary layer on the cylinder from laminar to turbulent, at even higher Re levels.

In more detail, for *Re*<5, the flow follows the geometry of the cylinder to the rear stagnation point, where it is detached (creeping flow). In the range 5<*Re*<47, the flow continues to be stable, however the separation point is located earlier than the rear stagnation point, forming two symmetrical vortices, also called recirculation zones. The length of these vortices is an increasing linear function of *Re*. For *Re*>47, the recirculation zone develops instabilities which appear initially on the downstream end of the zone. As *Re* increases, these instabilities start moving upstream towards the cylinder, and the associated fluctuation intensities are increased. The presence of instabilities can be observed by the velocity fluctuations in the wake and also by the oscillation of the whole recirculation zone transversely to the flow. As these oscillations continue to increase in amplitude, one of the two vortices is detached from the cylinder, and shed in the wake. When the first vortex is shed, the second one starts increasing its size, until it is its turn to be detached from the cylinder. At the time when one vortex is detached from the cylinder, another one is shaped, on the other side of the cylinder (fig.2). This phenomenon is time-periodic and called vortex shedding. Vortex shedding is thus associated with the creation of a row of vortices travelling downstream, forming the Karman vortex street. The vortices are shed alternatively from the two sides of the cylinder, and one period is completed when one vortex is detached from each side. The frequency "*f*" of vortex shedding is commonly presented in non-dimensional form as the Strouhal number, *St*, defined as follows.

$$St = \frac{f \cdot D}{U_\infty} \tag{2}$$

St is an increasing function of *Re* in the region between *Re*=47 and 180, in which the flow remains 2-D. Due to the extensive research in this region, the *Re-St* curve is well-known. In addition, the results of both experimental and computational works presents very small scatter in this region.

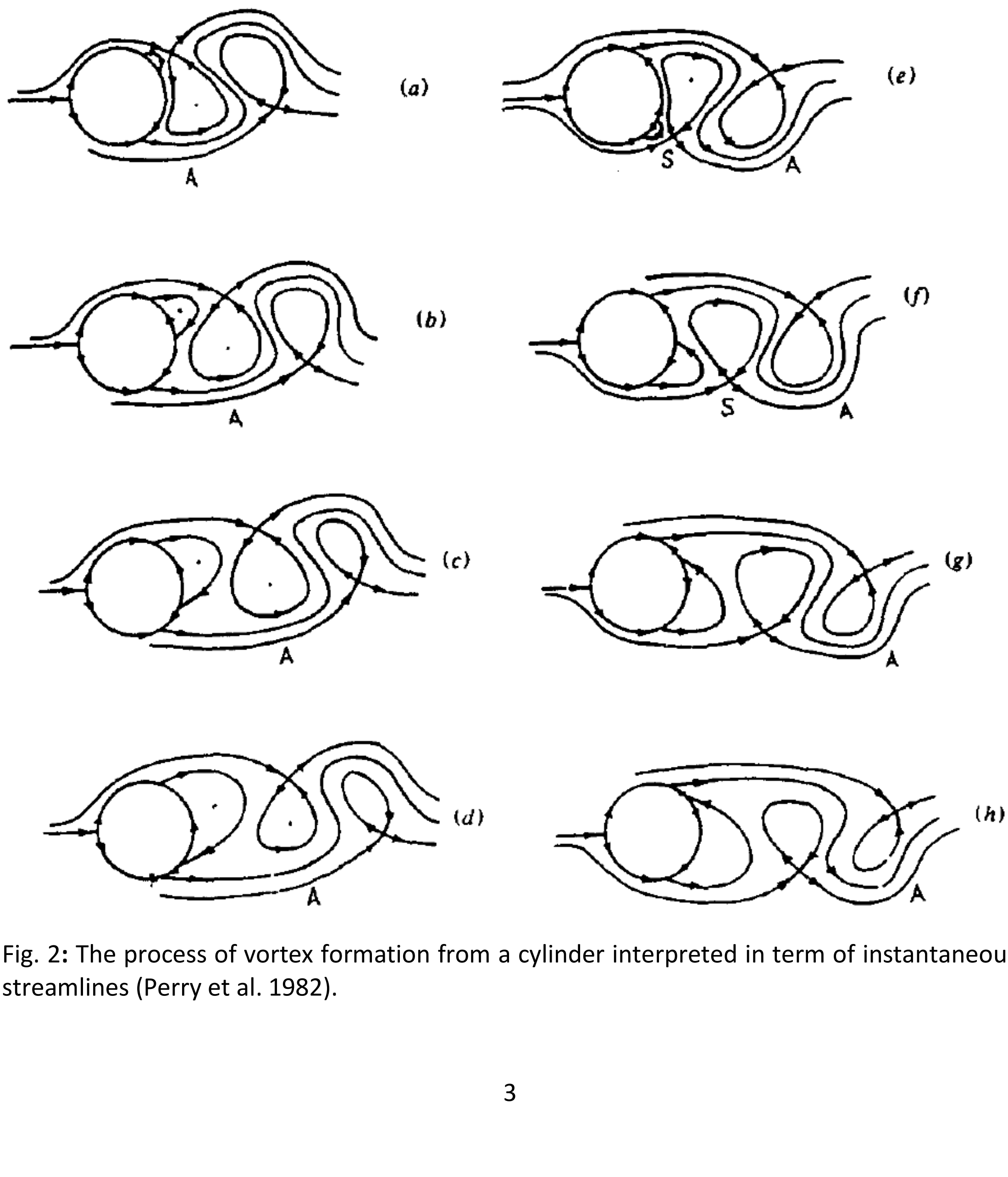

Fig. 2**:** The process of vortex formation from a cylinder interpreted in term of instantaneous streamlines (Perry et al. 1982).

For Re>180 a second instability occurs and the flow becomes 3-D. The wake becomes turbulent at higher values of Re. The three-dimensionality is mainly manifested by two changes in the wake. The first is the deformation of Karman (spanwise) vortices by losing their cylindricality and presenting a wavy pattern. The second change in the wake is the formation of streamwise vortex pairs. This modified, three-dimensional, wake structure is known as *mode A* shedding. Over the range of *Re* from 230 to 260, there is a transition of the wake from *mode A* shedding to *mode B* shedding. The difference between the two modes is mainly the wavelength (spanwise separation) of streamwise rolls, with *mode B* characterized by lower levels of wavelength. For Re>1000 the shear layers emanating from the cylinder become turbulent. Further, at $Re \approx 3.5 \cdot 10^5$ the boundary layer undergoes a transition from laminar to turbulent, resulting in the movement of separation points downstream, and therefore the sharp decrease of drag coefficient (drag crisis). Finally, for $Re > 1.5 \cdot 10^6$ the entire flow field is turbulent. In the next sub-section, a detailed description of the two shedding modes (mode A, mode B) is presented, as they correspond to the regime of the present study.

1.2.1.1 Shedding modes A & B

As stated before, mode A of shedding is the manifestation of the first 3-D instability (fig. 3a). This mode of shedding occurs for Re>180, and is characterized by a discontinuous change in the *Re*-*St* curve (fig.4). This discontinuity is hysteretic, because the critical *Re* at which the flow transitions from 2-D to 3-D depends on whether the flow speed is increased or decreased. As regards the flow structure, the primary (Karman) vortices acquire a wavy form, while the streamwise vortex pairs have wavelength “λ_Z” of about 3 to 4 cylinder diameters. Nonetheless, the reported values of wavelength have a large scatter, both for experimental and computational results, and one of the reasons for this scatter is the appearance of vortex dislocations. The formation of wavy pattern and vortex loops in Karman vortices is due to the shedding process on cylinder. In more detail, the creation and the shedding of vortices stop being spanwise independent because elliptical spots of earlier vortex formation appear. This results in the displacement of primary vortices upstream towards the cylinder at this point. As the vortex stretched upstream part of the vorticity pulled back to the cylinder forming a vortex loop. In addition, the deformation of Karman vortices as they shed results in the creation of streamwise vortex pairs. A streamwise vortex is located between two primary vortices, and follows a staggered arrangement as one vortex has opposite vorticity from the next one (fig.3a).

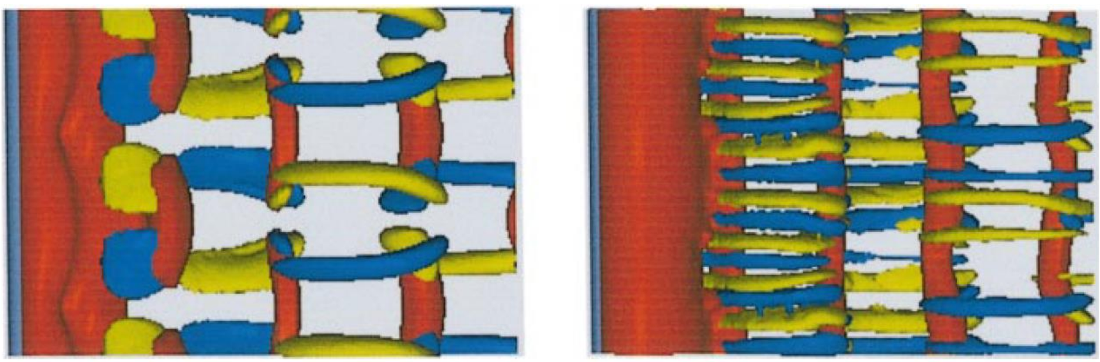

(a) (b)

Fig. 3: Visualizations of shedding modes in the cylinder wake: (a) Mode A, *Re*=210, (b) Mode B, *Re*=250. The yellow and blue isosurfaces represent positive and negative streamwise vorticity, while the red isosurfaces present the absolute spanwise vorticity (Thompson et al. 2000).

The second discontinuous change in the *Re-St* curve denotes the manifestation of mode B. This transitions involves a gradual transfer of energy from mode A to mode B, as *Re* increases. Thus, a specific transition point from one mode to the other does not exist. This transition occurs for *Re* ranging from 230 to 260, but there is also a scatter according to literature. As stated previously, the main difference between the two modes is the spanwise wavelength, which, in this case, is around one cylinder diameter. The latter denotes that the transition of the flow from mode A to mode B demands the reduction of the wavelength value. This reduction is associated the formation of new streamwise vortices between those of mode A. As a result, the streamwise vortices of mode B have an inline arrangement (fig.3b). Finally, it is worth to mention that mode B is more uniform in the spanwise direction, due to its finer scale structure.

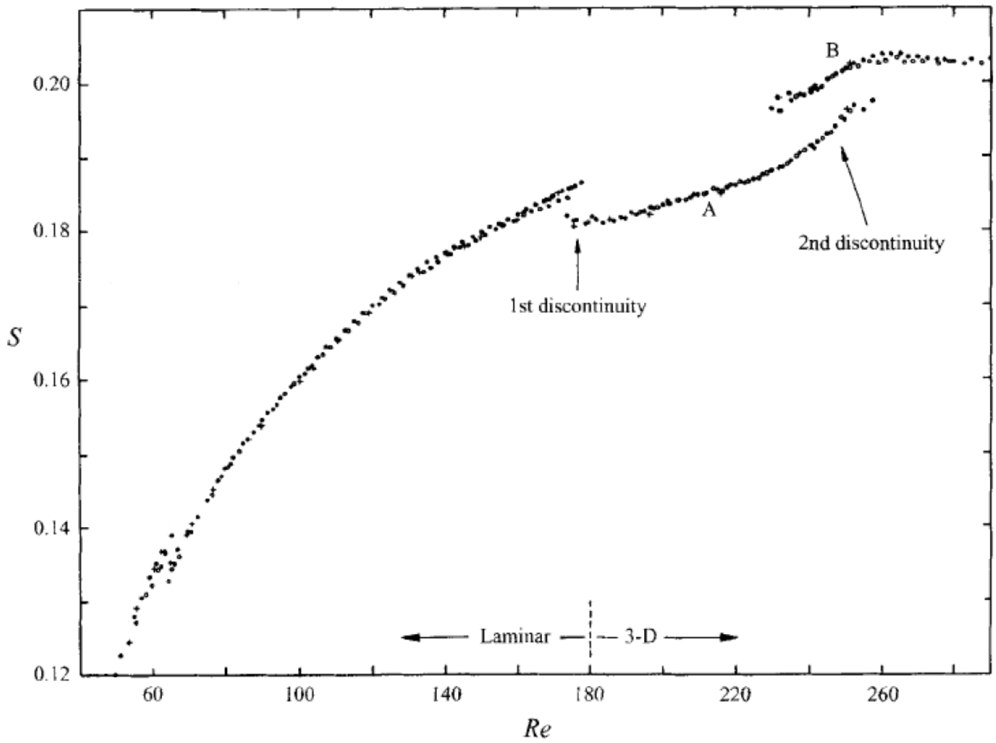

Fig. 4: *St-Re* relationship based on experimental data (Williamson 1989, 1996).

1.2.2 Lift and drag forces

The phenomenon of vortex shedding results in the action of an oscillating force on the cylinder. This force is commonly decomposed into the lift force, F_L, and the drag force, F_D. The lift force is perpendicular to the main flow direction, and its signal is sinusoidal. At low *Re,* the frequency of this signal is the same with the frequency of vortex shedding. As *Re* increases, the signal stops being a pure sine wave, and frequency harmonics of small amplitude are present. The time average value of lift force is zero, in all cases; thus the lift force is commonly expressed in terms of its amplitude or the RMS fluctuation intensity. On the other hand, the drag force is along the main flow direction. Its signal has much smaller amplitude, and its time average value is non-zero. In addition, the frequency of drag force is double in comparison with lift force. The latter occurs because drag force is affected by the absolute value of bound circulation while lift force by the signed value of bound circulation. Finally, the signal of drag force has similar behavior with lift, as regards the presence of harmonics.

Lift and drag forces should be presented in a proper non-dimensional form. This is done in terms of the lift coefficient and the drag coefficient, defined as follows.

$$C_D = \frac{F_D}{\frac{1}{2} \cdot \rho \cdot U_\infty^2 \cdot A} \tag{3}$$

$$C_L = \frac{F_L}{\frac{1}{2} \cdot \rho \cdot U_\infty^2 \cdot A} \tag{4}$$

Where:
ρ: Fluid density
A: Reference area defined as A=D·z (z is the cylinder length).

From dimensional analysis it follows that the drag and lift coefficient only depend on *Re*. This means that the forces acting on the cylinder can be readily calculated when the *Re*-C_D and *Re*-C_L functions are known.

1.3 Heat transfer modes

It is known from Thermodynamics that a system can interact with its surroundings by transferring energy. This energy is usually classified as work or heat. The transfer of energy as heat is due to spatial temperature difference. The study of heat transfer is necessary because Thermodynamics deals with the end states of a process, and provides no information regarding the spatial and temporal variation of the phenomenon. The transmission of thermal energy occurs by means of three mechanisms or modes of heat transfer, namely, conduction, convection and radiation. Radiation is the transfer of thermal energy with electromagnetic waves; since it has no application in the present study, it will not be analyzed further. In the following sub-sections, a short description oh heat transfer by means of conduction and convection is given.

1.3.1 Conduction

The term conduction is used to express the heat transfer on a stationary medium, which may be solid or fluid. In this mode, thermal energy is transferred by the interactions between the particles of the medium. In the case of solids, these interactions are the transfer of lattice vibrations through the molecules, and, in electrical conductors, the translation motion of free electrons. In gases, the heat is transferred by the random molecular motion and the collisions of particles. In more detail, it is known from Thermodynamics that in ideal gas (no intermolecular attractions between the molecules) kinetic energy of the particles is directly proportional to temperature. The latter means that the random motion of a particle or the collision of a particle with another result in the transfer of thermal energy through the medium. The transfer of energy by random molecular motion is called diffusion. Finally, the mechanism of heat transfer by conduction in liquids is based on the same principles as in gases and solids. More specifically, thermal energy is transferred by the random motion and the collisions of particles, but, because of the small gap distance, the molecular interactions are stronger and more frequent.

In order to describe the heat transfer by conduction, an appropriate rate equation is needed. This equation is known as Fourier’s law. Fourier’s law assumes that the medium is continuous therefore it is applicable only in macroscopic scales. The form of the equation is given below.

$$\vec{q}'' = -k \, \nabla T \tag{5}$$

Where:
$\vec{q}''$: Heat flux
k: Thermal conductivity
∇T: Temperature gradient

The heat flux expresses the heat transfer rate (energy per unit time) from a point per unit area. The negative sign in the equation indicates that heat is transferred to the opposite direction from the one corresponding to temperature increase. Finally, the thermal conductivity is a material property, and express how effectively a material conducts heat. Thermal conductivity varies with temperature, but for a number of materials can be treated as constant, because its variation is negligible over a significant range of temperature. In addition, *k* may vary with orientation in anisotropic materials as composites.

1.3.2 Convection

As convection is characterized the mode of heat transfer in fluids when their mass is in bulk or macroscopic motion. This mode can be divided into two simpler mechanisms. The first is based on molecular interactions (*diffusion*) and the second on the macroscopic motion of the fluid (*advection*). The second mechanism increases its contribution to the heat transfer when the stirring of the fluid increases. The latter means that, when the thermal conductivity is considered constant, the heat transfer rates that can be reached by convection are higher than those of conduction. In general, convection is dived into two categories, according to the nature of the flow. In particular, when the flow is caused by external means such as a fan or a pump, convection is called *forced*. In contrast, in *free* convection, the flow is induced by the buoyancy forces, which are duo to density differences caused by temperature variations in the fluid. The heat transfer between a solid boundary and a fluid is generally described by Newton's law of cooling, which is given by the following form:

$$\vec{q}'' = h \cdot (T_W - T_\infty) \tag{6}$$

Where:
$\vec{q}''$: Heat flux density normal to solid boundary
h: Convection coefficient
T_W: Temperature of solid boundary
T_∞: Bulk temperature of fluid

This relation shows that in a convection problem research concerns the determination of the *h* parameter. In contrast to thermal conductivity, the convection coefficient depends on thermodynamic and transport properties of the fluid as well as the nature of the flow. The latter means that convection heat transfer coefficient may not have a constant spatial distribution. In equation (6), temperatures T_W and T_∞ correspond to the temperature of solid wall and the temperature of undisturbed flow away from the boundary, respectively. Generally, the particles of the fluid which are in contact with the solid boundary achieve thermal equilibrium with it. In other words, the first layer of particles towards the surface has the same temperature with the wall. In turn, the particles of the first layer exchange thermal energy with those of the next layer, forming a temperature gradient. There is critical distance, normal to the solid boundary, where temperature gradient is zero and beyond that point temperature is constant and equal to the bulk temperature of the fluid, T_∞. The region of fluid in which a temperature gradient exists is the *thermal boundary layer*, and the distance where the temperature gradient becomes zero denotes the thickness of the thermal boundary layer. In practice, because it is difficult to define where the temperature gradient is zero, the thickness of thermal boundary layer, δ_t , is calculated as the value of *n* for which the ratio $[(T_W-T(n))/(T_W-T_\infty)]=0.99$, where *T(n)* is the temperature of a point at distance *n*, normal to the solid boundary. The thermal boundary layer has the same character with the hydrodynamic boundary layer, and the rate of heat transfer is affected by thermal boundary layer thicknesses. However, the shape of the thermal boundary layer is not independent from the hydrodynamic boundary layer. The relation between the two layers is described by a non-dimensional number, the Prandtl number, *Pr*, defined as follows:

$$Pr = \frac{\mu \cdot C_P}{k} \tag{7}$$

Where:
μ: Dynamic viscosity of the fluid
C_P: Heat capacity at constant pressure of the fluid

Pr is generally defined as the ratio of momentum diffusivity to thermal diffusivity. In other words, *Pr* provides a relation between the momentum and energy transported by diffusion in the hydrodynamic and thermal boundary layer respectively. *Pr* depends only on thermodynamic and transport properties of the fluid, and may thus change its value with temperature variation. When the value of *Pr* is close to unity, representative in gases, the thickness of thermal and hydrodynamic boundary layer are nearly equal. Fluids that have significant higher or lower values of *Pr* than unity are oils and liquid metals, respectively.

In order to define the dimensionless effectiveness of thermal convection, a non-dimensional parameter, known as Nusselt number, *Nu*, is used.

$$Nu = \frac{h \cdot D}{k} \tag{8}$$

Nu is equal to the dimensionless temperature gradient at the surface and provides a measure of heat transferred by convection from the body to fluid. The spatial distribution of *Nu* is not constant on the surface of the body because depends on the convection heat transfer coefficient. For a given geometry, *Nu* is a function of *Re* and *Pr*. If this function is known, typically from experiments, then the value of *Nu* can be readily calculated. From knowledge of *Nu,* the convection heat transfer coefficient may be found and then, from (6), the heat flux may be calculated.

1.4 Heat transfer in flow past a cylinder

Heat transfer by convection between a solid circular cylinder and a fluid in cross flow constitutes a common problem in thermofluids. An important application is heat exchangers, which are made of tubes which exchange thermal energy between a fluid inside them (internal flow) and a fluid around them (external flow). For characterizing the latter, the conditions and the rates in which the heat is transferred should be calculated. Therefore, several studies have addressed the problem of heat transfer in flow past a heated cylinder. As stated before, the non-dimensional numbers which affect heat transfer in this problem, therefore *Nu*, are *Re* and *Pr*. In the present study, the value of *Pr* has been kept constant; thus, only the relationship between *Nu* and *Re* will discussed in the next paragraph.

In general, *Re* affects both the average value and the spatial distribution of *Nu* on the surface of cylinder. Moreover, it is a general trend that *Nu* increases its average value with the increase of *Re*. As regards the distribution of *Nu* across the surface of cylinder, the maximum value is always attained at the front stagnation point, since it is the starting point for the development of the thermal boundary layer, thus characterized by minimum thickness. The local minimum of *Nu* is not located at a fixed point, and its position depends on *Re*. In more detail, for $Re<5$ the local minimum of *Nu* is located at the rear stagnation point and the Nu-ϑ curve is monotonic, where ϑ is the local angle with respect to the front stagnation point. This distribution is associated with the shape of the thermal boundary layer, which increases its thickness until the rear stagnation point. For *Re* ranging from 5 to 47, the point of the minimum value of *Nu* starts to move upstream, following the separation point. Furthermore, a local maximum of *Nu* is attained at the rear stagnation point, due to the formation of recirculation zones. Increasing *Re*, the variation between the local minimum and maximum will increase. Finally, in this region, the average value of *Nu* is a nearly linear increasing function of *Re*. For $47<Re<180$, there are no changes in the general form of the Nu-ϑ curve, however, because the phenomenon is time-dependent due to the formation of vortex street, both the local and space-averaged *Nu* are periodic in time. As a result of vortex shedding, which also affects the thermal boundary layer, the instantaneous Nu-ϑ curve is asymmetric. The signal of space-averaged *Nu* is sinusoidal, and its amplitude increases with *Re*. Moreover, the frequency of this signal is equal to the frequency of drag coefficient (i.e., double the shedding frequency). This is attributed to the fact that the space-averaged *Nu* is affected by the absolute value of bound circulation. In addition, the mean value of this signal, the time-averaged *Nu* continues to be an increasing function of *Re*. For $Re>180$, the spanwise distribution of *Nu* becomes periodic, while its wavelength is affected by the wavelength of shedding mode (mode A or mode B). As *Re* increases further, the local maximum at the rear stagnation point increases its value, due to the high mixture of the flow at this point. Finally, when a portion of the hydrodynamic boundary layer becomes turbulent, a sharp increase of local *Nu* occurs at the transition point. In this regime, the Nu-ϑ curve has thus three local maxima, and for high *Re* the intermediate maximum is higher than those of the front and rear stagnation points.

1.5 Surface hydrophobicity

As hydrophobic or superhydrophobic are characterized surfaces that are difficult to wet. An illustrating example of this surface is the leaf of lotus plant, which can be classified as superhydrophobic. Superhydrophobic leafs enable a droplet impacting on them to fully rebound like an elastic ball. Furthermore, when a drop is located on such kind of an inclined surface, it tends to roll rather than to slide. The cause of these behaviors is the relatively low actual wettability of the solid boundary from the liquid. Generally, such behavior of a solid surface is a combination of low ideal wettability and nanoscale roughness.

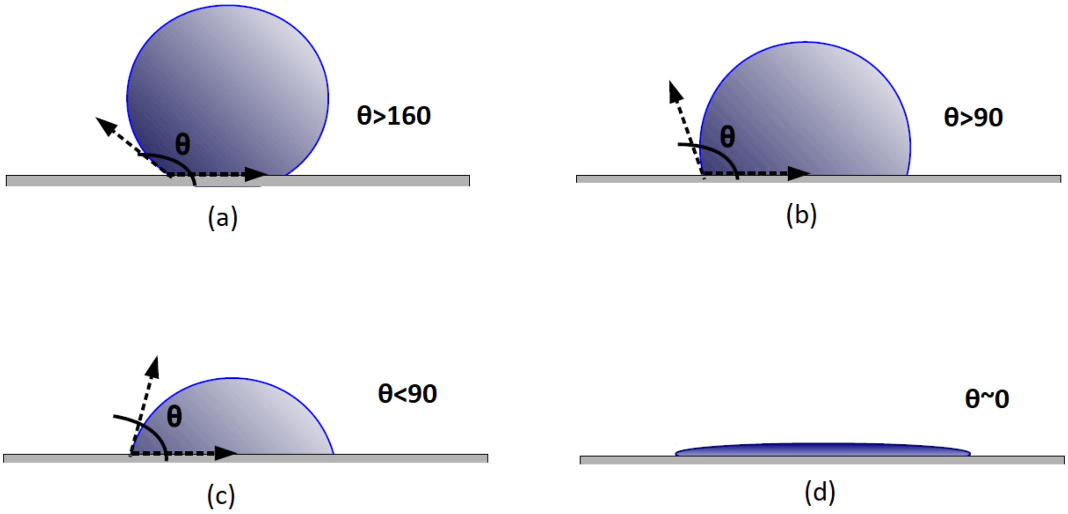

Fig. 5: Contact angle for: (a) superhydrophobic surfaces, (b) hydrophobic surfaces, (c) hydrophilic surfaces, (d) superhydrophilic surfaces (Rios 2011).

1.5.1 Contact angle

In order to understand how ideal wettability and microscale roughness affect the hydrophobicity of a surface, we should introduce a quantity which quantifies hydrophobicity. Generally, in a static condition, hydrophobicity is quantified by the contact angle between a droplet and a horizontal surface. When this angle is less than 90 deg., the surface is characterized as hydrophilic while the surfaces is hydrophobic when the contact angle is higher than 90 deg. In addition, when the contact angle is higher than 160 deg the surface is characterized as superhydrophobic (Fig. 5). For an ideal surface (i.e. flat, rigid, perfectly smooth and chemically homogeneous) in the presence of three phases (i.e. solid, liquid and gas), the contact angle between the solid and liquid is given by the Young's relation (eq.9).

$$\theta = \cos^{-1}[(\gamma_{SG} - \gamma_{LS})/\gamma_{LG}] \tag{9}$$

Where:
θ: Contact angle.
γ_{SG} : Solid-liquid interfacial stress
γ_{LS} : Liquid-solid interfacial stress
γ_{LG} : Liquid-gas interfacial stress

However, this angle expresses the ideal wettability of the surface. In order to calculate the actual wettability or the actual contact angle, some parameters, assumed having negligible effect, must be taken into account. Nevertheless, because a detailed presentation of the effect of each parameter is beyond the scope of the present study, only the effect of microscale roughness will be described next.

When microscale roughness is implemented on the surface, there are two possible contact states between the drop and the surface; the Wenzel state and the Cassie-Baxter state. In the Wenzel state (fig.6a), liquid penetrates the corrugations on the surface, thus increasing the increasing the contact area. In this state, the actual wettability is reduced by the roughness resulting in the increase of hydrophobicity, while the ideal wettability remains the same. To this point, it is worth to mention that the Wenzel state leads to higher hydrophobicity only when the ideal contact angle is higher than 90 deg., otherwise it leads to lower hydrophobicity. The contact angle in this state is given in the following form.

$$\cos\theta_W = r \cdot \cos\theta \tag{10}$$

Where:
θ_W: Contact angle of Wenzel state
θ: Young contact angle
r: Roughness parameter

The roughness parameter is the ratio of actual wetted area to the projected area of the surface. In order to simplify the effect of this parameter, we could consider the case that roughness consists of a periodic array of square pillars (fig.7). In this case, the roughness parameter is equal to $r=1+4\phi_S h/d$, where $\phi_S=d^2/(d+w)^2$ is the fraction of surface covered by pillars. Finally, it should be noted that in this contact state the hydrophobicity can be increased by increasing either the aspect ratio pillars or the density of the pillars.

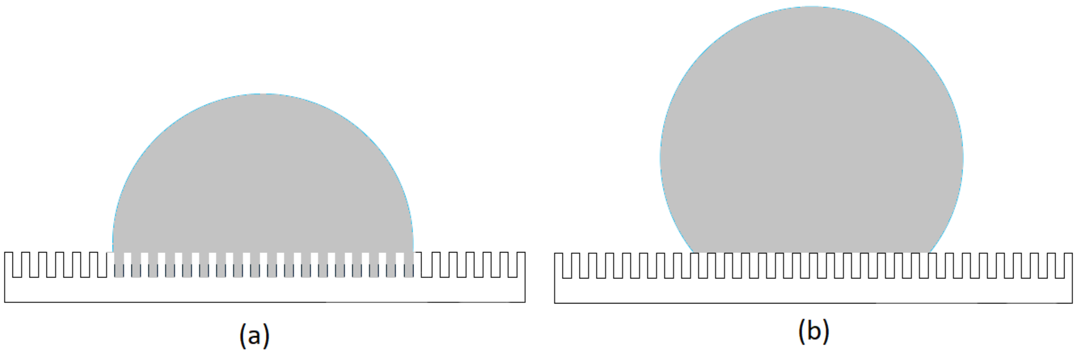

Fig. 6: Contact states. (a) Wenzel contact state, (b) Cassie-Baxter contact state.

On the other hand, in the Cassie-Baxter state, the roughness of the surface prevents the liquid from moving into the space between the pillars (fig.5b). The latter results in the creation of a gas-water interface supported by the tops of the pillars. In this state, the contact angle is given by the following form.

$$\cos\theta_{CB} = -1 + \varphi_S \cdot (1 + \cos\theta) \tag{11}$$

In this case, the contact angle increases in proportion to the amount of gas-liquid interface. It is clear that the Cassie-Baxter state may lead to higher contact angles than those of Wenzel states, for the same roughness. For that reason, the Cassie-Baxter state is desirable state in order to achieve high hydrophobicity. However, there is a maximum in static pressure that can be supported before the liquid-gas interface deflects enough to reach the contact angle and is driven into the space between the surface roughness elements. At this point, the Cassie-Baxter states reverts to Wenzel state. This critical pressure is a function of interfacial stress between the three phases and geometry of surface roughness.

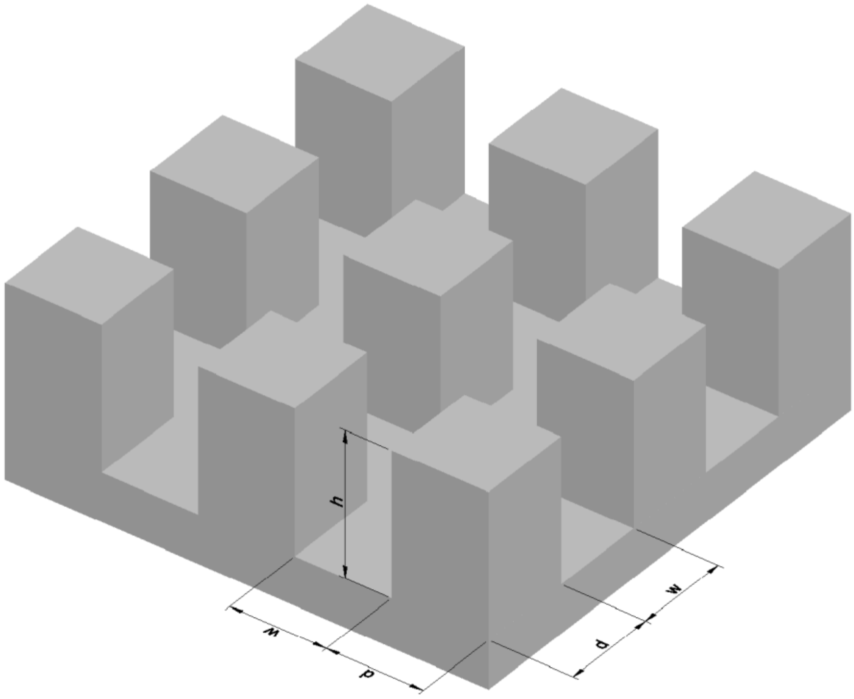

Fig. 7: Microscale roughness consists of a periodic array of square pillars.

1.5.2 Slip length

Macroscopically, when a hydrophobic object is placed on a flow a nonzero velocity may appear at the fluid boundary. One of the parameters which could lead to this phenomenon is the existence of gas-liquid interface (Cassie-Baxter state) in which shear stress is close to zero. Thus, the nonslip condition is inappropriate for this case, and a model which provides a slip velocity is needed. One of the simplest and most commonly used slip model is the Navier model (Zhang et al 2012). The Navier model (eq. 12) assumes that the magnitude of slip velocity is directly proportional to the magnitude of flow shear rate at the wall. The proportionality constant of this equation, called the *slip length*, quantifies the hydrophobicity of the object. In other words, slip length express the distance normal to the wall at which the tangential velocity is zero when the shear stress is constant throughout this distance and equal to the wall shear stress. The latter is illustrated in figure 8, in which the no-slip condition and the Navier model are sketched. Here, it should be mentioned that the quantification of hydrophobicity with the contact angle provides no information about the slip velocity. However, several studies have attempted to find a relationship between the contact angle, and the apparent slip length. In general, slip length trends to increases its value with the increase of contact angle. Nevertheless, because slip length is affected by a wide range of other parameters, it is difficult to extract a correct correlation between the two quantities for every case.

$$V_s = b\left(\frac{\partial V}{\partial n}\right)_W \tag{12}$$

Where:
V_S: Slip velocity
b: Slip length

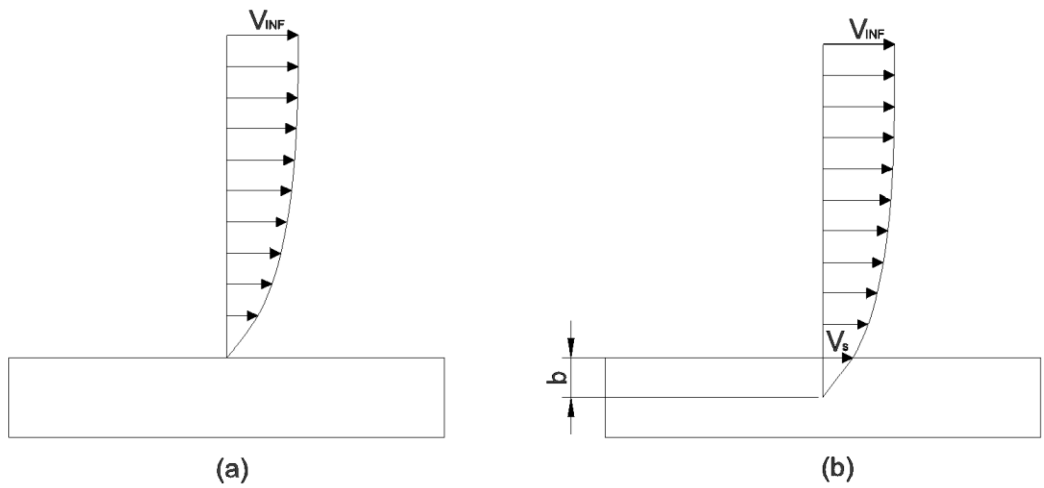

Fig. 8: Velocity profile. (a) Sketch of no-slip condition. (b) Sketch of Navier model for slip velocity.

1.5.3 Effects of hydrophobicity in the case of circular cylinder

The research on potential applications of hydrophobicity started when the existing technology was capable of creating artificially these surfaces. Indeed, a wide range of applications for hydrophobic surfaces has been developed, varying from self-cleaning fabrics to microfluidic devices. In addition, studies on this field have shown that hydrophobic surfaces present a significant reduction of drag force. In the case of flow past a cylinder, implementation of hydrophobicity on its surface results in both reduction of average drag and suppression of unsteadiness. The drag force reduction is partially caused by the lower viscous drag (lower shear stress on fluid boundary) and partially by the lower pressure drag. Pressure drag is mainly related with the wake structure, so its variation is due to the wake modification and suppression of unsteadiness. Indeed, the implementation of hydrophobicity and thus the slip of the flow at the cylinder surface results in the movement of separation point downstream, forming a narrow wake, similar to that at lower *Re*. At low *Re*, a proper value of slip length may lead to complete cancelation of the Karman vortex street.

As regards the effect of hydrophobicity on heat transfer, several studies have shown that hydrophobicity can generally enhance the heat transfer rates. This can easily be explained in the case of a flat plate but in the case of the cylinder the phenomenon is more complex. Near the front stagnation point, similar with the plate, slip velocity results in the formation of a thinner hydrodynamic boundary layer, and therefore a thinner thermal boundary layer. A thinner thermal boundary layer means that the temperature gradient is higher in this region, and thus the resulting value of *Nu*. On the other hand, hydrophobicity also causes stabilization of the flow, decreasing the mixing towards the rear stagnation point, and thus the heat transfer rate. Thus, implementing a proper value of slip length which maximizes heat transfer rates is a subject of research.

2 Flow control and heat transfer enhancement

2.1 Flow control

Several studies have dealt with the problem of controlling flow past a circular cylinder. A principal aim of these efforts was to reduce the oscillating forces on the cylinder, as well as the time-averaged drag. This can be achieved by the suppression of vortex street for *Re* values higher than the critical one, i.e., for *Re*>47. Generally, the control of the flow can be classified as passive control or active control. In passive control, no energy is introduced in the system and the desired goal is achieved by modifications on geometry and properties of the system. On the other hand, active control requires a constant or time-varying amount of energy (active open-loop control and active feedback control, respectively) in order to achieve the desired goal. In the following sections, a few control schemes are briefly described.

2.1.1 Wake splitter plate

One of the first attempts to passively control flow around a circular cylinder was undertaken by Roshko (1954). Roshko introduced a splitter plate at the center plane and parallel to the flow in order to split the wake symmetrically and interfere with the communication between the two sides of the wake. Indeed, Roshko discovered that the introduction of a splitter plate can inhibit the vortex street formation, and therefore can suppress force oscillation on the cylinder. The parameters which control the effectiveness of a splitter plate are the length of the plate, the distance between the cylinder and the leading edge of the plate and the thickness of the plate. Hence, several studies have been performed, after Roshko's experiments, in order to find how these parameters control the structure of the flow. Representative studies are those of Apelt et al. (1973) and Apelt and West (1975), who investigated how the length of the plate affects the flow, and the study of Unal and Rockwell (1988), who used thicker plates than those of earlier experiments. Finally, it is noted that Cardell (1993) replaced the solid splitter plate with a permeable one. In this study, the plates were made of woven wire mesh, and their permeability was controlled by the density of the mesh. The experiments have shown that plates with very high permeability do not affect the flow. On the other hand, plates with sufficient solidity can achieve drag reduction on the cylinder, as well as to uncouple the vortex formation from the cylinder surface, with the generation of primary vortices occurring farther downstream.

2.1.2 Cylinder rotation

The control of the flow with a forced rotation of the cylinder consists an active control scheme. In more detail, when the cylinder rotates with a constant angular velocity or executes a predefined rotary oscillation, the control scheme is classified as active open-loop. On the contrary, the control scheme is characterized as active feedback when the angular velocity is adjusted dynamically using data which describe the system state. Both active open-loop and active feedback schemes have been applied in order to control the structure of the flow and thus the forces acting on the cylinder. In the work of Kang and Choi (1999), constant angular velocities were implemented on the cylinder for low values of *Re*. They pointed out that there is a critical angular velocity above which the shedding on the cylinder completely disappears. In addition, this critical velocity shows a logarithmic dependence on *Re*. Further, they confirmed that this technique can achieve drag reduction with the appearance of a non-zero average lift value (Magnus effect). Mittal and Kumar (2002) performed numerical simulations for *Re*=200 and high angular velocities. They found that a second instability occurs in the wake for a specific range of angular velocities. In this regime, shedding takes place only on one side of the cylinder. Regarding the control of the flow with rotary oscillations, Tokumaru and Dimotakis (1990), using experiments with an active open-loop control scheme, found that significant increase or decrease of drag can be achieved, depending on the frequency and amplitude of oscillation. Finally, Homescu et al (2002), implementing an active feedback control scheme, achieved a large decrease of lift and drag amplitude.

2.1.3 Fluid suction and blowing

Several studies have shown that suction and blowing of fluid, through holes on the cylinder surface, may lead to a significant reduction of drag force and suppression of unsteadiness in the wake. Here, the control scheme is passive when the fluid is transferred naturally through the holes and active when the transfer is imposed. The main parameters of this control scheme are the location of the holes and the mass flow rate. Chen et al. (2015) performed experiments in a wind tunnel, using double skin circular cylinders with ventilation holes on the external skin. They found that both the mean drag and lift amplitude can be significantly reduced. Subsequently, Chen et al. (2017) replaced the double skin cylinder with a cylinder having a slit parallel to the flow, thus creating a communication channel between the front and rear stagnation point. The results of this study exhibited the same trends as those of the previous study (2015). On the other hand, Dong et al. (2008), using an active control scheme, investigated, with numerical simulation, the effect on flow structure when a steady suction is applied on the windward half of the cylinder or a steady suction on the leeward half. They considered two cases, first a fixed cylinder, and second a cylinder allowed to vibrate freely in the cross-flow direction. They found that this control method can sufficiently decrease the lift amplitude and unsteadiness in the wake, for both types of control action. Finally, McDonald and Persoons (2017), using a jet actuator, imposed alternating blowing and suction through a hole located at 90 deg. from the front stagnation point. They pointed out that, for certain actuation frequencies, a significant reduction of mean drag and lift fluctuation intensity can be achieved.

2.1.4 Second Cylinder

The introduction of a small cylinder near the main cylinder is a passive control method, as it does not demand any energy input. The second cylinder modifies the flow structure, forcing the reattachment of the shear layer separated from the main cylinder. The parameters which control the effectiveness of this method are the location and the diameter of the second cylinder (Strykowski and Sreenivasan, 1990). Igarishi and Tsutsui (1992) performed a set of experiments in order to find the optimum location of the second cylinder. Through their experiments, they discovered that a significant drag reduction can be achieved by this method. In addition, they found that placement of the small cylinder can produce a non-zero average lift. Mittal and Raghuvanshi (2001) performed numerical simulations in order to examine the effectiveness of the method at low *Re*. They confirmed that a proper placement of the second cylinder can lead to a full stabilization of the flow.

2.1.5 Surface hydrophobicity

The implementation of hydrophobicity on the surface of a cylinder is a passive, relatively new, control method. As stated in the previous chapter, the movement of the separation point downstream, caused by the slip of the flow at cylinder surface, results in the formation of a narrower wake, stabilizing the flow. In this method, the parameter which mainly affects the flow structure is the intensity of surface hydrophobicity. However, recent studies have shown that the spatial distribution of hydrophobicity also has a major effect on the flow. Legendre et al. (2009), using numerical simulations at low *Re*, have shown that hydrophobicity delays significantly the onset of recirculation zone formation, and vortex shedding in the wake. Moreover, they found that, when the vortex shedding is not completely suppressed, lift and drag amplitudes display a reduction in their values, while the shedding frequency is increased. You and Moin (2007) performed 3-D numerical simulations implementing alternating circumferential bands of hydrophobicity. They observed that the most efficient bands in decreasing lift amplitude and drag were those with a width equal to one cylinder diameter, a value close to the natural wavelength of spanwise flow structure. Finally, Mastrokalos et al (2015) attempted, using multi-objection optimization, to find the most effective distribution of hydrophobicity on the cylinder surface, for flow stabilization at a minimal passive control effort. They found that the absence of hydrophobicity in the rear stagnation point region may have the same result in stabilizing the flow with that of implementing full hydrophobicity (i.e., on the entire cylinder surface).

2.1.6 Mesh around cylinder

Studies with different types of permeable meshes around the cylinder have been carried out in order to find how this method affects the flow structure. This control scheme is passive and the main parameters of it are the shape, the position and the permeability of the mesh. In the experiments of Oruc (2012), an elliptic mesh with edges at upstream and downstream ends was used. The results showed that this mesh type can suppress the formation of primary vortices and diminish the intensity of turbulence by forcing the reattachment of shear layers separated from cylinder. In addition, it was found that the size of mesh does not significantly influence the distribution of turbulence. On the other hand, a cylindrical mesh was introduced in the work of Ozkan et al (2012). They examined a variety of meshes with different sizes and porosities in order to find the most efficient combination. They discovered that a certain range of mesh diameters has the best results in controlling the flow and that the porosity does not affect essentially the formation of vortices. Finally, Oruc et al (2015) performed experiments at different *Re* using a drop-shape mesh. They managed to reduce the turbulence in the wake and inhibit the vortex formation as well.

2.2 Heat transfer enhancement

The enhancement of heat transfer consists a classical problem in the fields of thermofluids and thermal engineering. This is attributed to the demand of the market for lighter, smaller and cheaper heat exchangers which maintaining a desired heat power capability. The latter cannot be achieved by increasing the heat exchange surface or the fluid speed as both lead to the increase of the associate cost. Therefore, several methods have been investigated and implemented in order to design more efficient heat exchangers. Similar with the flow control, heat transfer enhancement methods are classified as passive and active, depending on the input (or not) of energy to the system. In the next paragraphs, a few methods are briefly described.

2.2.1 Vortex promoters and turbulators

Vortex promoters and turbulators are the most common devices used to increase the efficiency of a heat exchanger. These devices, promoting the creation of large scale vortices, increase the flow mixture and thus the heat transfer through the medium. In addition, the turbulence that these devices induce in the wake results in the formation of a thinner thermal boundary layer, and therefore an increase of heat transfer rates at solid boundaries. Usually, these devices are implemented in internal flows, such as flows inside tubes and channels, in order to enhance the flow swirling motions. They have a large variety of shapes, but the most common ones are the spiral stripes and wires. Nonetheless, several other shapes of vortex promoters have been tested in computational and experimental studies. For instance, in the work of Wijayanta et al. (2017) the effects of punched delta winglet vortex generator inside a tube on heat transfer rate and friction loss were investigated. They found that this device increases *Nu* as *Re* increases, but also induces a significant pressure drop along the tube. Vortex promoters have been also introduced in external flows such as flows around a flat plate or a cylinder. Turk (1984) attempted to increase the heat transferred from a heated flat plate using inclined blades near to the leading edge of the plate. The main objective of those blades was to generate vortices perpendicular to the plate. Turk discovered that proper arrangement and height of the blades may lead to great increase of heat transfer rate. In addition, he reported that the most important factor in the design of vortex generators is the need to ensure that the vortices generated remain close to the plate. Finally, in the detailed work of He and Zhang the effects of longitudinal vortex generators were discussed. This type of vortex generators swirl the flow strongly, thus creating streamwise vortices. The main advantage of these vortex promoters is the ability to substantially increase heat transfer rates, while maintaining the associated increase of pressure drop at a moderate level.

2.2.2 Nanofluids

A nanofluid is a fluid containing nanometer-sized particles, called nanoparticles. In heat transfer applications, these particles are made of metals such as Cu, Ag, etc. The main aim of these particles is to increase the effective thermal conductivity of the fluid, resulting in heat transfer enhancement. In this approach, the parameters which control the overall effectiveness are the volume fraction of particles and the material that the particles are made of. Several studies have addressed the problem of heat transfer enhancement for working fluids containing metal nanoparticles. In the work of Kahwaji and Ali (2015), the effectiveness of a water-based nanofluid with Cu in natural convection over a square cylinder was investigated. They performed numerical simulations for different values of Rayleigh number and volume fraction. The results have shown that heat transfer is gradually enhanced when the volume fraction of nanoparticles is increased. On the other hand, Bovand et al. (2015) studied the effect of nanofluids on forced convection over an equilateral triangular cylinder.

They observed that the increase of volume fraction of particles increases the average *Nu*, but also makes the wake more unstable. Regarding the effectiveness of nanofluids on heat transfer in flow past a circular cylinder, literature studies have confirmed heat transfer enhancement. In particular, Vegada et al. (2014) and Abu-Nada et al (2008) found that the increase of volume fraction of particles increase the average *Nu*. Moreover, Vegada et al. observed that with the increase of volume fraction the temperature gradient on the cylinder surface drops but the relative high thermal conductivity of fluid leads the heat flux to increase.

2.2.3 Surface hydrophobicity

As stated in previous paragraphs, implementing surface hydrophobicity is a passive control method, which depends on the intensity and spatial distribution of hydrophobicity. Here, heat transfer enhancement is achieved by modifying the flow structure. Maynes et al. (2008) studied the influence of hydrophobicity on heat transfer rates between two parallel walls, performing 2-D numerical simulations. In contrast to other studies, they did not use a direct slip model, but implemented micro-roughness on the walls in the form of micro-ribs and cavities. The found that, as the size of cavities increases, the heat transfer rate drops, while pressure drop along the channel decreases. Finally, they reported that the ratio of *Nu* to friction factor increases with the increase of the intensity of hydrophobicity, which means that higher hear transfer rate is attained per unity of energy input for moving the fluid. In the work of Haase et al. (2015) heat transfer inside a circular tube with hydrophobic and superhydrophobic surface was investigated. They modeled hydrophobicity using the Navier model, and found that *Nu* increases with the increase of the intensity of hydrophobicity. Finally, Kafarakis et al. (2016) investigated the effects of surface hydrophobicity in flow past a cylinder, using 2-D numerical simulation. They used different spatial distributions of surface hydrophobicity, and found that the absence of hydrophobicity in the region of rear stagnation point leads to the same heat transfer rates with full hydrophobicity, while flow stability is also increased.

2.2.4 Pulsating Flow

Several numerical and experimental studies have investigated how pulsating flow affects heat transfer rates. However, due to the complexity of the phenomenon and the relatively large number of parameters associated with implementing this approach, the results are often contradictory on whether this method indeed enhances heat transfer or not. In brief, the most important parameters of the problem are the pulsation frequency and pressure amplitude. Li et al. (2015) studied numerically heat transfer over a flat plate confined by a cylinder under pulsating flow. They considered constant uniform heat flux over the plate, and found that pulsating flow leads to lower temperatures on the surface, as well as lower temperature gradient, which is equivalent to heat transfer enhancement. On the other hand, Li et al. (2016) investigated experimentally heat transfer in flow past a heated circular cylinder. They studied several cases of different *Re*, pulsation frequency and pressure amplitude. They reported that heat transfer rates are enhanced with the increase of pressure amplitude, while generally decreasing with the increase of pulsation frequency.

3 2-D problem setup

3.1 Computational model – equations

In the present study, we consider an infinitely long heated circular cylinder in an incompressible uniform cross flow. For the computation of the flow field, the non-dimensional form of incompressible Navier-Stokes equations are utilized (eq.10). In addition, the temperature field is computed from the solution of energy equation (eq.11). The thermo-physical properties of fluid are assumed to be independent of its temperature. The assumption of constant thermophysical properties enables to partially uncouple the Navier-Stokes and energy equations. This means that the flow field is independent of the temperature field, however the inverse does not hold. The form of continuity equation (9), Navier-Stokes equations or momentum equations (10) and energy equation (11) is given below.

$$\nabla \cdot \vec{V} = 0 \tag{9}$$

$$\frac{\partial \vec{V}}{\partial t} + (\vec{V} \cdot \nabla)\vec{V} = -\nabla p + \frac{1}{Re}\nabla^2 \vec{V} \tag{10}$$

$$\frac{\partial T}{\partial t} + (\vec{V} \cdot \nabla)T = \frac{1}{Re \cdot Pr}\nabla^2 T + \frac{Ec}{Re}\Phi \tag{11}$$

Where:
$\vec{V}$: Velocity vector $\vec{V} = (u, v)$
p: Static pressure
T: Temperature

Eckert number $$Ec = \frac{U_\infty^2}{C_p \cdot (T_W - T_\infty)} \tag{12}$$

Viscous dissipation term $$\Phi = \left\{2\left[\left(\frac{\partial u}{\partial x}\right)^2 + \left(\frac{\partial v}{\partial y}\right)^2\right] + \left(\frac{\partial v}{\partial x} + \frac{\partial u}{\partial y}\right)^2\right\} \tag{13}$$

The physical variables of the problem have been non-dimensionalized with the proper use of scales based on cylinder diameter *D*, free steam velocity U_∞, fluid density *ρ* and the temperatures of cylinder surface T_W and free steam temperature T_∞. Here, the focus is not related to the effects of thermophysical properties; thus, the values of *Pr* and *Ec* (eq.12) were maintained constant in all simulations, equal to *Pr*=1, *Ec*=0.001. *Ec* is a non-dimensional number which express the relationship between the flow's kinetic energy and the boundary layer enthalpy difference. In other words, *Ec* expresses the rate at which the kinetic energy is transformed to thermal energy, increasing the fluid temperature. It is known that, as the value of *Ec* decreases, the effect of viscous dissipation term (eq.13) decreases too. Practically, when *Ec* is substantially lower than unity (*Ec*<<1), the viscous dissipation term has a negligible effect on the energy equation. In the present study, the ANSYS CFD code was used for the solution of the governing equations, with a second-order finite volume scheme and a second-order time integration method.

3.2 Computational domain – boundary conditions

According to literature studies, the most common computational domains around a circular cylinder are the cylindrical domain and the rectangular domain. The advantages of cylindrical domain are the simplicity of grid generation and the solution of governing equations in a structured mesh using a cylindrical coordinate system. However, in such domains, choosing and implementing boundary conditions is not a straightforward procedure, because inflow and outflow faces are not readily defined. On the other hand, rectangular domains present difficulties in grid generation but not in implementing boundary conditions. In the present study, the computational domain is rectangular, with its long side parallel to free stream velocity. In more detail, the length and width of computational domain are 80D and 34D, respectively. The distance between the center of cylinder and inflow boundary is 20D while the distance between cylinder and lateral boundaries is 17D. The center of coordinates is taken at cylinder center, as shown in (fig. 9) and (fig. 10). The sufficiency of the present domain size has been validated in the studies of Kaiktsis et al. (2007), Delaunay and Kaiktsis (2001), and Evangelinos and Karniadakis (1999).

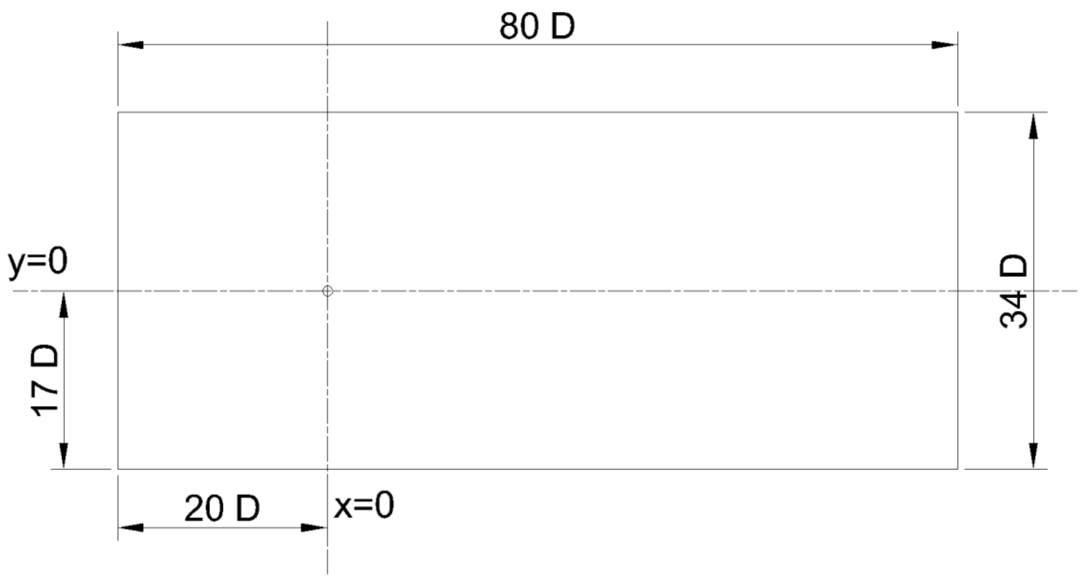

Fig. 9**:** Computational domain.

The following conditions are prescribed at the domain boundaries.

- Inflow and lateral boundaries: $u = U_\infty = 1, v = 0, T = T_\infty = 0$
- Outflow: $p = 0$, Newman boundary condition
- Cylinder surface: $u_r = u_\theta = 0, T = T_W = 1$

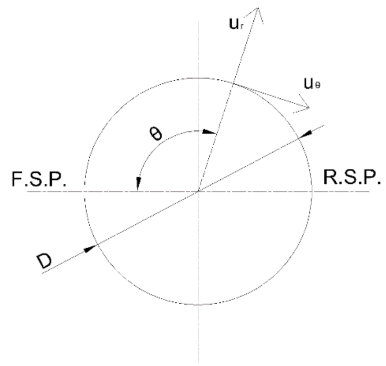

Fig. 10**:** Definition of angular displacement, measured from the front stagnation point (θ) and local components of velocity (u_r and u_θ).

3.3 Grid generation

As stated above, a rectangular domain around a circular cylinder causes a complexity for grid generation because the cylindrical shape of the mesh near the cylinder must gradually transform to rectangular. To better control mesh generation (i.e., shape and size of finite volume elements), the main domain has been divided into subdomains. Some ways of decomposing the main domain were tested, and it was found that the division into nine subdomains was sufficient for the grid control (fig.11). Here, the complexity is localized in the central region close to cylinder, but even there mesh has a sufficient quality as the number of triangular elements has been minimized and the elements smoothly change their arrangements from cylindrical to parallelograms. In the other eight subdomains, grid generation was a simple procedure because their elements are everywhere rectangles. In these subdomains, elements located near the boundaries of the main domain were designed to have bigger size than those near the cylinder. In more detail, along the longitudinal direction, elements are quadratic at the central region and they are gradually transformed to rectangles, with the long side being double the short side at the inflow and outflow boundaries. Similarly, in the transverse direction, elements are transformed from quadratic to rectangles, with the length of long side being four times the length of short side at the lateral boundaries (fig.12).

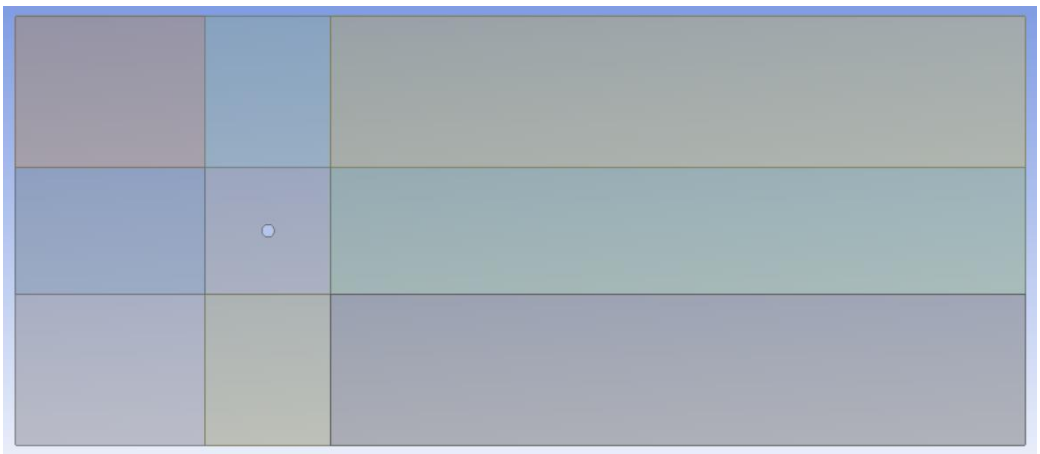

Fig. 11**:** Decomposition of the flow domain in nine subdomains.

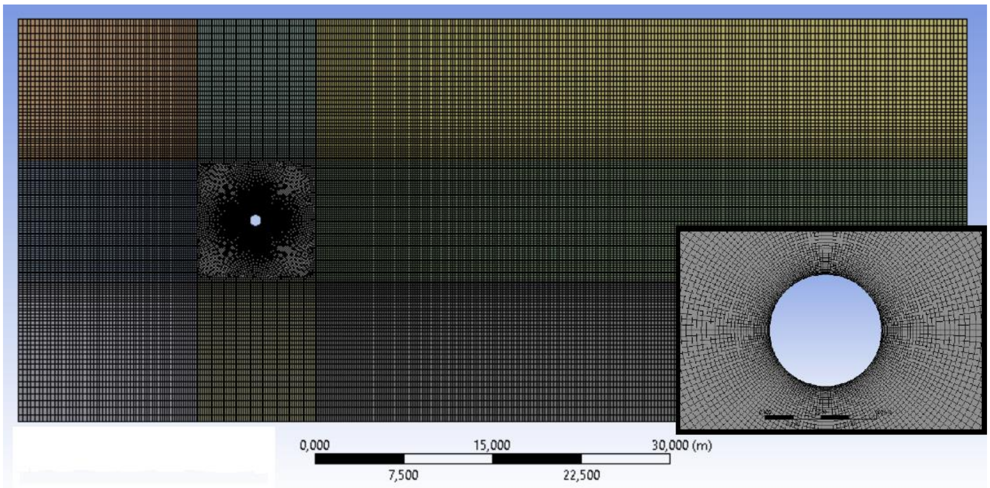

Fig. 12**:** Finite volume mesh (approximately 50000 elements) with detail close to cylinder (the number of finite volumes osculating to cylinder surface is 160).

3.4 Resolution tests

In order to select the proper spatial and temporal discretization, resolution tests must be performed. The main aim of these tests is to find the mesh density and the value of numerical time step above which the results are practically independent from further increase of number of elements and decrease of time step value. Practically, because this independence occurs in extremely fine meshes and time steps, a mesh or time step is considered to be sufficient when the results have the desired accuracy or the changes are negligible. In the following paragraphs, the spatial and temporal resolution tests are described.

3.4.1 Spatial resolution tests

In order to find a sufficient mesh around the cylinder, several resolution tests were performed for different values of *Re.* In these tests, the value of numerical time step was maintained relatively low (Δt=0.01) and eight grids were tested, with a number of elements from approximately 10000 to 80000. In addition, for each *Re,* a high resolution grid, with 185000 elements, was tested in order to obtain indisputably accurate results, which could be compared with those of other (coarser) meshes. In the next figures, the results for *Re*=120 and *Re*=300 are shown. The first value of *Re* was selected because in this region the flow structure is 2-D and for that reason a 2-D numerical simulation can in principle represent the same phenomena with an actual flow. On the other hand, the goal of the present study is to investigate the flow structure at higher *Re*, where the phenomena are 3-D, and 2-D simulations are not adequate; nonetheless, the adequacy of discretization in x-y planes must still be assessed by means of 2-D simulations. For each of the grids considered, force coefficients and shedding frequency are calculated. As regards the force coefficients, the time average value of drag coefficient $<C_D>$ and the amplitudes of drag and lift coefficient, $C_{D,AMP}$, $C_{L,AMP}$, are calculated. Finally, the shedding frequency is expressed in terms of the Strouhal number, *St*.

The results of the first resolution test are presented in figure 13 and table 1. In figure 13, the values of force coefficients and shedding frequency are plotted versus the number of elements of each grid. It should be noted that the parameters considered approach quickly their limit values. Indeed, the grids consisting of 40000 and 50000 elements display results with negligible deviation against the grid with 185000 element. This trend is also presented in table 1, which contains the values of force coefficients and shedding frequency for each mesh considered. Based on these results, we conclude that a grid consisting of 40000 elements is sufficient for *Re*=120.

Table 1: Spatial resolution tests for *Re*=120 and time step Δt=0.01. Values of time-averaged drag coefficient $\langle C_D \rangle$, lift coefficient amplitude, $C_{L,AMP}$, drag coefficient amplitude, $C_{D,AMP}$, and Strouhal number, St, for each grid.

N	$\langle C_D \rangle$	$C_{L,AMP}$	$C_{D,AMP}$	St
10000	1.318228	0.393947	0.014511	0.165152
20000	1.334927	0.419969	0.016017	0.171087
30000	1.339447	0.423934	0.016263	0.172662
40000	1.342495	0.426736	0.016551	0.173611
50000	1.344375	0.428512	0.016670	0.174166
60000	1.345007	0.429063	0.016726	0.174317
70000	1.345516	0.429621	0.016762	0.174520
80000	1.346309	0.430556	0.016849	0.174723
185000	1.347392	0.432293	0.017000	0.175080

Table 2: Spatial resolution tests for *Re*=300 and time step Δt=0.01. Values of time-averaged drag coefficient, $\langle C_D \rangle$, lift coefficient amplitude, $C_{L,AMP}$, drag coefficient amplitude, $C_{D,AMP}$, and Strouhal number, St, for each grid.

N	$\langle C_D \rangle$	$C_{L,AMP}$	$C_{D,AMP}$	St
10000	1.337096	0.856418	0.069435	0.196740
20000	1.369865	0.910332	0.079353	0.205076
30000	1.378131	0.919917	0.080705	0.207408
40000	1.385380	0.929434	0.082349	0.209018
50000	1.390180	0.936715	0.083789	0.209895
60000	1.391843	0.939403	0.084326	0.210195
70000	1.393244	0.941620	0.084803	0.210471
80000	1.395256	0.945541	0.085627	0.210748
185000	1.398779	0.953887	0.087422	0.211225

In figure 14, the results of resolution tests for *Re*=300 are shown. Again, the force coefficients and shedding frequency are plotted versus the number of elements of each grid considered. Here, it is observed that values approach their limit, but with higher required resolution, as the grid density is increasing. In addition, the deviation between the results of the second finest grid (80000 elements) and the finest grid (185000 elements) is still very small, but higher than that for *Re*=120. However, as shown in table 2 and figure 14, the results of grids with 50000 and 60000 are close enough with those of the finest grid, which are assumed to be accurate. Indeed, the highest deviation between the results of the grid with 50000 elements and the finest grid, in terms of the drag coefficient amplitude, are about 4%. Moreover, the deviations in time-average drag coefficient and *St* are lower than 1%. For these reasons, we could say that a grid with 50000 elements is sufficient for simulation of 2-D flow, even for *Re*=300. All numerical simulations, reported in the next chapters are performed with grids consisting of 50000 elements in x-y planes.

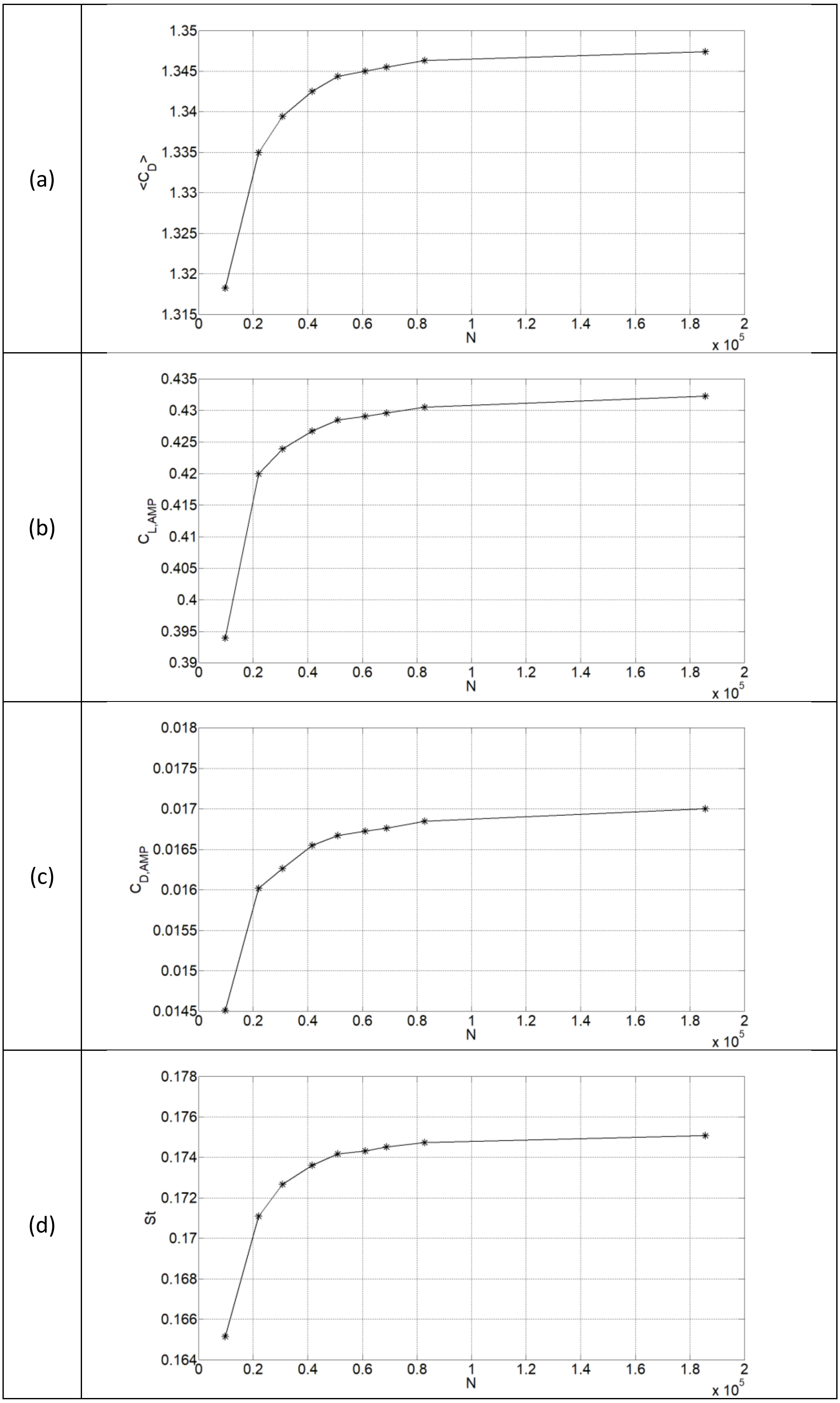

Fig. 13**:** Spatial resolution tests for *Re*=120 and time step *Δt*=0.01. (a) Time-averaged drag coefficient, (b) lift coefficient amplitude, (c) drag coefficient amplitude, (d) Strouhal number, versus number of elements of each grid.

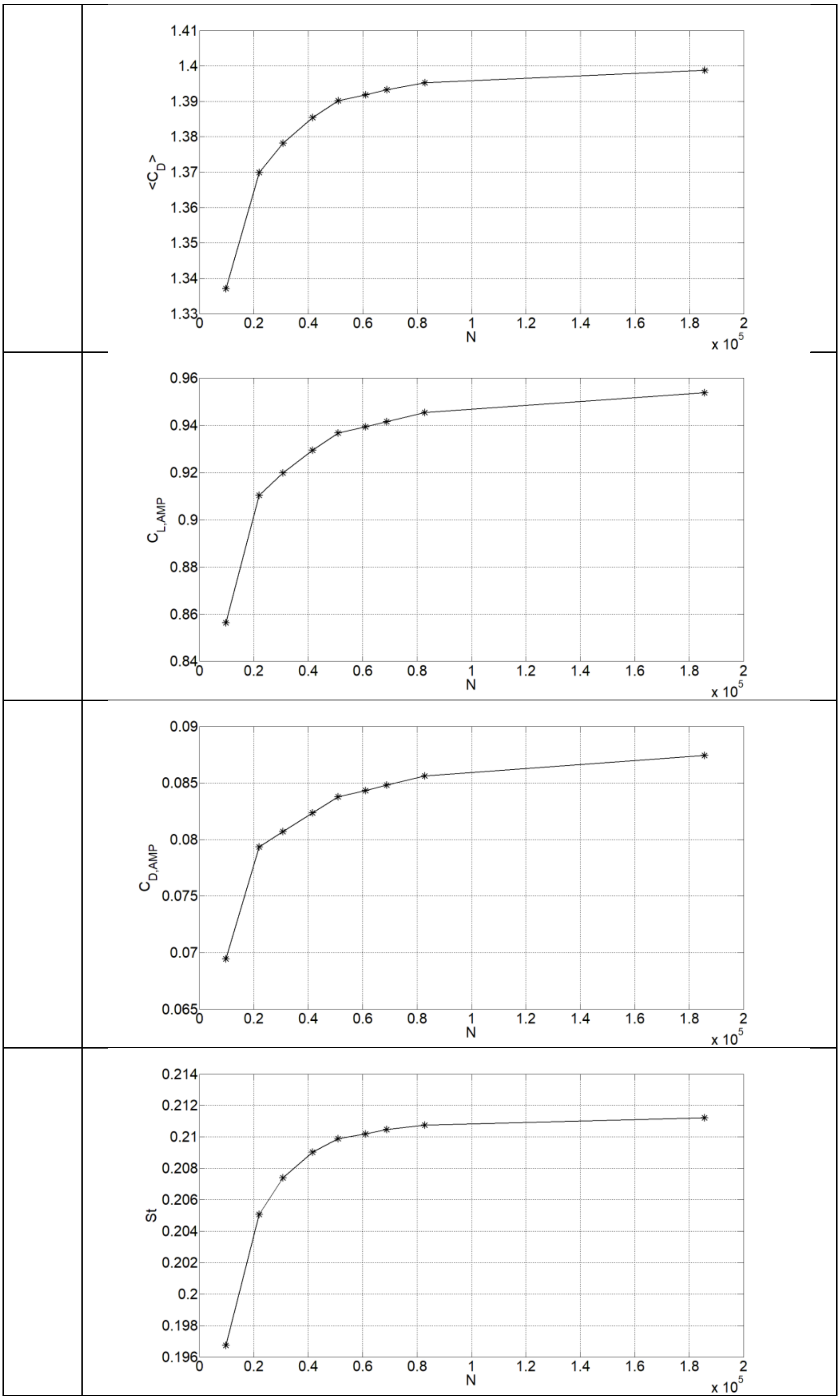

Fig. 14: Spatial resolution tests for *Re*=300 and time step *Δt*=0.01. (a) Time average drag coefficient, (b) lift coefficient amplitude, (c) drag coefficient amplitude, (d) Strouhal number, versus number of elements of each grid.

3.4.2 Temporal resolution tests

In the present paragraph, results of temporal resolution tests are reported, performed with a grid selected from the spatial resolution tests (50000 elements). Here, the (non-dimensional) time step values tested are Δt= 0.1, 0.05, 0.02, 0.01, 0.005. The numerical simulations were performed for *Re*=120, and as in the spatial resolution tests, the values of force coefficients and shedding frequency were considered.

The computed values of force coefficients and *St* versus time step value are presented in figure. 15. The results are shown to be a nearly linear function of time step. In more detail, the value of force coefficients decreases linearly with the decrease of time step, whereas the shedding frequency increases. Nevertheless, as shown in table 3, the deviations between the results of Δt=0.01 and Δt=0.005 are negligible. Indeed, for most of the results, differences are observed in the third decimal point, and the highest relative deviation, present in the drag amplitude coefficient, is about 5%. Moreover, the deviations in time-averaged drag coefficient and St are lower than 1%.For these reasons, the time step value Δt=0.01 is considered as acceptable, and all the simulations, reported in the next chapters use this time step value.

Table 3**:** Temporal resolution tests for Re=120, using a grid with 50000 finite volumes. Values of time-averaged drag coefficient, $\langle C_D \rangle$, lift coefficient amplitude, $C_{L,AMP}$, drag coefficient amplitude, $C_{D,AMP}$, and Strouhal number, St, for each value of numerical time step.

Δt	$\langle C_D \rangle$	$C_{L,AMP}$	$C_{D,AMP}$	St
0.1	1.405392	0.614463	0.032649	0.168550
0.05	1.373714	0.515067	0.023576	0.171923
0.02	1.351954	0.450302	0.018327	0.173712
0.01	1.344422	0.428546	0.016672	0.174166
0.005	1.340617	0.417716	0.015879	0.174419

(a)
(b)
(c)
(d)

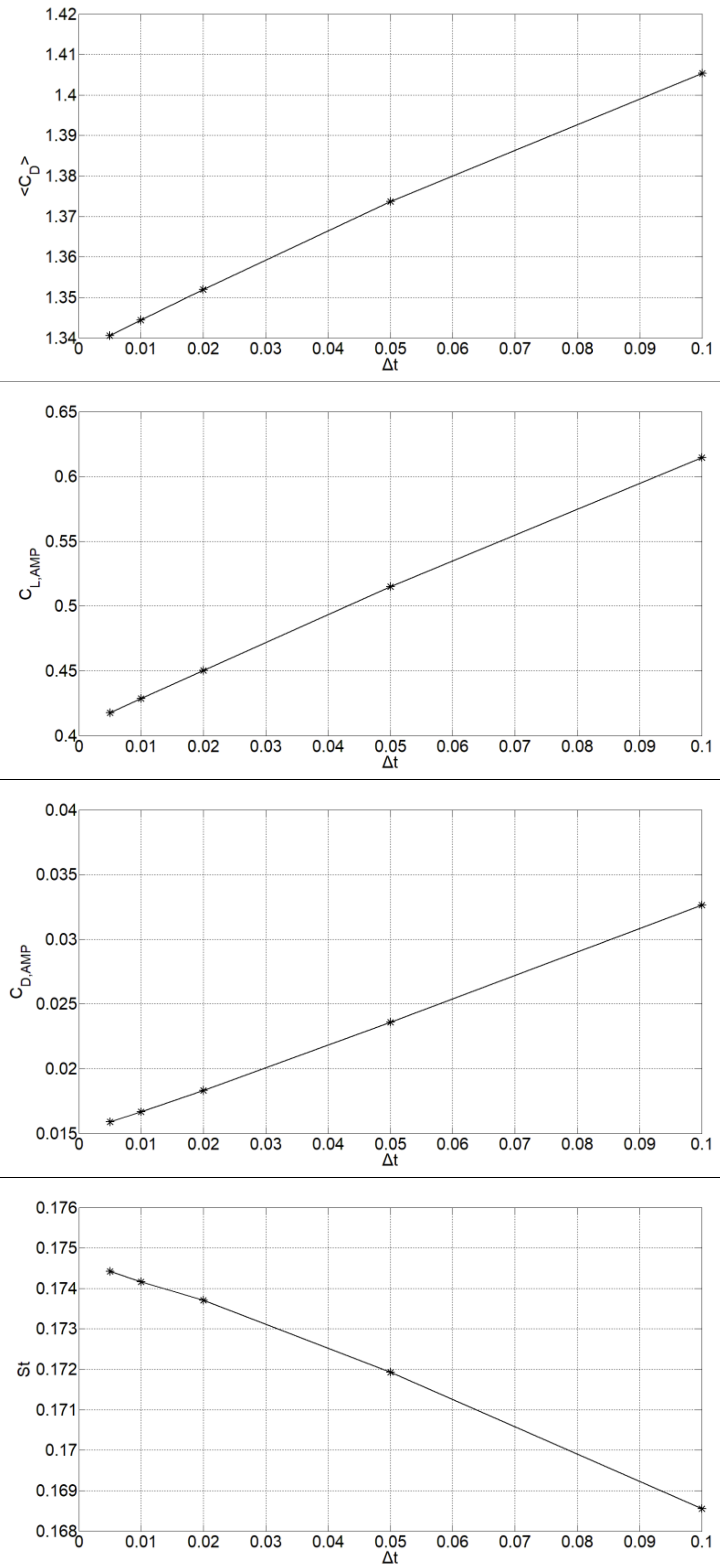

Fig. 15**:** Temporal resolution tests for *Re*=120, for a grid with 50000 finite volumes. (a) Time-averaged drag coefficient, (b) lift coefficient amplitude, (c) drag coefficient amplitude, (d) Strouhal number, versus the value of numerical time step.

3.5 Validation tests

In this paragraph, the present numerical results are validated by comparing high resolution simulation of the uncontrolled flow against published literature data. Here, the simulations are performed for *Re* ranging between 40 and 180, for which flow remains 2-D. In more detail, the time-averaged drag coefficient, shedding frequency and mean *Nu* are examined, for each *Re* considered. Fig. 16a presents the variation of time-averaged drag coefficient with *Re*, for the present study and those of Patnana et al. (2009) and Henderson (1995). An excellent agreement between the results of the present study and those of literature is demonstrated. In figure 16b, the non-dimensional shedding frequency versus *Re* of the present study is compared with the results of Fey et al. (1998) and Hammache and Gharib (1991). The results of these literature sources present a small deviation, which increases with *Re*. Nonetheless, the results of the present study are characterized by values close to the middle of the range of literature values.

(a)

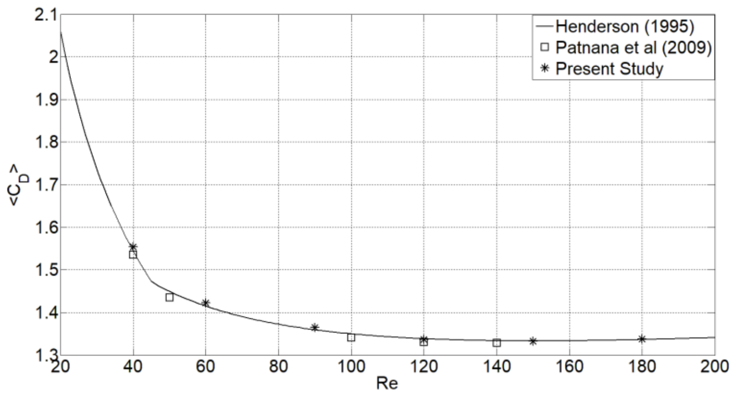

(b)

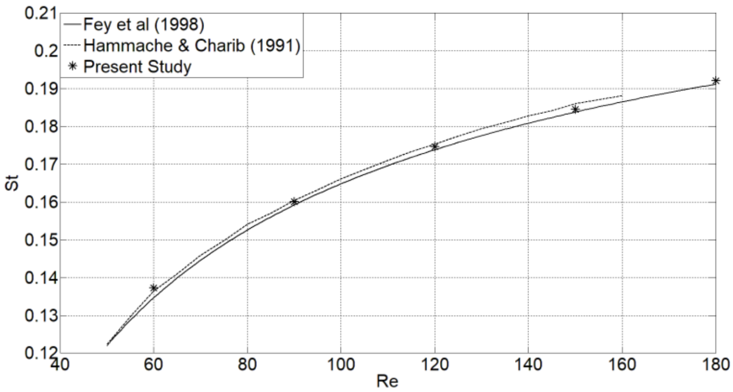

Fig. 16**:** Validation of the present results with literature studies. (a) Time-averaged drag coefficient versus *Re*. (b) Non-dimensional shedding frequency (*St*) versus *Re*.

Validation tests regarding heat transfer are presented in figure 17. Fig. 17a presents the spatial distribution of *Nu* on the cylinder surface for *Re*=40. In this regime, the distribution of time-averaged local *Nu* is the same with the distribution of instantaneous local *Nu*, since the flow is steady. The agreement between the present results and that of Patnana et al. (2010) is excellent, for the entire cylinder surface. Finally, in fig. 17b the time-averaged *Nu* for different *Re* is presented and compared with the results of Patnana et al (2010) and the correlation of Churchill and Bernstein (1977). The deviation between the present results and those of the other works is acceptable, for every *Re* considered. Summarizing the results of validation tests, we could state that the present numerical simulations for a grid consisting of 50000 elements and a time stem equal to Δt=0.01 can accurate predict the flow and temperature field.

(a)	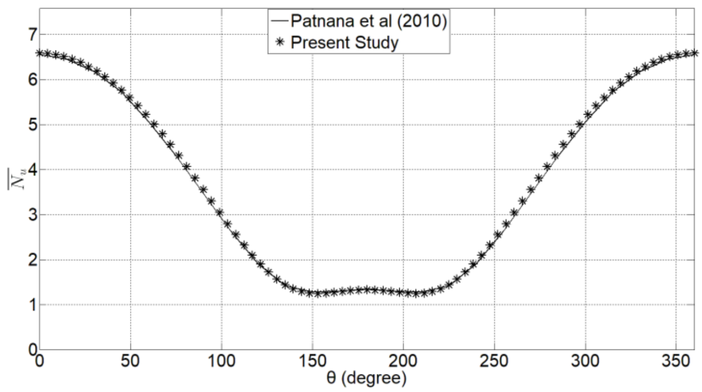
(b)	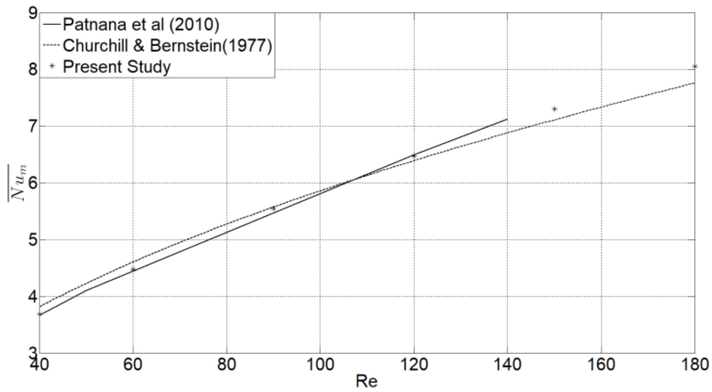

Fig. 17**:** Validation of the present results with literature studies. (a) Spatial distribution of *Nu* on cylinder surface for *Re*=40. (b) Time-averaged *Nu* versus *Re.*

4 3-D problem setup

In this chapter, the computational approach of the flow around a 3-D circular cylinder is presented in detail. We consider an infinitely long, heated circular cylinder in uniform and incompressible cross flow taking into account the presence of 3D phenomena in the flow. Similar with the 2D problem, the governing equations are the incompressible Navier-Stokes equations (eq.10) end energy equation (eq.11). Here, the only difference in these equations is the velocity vector $\vec{V}$ which contains three velocity components, $\vec{V} = (u, v, w)$. In addition, the viscous dissipation term in energy equation, because of the new velocity component, takes the following form.

$$\Phi = \left\{2\left[\left(\frac{\partial u}{\partial x}\right)^2 + \left(\frac{\partial v}{\partial y}\right)^2 + \left(\frac{\partial w}{\partial z}\right)^2\right] + \left(\frac{\partial v}{\partial x} + \frac{\partial u}{\partial y}\right)^2 + \left(\frac{\partial w}{\partial y} + \frac{\partial v}{\partial z}\right)^2 + \left(\frac{\partial u}{\partial z} + \frac{\partial w}{\partial x}\right)^2\right\} \quad (14)$$

Moreover, the assumption of constant thermo-physical properties is maintained in these simulations too. *Pr* and *Ec* have the same values with the 2D simulations (i.e. *Pr*=1 and *Ec*=0.001) and the same procedure was followed for the non-dimensionalization of the problem.

4.1 Computational domains – boundary conditions

In the present study two different computational domains were tested in order to find which one display more accurate results. Both domains had the same shape with the 2D domain, presented in previous chapter, at XY plane (plane perpendicular to cylinder axis). However in Z direction the first domain extends 2πD (fig.18a) and the second πD (fig.18b). Where, D is the diameter of the cylinder and π is equal to 3.14159. As regards the boundary conditions, they are the same with the 2D simulations. In addition, at the lateral boundaries perpendicular to Z direction (cylinder axis) periodic boundary conditions are prescribed. For the grid generation, the same procedure with the 2D domain was followed. In more detail, the main domain was divided into nine subdomains (fig.19) and the shape and number of elements at X-Y planes was the same with the 2D grid. In the spanwise direction, elements followed a uniform distribution, since there exist no regions which demand more dense or sparse grids (fig.20). In the next sub-sections, the results from the two different computational domains are presented

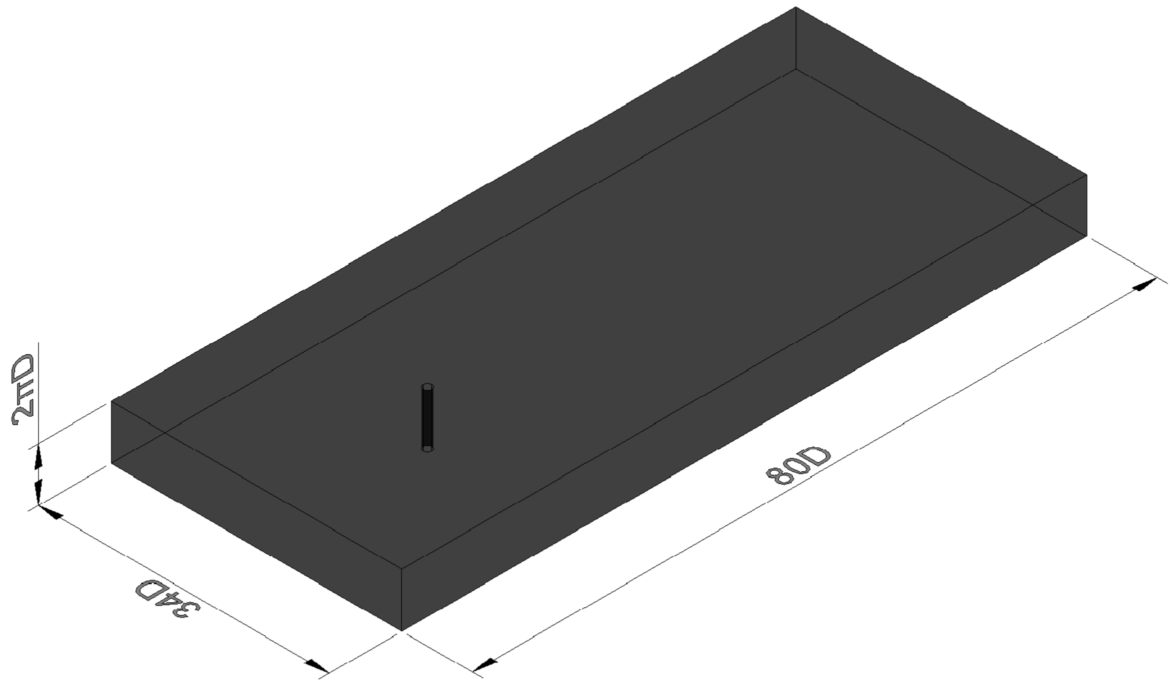

(a)

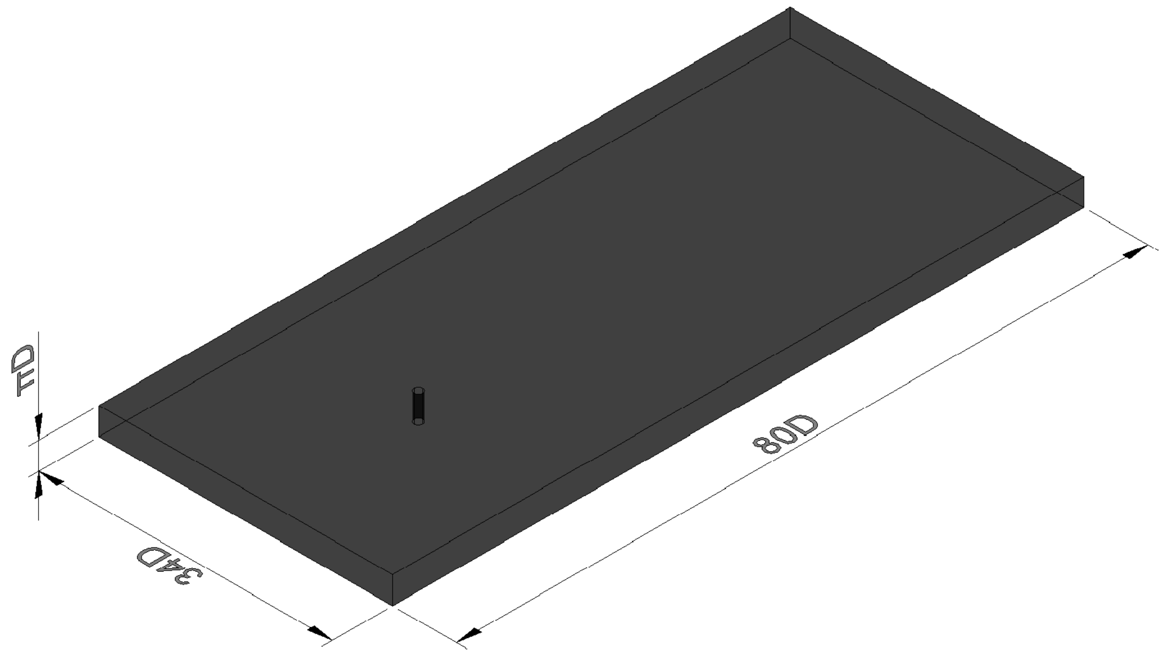

(b)

Fig. 18: Perspective view of computational domain. (a) Domain length in spanwise direction equal to 2πD. (b) Domain length in spanwise direction equal to πD.

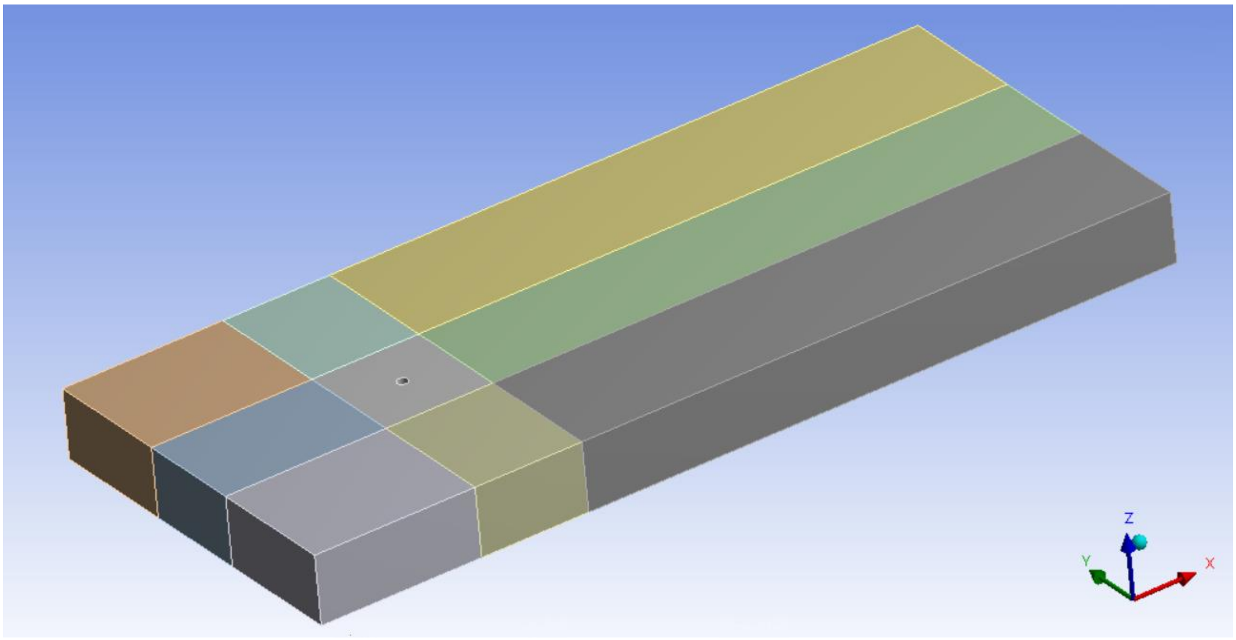

Fig. 19**:** Perspective view of computational domain with a spanwise length of 2πD and its decomposition into nine subdomains.

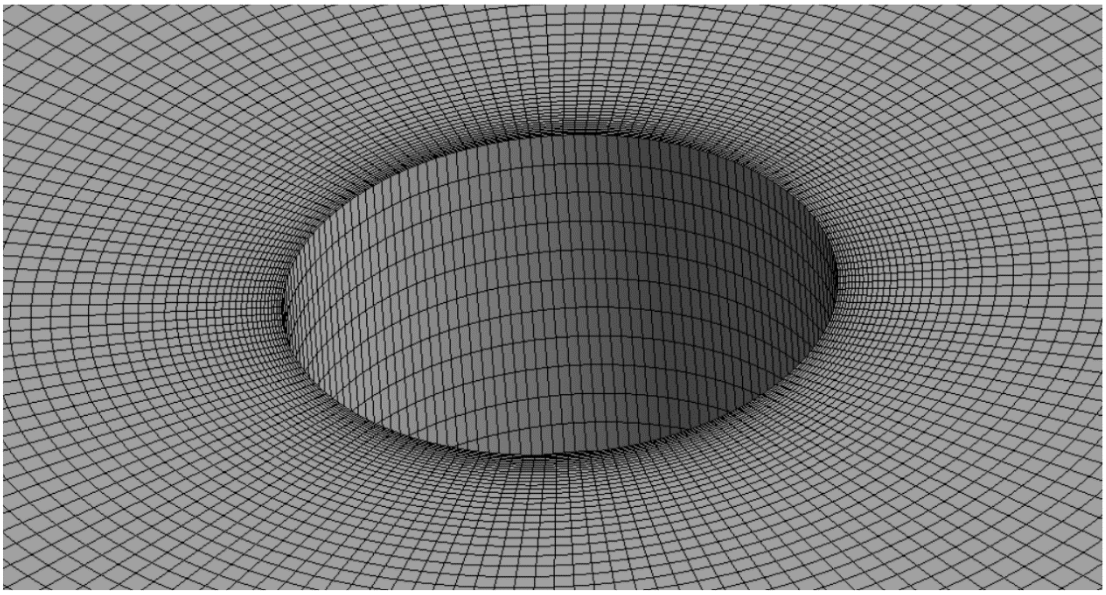

Fig. 20**:** Perspective view of mesh close to the cylinder. Elements follow a uniform distribution in the spanwise direction.

4.1.1 2πD computational domain

In this sub-section, the numerical simulations are performed using a computational domains which extents 2πD in Z direction, illustrated at figure 14a. The size of this domain is deemed sufficient according to the studies of Kim and Kim (2010) and Labbe and Wilson (2007). Here, the simulations were performed for *Re* equal to 300 where the flow structure is 3D and the mode B is the dominant shedding mode. In order to select the proper spatial discretization, resolution tests were performed. In these tests, the number of elements at XY plane was constant and equal to 50000 (this grid is sufficient for *Re* up to 300 according to the resolution tests of the previous chapter). However, in the spanwise direction the number of elements varied from 50 to 100. In particular, four grid were tested which had 50, 60, 80, and 100 elements in spanwise direction and total 2500000, 3000000, 4000000, 5000000 respectively. For each grid considered, force coefficients and shedding frequency are calculated. In addition, visualization of the flow by mean of instantaneous spanwise and streamwise vorticity are presented. As regards the force coefficients, the time average value of drag coefficient $<C_D>$ and the amplitudes of drag and lift coefficient $C_{D,AMP}$, $C_{L,AMP}$ are calculated. Finally, the shedding frequency is represented with the use of *St*.

The results of the resolution test are presented in figure 16 and table 4. The time average drag coefficient (fig.21a), amplitudes of lift (fig.21b) and drag (fig.21c) coefficient and shedding frequency (fig.21d) are plotted versus the elements of each grid. It is observed that the first three grids display almost the same results and the deviation between them is at the third decimal point. However, as shown in figure 21 and table 4, the results of the last grid present a sharp drop. In more detail, the percentage deviation, between the results of the first three grid and the last grid, at time average drag coefficient and shedding frequency is less than 3% but in lift amplitude and drag amplitude is 25%and 50%, respectively. The latter implies that the last grid may predict phenomena that the other three grids cannot.

Moreover, in figure 22, the visualizations of spanwise and streamwise vorticity for each grid are presented. The first three grids (fig.22a-22c) predict the same flow structure. Here, the spanwise wavelength is πD and the streamwise vorticity follows a staggered arrangements. According to literature data, and as described in sub-section (1.2.1.1), these two factors are characteristics of mode A. However, for *Re*=300 the dominant shedding mode is the B. On the other hand, the last grid displays a totally different flow structure. Although it is difficult to determine the exact value of spanwise wavelength, we could say that it ranges from πD/3 to πD/4 (i.e. close to one cylinder diameter). The latter, combined with the fact that streamwise vorticity displays an inline arrangement, validates that the predicted shedding mode is the mode B. To that point, we could say that a grid consisting of at least 5 million elements is needed in order to predict the correct shedding mode

Table 4**:** Spatial resolution tests for *Re*=300. Values of time average drag coefficient $<C_D>$, lift coefficient amplitude $C_{L,AMP}$, drag coefficient amplitude $C_{D,AMP}$ and Strouhal number St for each grid.

N	$<C_D>$	$C_{L,AMP}$	$C_{D,AMP}$	St
2500000	1.309434	0.785898	0.044825	0.195969
3000000	1.309025	0.781974	0.044230	0.196024
4000000	1.305682	0.781260	0.045914	0.195367
5000000	1.266692	0.581673	0.022032	0.193170

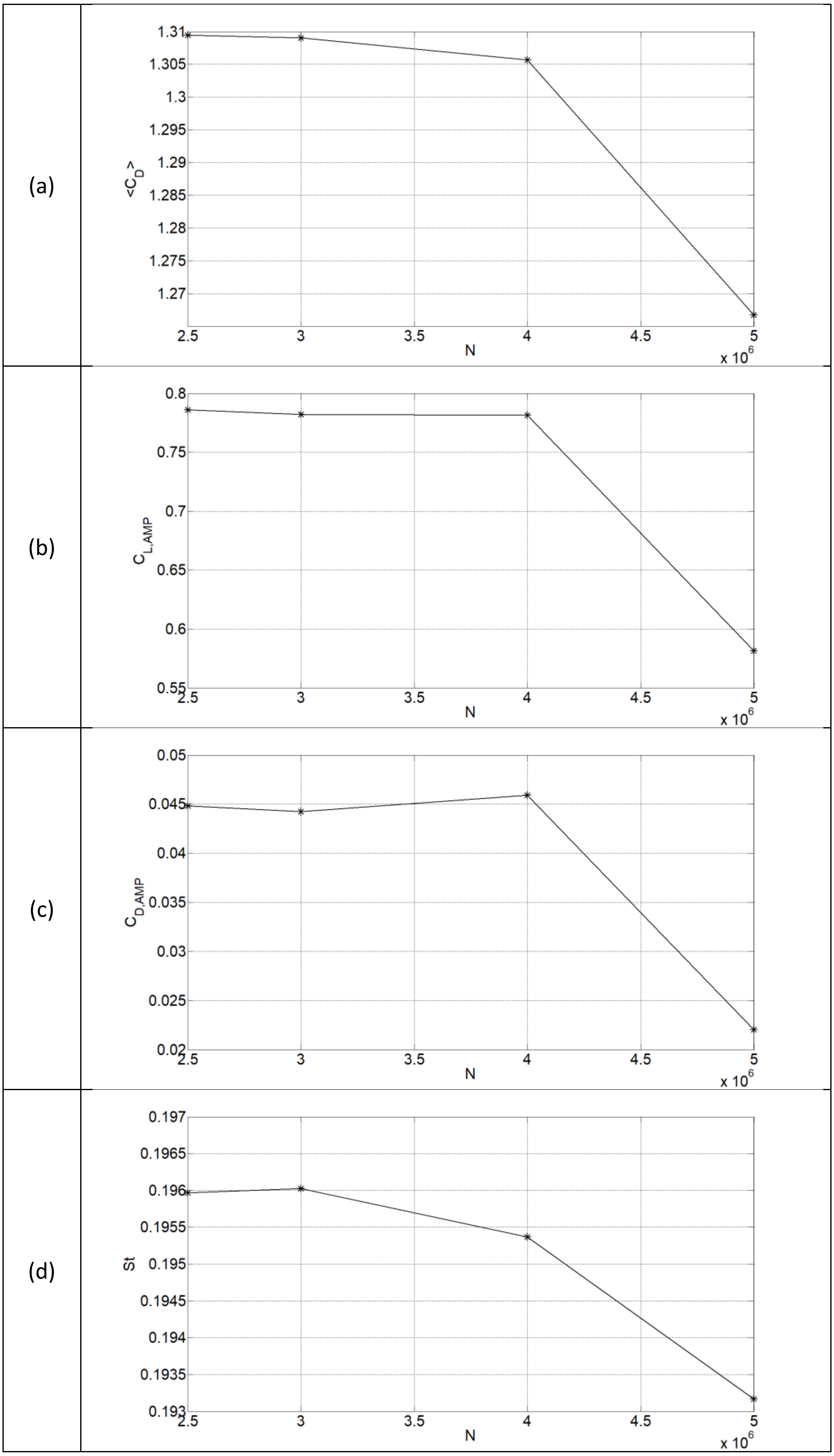

Fig. 21**:** Spatial resolution tests for *Re*=300. (a) Time average drag coefficient, (b) lift coefficient amplitude, (c) drag coefficient amplitude, (d) Strouhal number, versus number of elements of each grid.

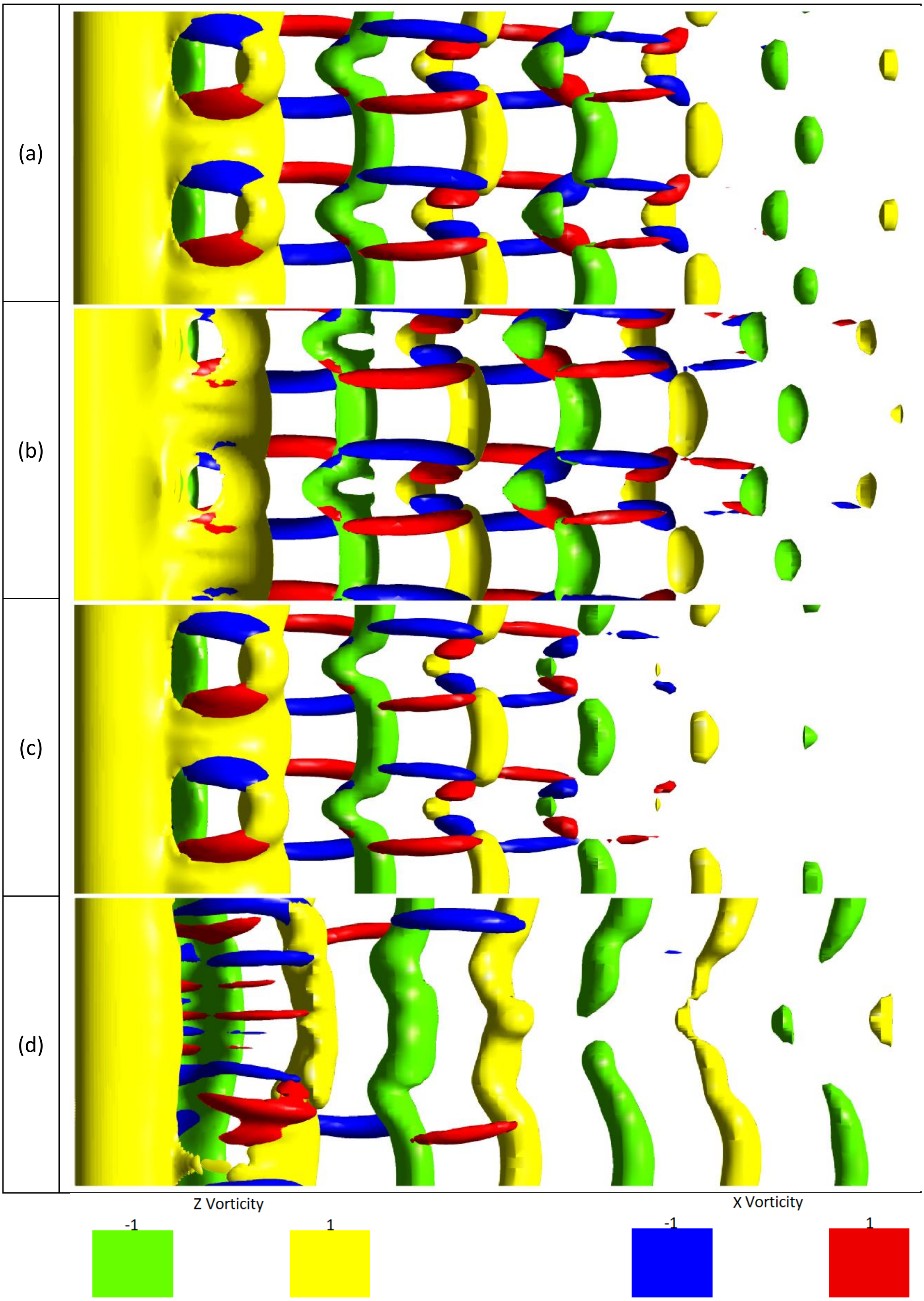

Fig. 22: Snapshots of instantaneous isosurfaces of spanwise (ω_Z) and streamwise (ω_X) vorticity for each grid. (a) Grid with 2.5 million elements. (b) Grid with 3 million elements. (c) Grid with 4 million elements. (d) Grid with 5 million elements.

4.1.2πD computational domain

As stated in the previous sub-section, the computation domain which extends 2πD in spanwise direction demands at least 5 million elements in order to predict the correct shedding mode at *Re*=300. However, the computational cost even of this grid is beyond the capabilities of the computational resources available to us. For this reason, we decide to reduce the size of the computational domain by half, introducing a domain which extends πD in Z direction. This domain enables us to maintain grid density equal to that of the previous domain and reduce the elements number by half. In addition, this domain can theoretical predict both shedding modes (i.e. mode A and mode B) because its thickness is close to wavelength of mode A and much greater than the wavelength of mode B. The latter is validated in the works of Kim and Kim (2010) and Labbe and Wilson (2007). Moreover, they pointed out that a computation domain with spanwise extension equal to πD is sufficient to predict all the characteristic components of the flow. Finally, analyzing their results, we could infer that narrower domains may lead to a slight increase at forces acting on cylinder and shedding frequency. In the next sub-sections, validation test for *Re* equal to 300 is *presented.*

4.1.2.1 Validation test *Re*=300

In this sub-section, the results of numerical simulations for *Re*=300 are validated by comparing them against published literature data. The characteristic components of the flow, which are taken into account, are the time average coefficient $<C_D>$, the amplitude of lift coefficient $C_{L,AMP}$, the shedding frequency in terms of *St* and the time average *Nu*. Moreover 3D features in the wake of the cylinder are compared with flow structures that others studies have predicted.

Table 5**:** Integral flow quantities for the present study and for literature studies at *Re*=300.

	$<C_D>$	$C_{L,AMP}$	St	$\overline{Nu_m}$
Present study	1.326	0.748	0.208	10.457
Labbe and Wilson (2007).	1.302	0.850	0.205	-
Peppa (2012)	1.251	0.532	0.196	-
Mastrokalos and Kaiktsis (2017)	1.275	0.735	0.194	10.800
Nakamura and Igarashi (2004)	-	-	-	10.645
Churchill and Bernstein (1977	-	-	-	9.935

The results of the present study and those of other works are presented in table 5. As regards the time average drag coefficient, the maximum percentage deviation, presented between the present results and those of Peppa (2012), is lower than 6%. This deviation may be non-negligible but it can be justified by the facts that a πD domain is used (decrease in domain thickness leads to increase of drag force) and that the results of the other studies have also a large scatter. Nevertheless, the greatest scatter, in literature data, is observed for the amplitude of lift coefficient. Here, the percentage in the deviation between the results of Labbe and Wilson (2007) and Peppa (2012) is close to 60%. However, the amplitude of lift coefficient, calculated in the present study, is close to the middle of the range of reported values. The shedding frequency follows the same trend with the drag force regarding the percentage deviation and scatter in literature data. Finally, the rate of heat transfer in terms of *Nu* presents an excellent agreement with both computational results of Mastrokalos and Kaiktsis (2017) and correlation of Nakamura and Igarishi (2004).

Figure 23 presents the visualizations of spanwise and streamwise vorticity from the works of Peppa (2012) (fig. 23a), Labbe and Wilson (2007) (fig. 23b) and present study (fig. 23c). In both literature studies, a computational domain that extends 2πD in spanwise direction has been used. However, the flow structure, predicted in the present study with a πD domain, demonstrates an excellent resemblance compared to those of the two other works. In particular, the spanwise wavelength in the present study is πD/4, and in the two other studies ranges between to πD/3.5 and πD/4. Moreover, primary vortices display the same deformation not only in the shedding region (region of vortex loops near to the cylinder) but also in the region far downstream. Finally, the above mentioned results are in total accordance with the experimental results of Williamson (1995), in which he provides visualizations of mode B.

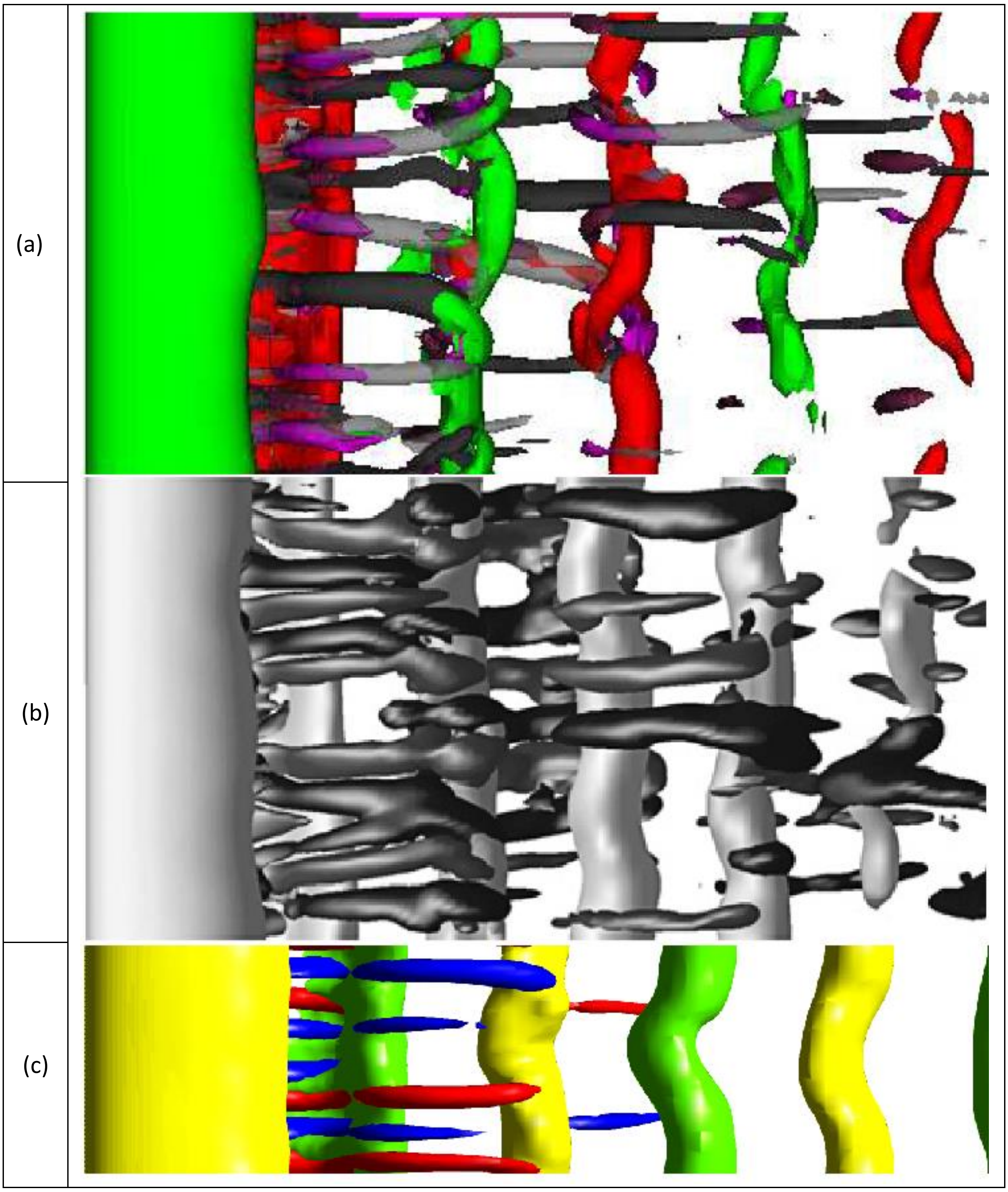

Fig. 23**:** Snapshots of instantaneous isosurfaces of spanwise (ω_Z) and streamwise (ω_X) vorticity. (a) Peppa (2012). (b) Labbe and Wilson (2007). (c) Present study.

5 Implementation of hydrophobicity – results

In this chapter hydrophobicity is implemented on the entire surface of the cylinder, aiming at the suppression of the Karman vortex street, as well as in heat transfer enhancement. First, the slip model is introduced and explained and then the results of this control method are presented for *Re*=300, and are discussed in detail.

5.1 Implementation of hydrophobicity

When hydrophobicity is implemented on the cylinder surface the common no-slip condition (zero tangential velocity) must be replaced with a model that provides a nonzero tangential velocity, called slip velocity. In the present study, hydrophobicity is modeled utilizing the Navier model (eq. 12). The slip length is assumed to independent of the flow characteristics (i.e. consists the unique parameter that quantifies hydrophobicity). Finally, the boundary condition on the cylinder surface can be defined in terms of non-dimensional circumferential, u_θ, radial, u_r, and axial direction, w, as follows.

$$u_\theta = \tau b^* Re = b^* \left(\frac{\partial u_\theta}{\partial n}\right)_w \;, u_r = 0 \;, w = \tau b^* Re = b^* \left(\frac{\partial w}{\partial n}\right)_w$$

Where:
τ: Non-dimensional shear stress
b*: Non-dimensional slip length b*=b/D.

5.2 Computational results

In order to investigate in detail the effect of hydrophobicity on the flow structure and heat transfer, numerical simulations ware performed for a sufficient large range of slip lengths. Hydrophobicity was uniformly distributed on the entire cylinder surface and the non-dimensional slip lengths which were tested were b*=0, 0.02, 0.05, 0.1, 0.2, 0.3 and 0.4 (b*=0 denotes the uncontrolled case). Finally, all simulations ware performed for *Re*=300 where the flow is 3D and the dominant shedding mode is the mode B. The next two paragraphs present the effect of hydrophobicity on the flow structure, integral flow quantities and heat transfer, as well.

5.2.1 Flow structure and characteristic flow quantities

Figure 25 presents the time average drag coefficient (25a), the amplitude of lift (25b) and drag (25c) coefficient and the non-dimensional shedding frequency (25d) as a function of non-dimensional slip length. Here, the results are in total agreement with those of You and Moin (2007) and Mastrokalos and Kaiktsis (2017). They investigated the effect of slip length values equal to 0.02 and 0.2, respectively. In more detail, fig (25a) verifies that the implementation of hydrophobicity can extremely reduce the drag force. Moreover, it is clear that drag displays a sharp reduction for relatively low values of slip length and trends to approach a limit value for moderate and high slip lengths. Figure 25b and 25c illustrate the effect of hydrophobicity on unsteadiness and fluctuating forces. Drag and lift amplitude decrease sharply for slip lengths ranging from b*>0 to b*<0.1 and approach zero for b*>0.2. For b*=0.3 the amplitudes of force coefficients are zero which implies that vortex street have been totally suppressed. The latter is also validated in figure 25c which shows that for b*=0.3 stops the shedding from the cylinder. In addition, in three last figures, a discontinuity is observed in the region between b*=0.02 and b*=0.1. As shown in next figures this discontinuity may be associated with flow structure and especially the shedding mode.

Furthermore, figure 24 presents the time average pressure, viscous and total drag coefficient versus slip length. It is clear that viscous drag sharply decreases for small slip lengths and approaches a limit value for high slip lengths. Moreover, the shape of this curve is identical with the *Re*-$C_{D,viscous}$ which means that the increase of slip length affects viscous drag such as the increase of *Re*. In other words, the implementation of hydrophobicity increase the effective *Re* for viscous drag. Finally, the curve of viscous drag does not present discontinuities such as the other two curves. The latter is attributed to the fact that viscous drag is not affected by the flow structure. On the other hand, pressure drug also decreases with the increase of b*, which means that hydrophobicity decreases the effective *Re* for pressure drag. To that point, it is worth to mention that pressure drag is mainly responsible for the value of total drag as the viscous drag has negligible contribution. However, this is common for bluff body flows and moderate *Re* values.

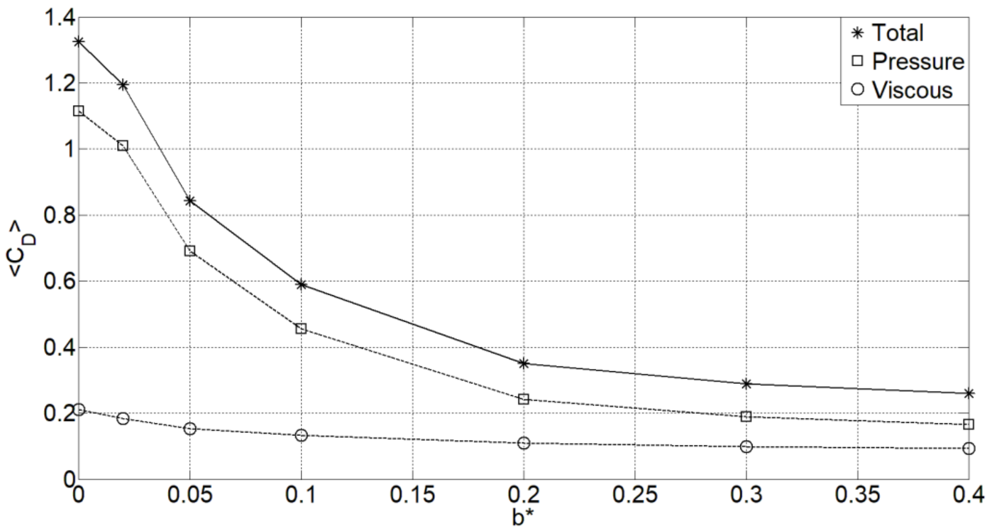

Fig. 24: Comparison between time average total, pressure and viscous drag coefficient for each slip length considered.

Furthermore, figure 26 illustrates the instantaneous spanwise vorticity at an XY plane (Z=0). It is clear that the intensity of primary vortices decreases with the increase of slip length. In particular, for b*=0 and b*=0.02 flow displays the same structure but for b*=0.02 vortices weaken faster; this trend can be observed at the far wake. Flow, for b*=0.05, presents a slight

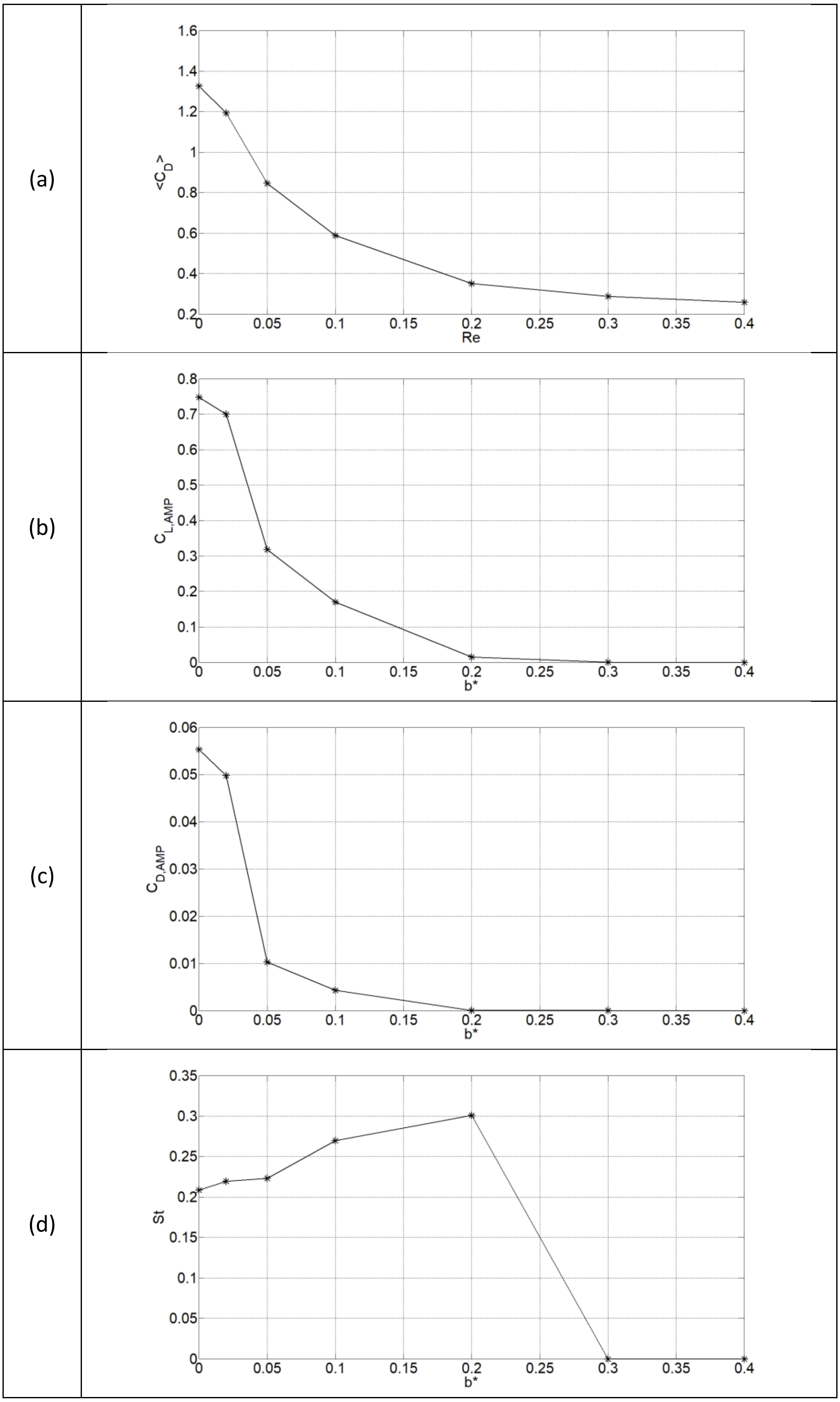

Fig. 25: Results of hydrophobicity implemented on the entire cylinder. (a) Time average drag coefficient, (b) lift coefficient amplitude, (c) drag coefficient amplitude, (d) Strouhal number, versus non-dimensional slip length.

different structure as the vortices are more spatially spread. However, here, the effect of hydrophobicity starts being clear for slip length equal to 0.1. At this slip length, the delayed vortex shedding is observable as the vortex bubble stretches downstream and the wake became narrower. In addition, the point at which the vortex shedding take place moves downstream with the increase of slip length. Finally, for b*=0.3 the flow is totally stable as the Karman vortex street have been suppressed. In this regime, recirculation zones appear in the wake the length of which decreases with the increase of b*

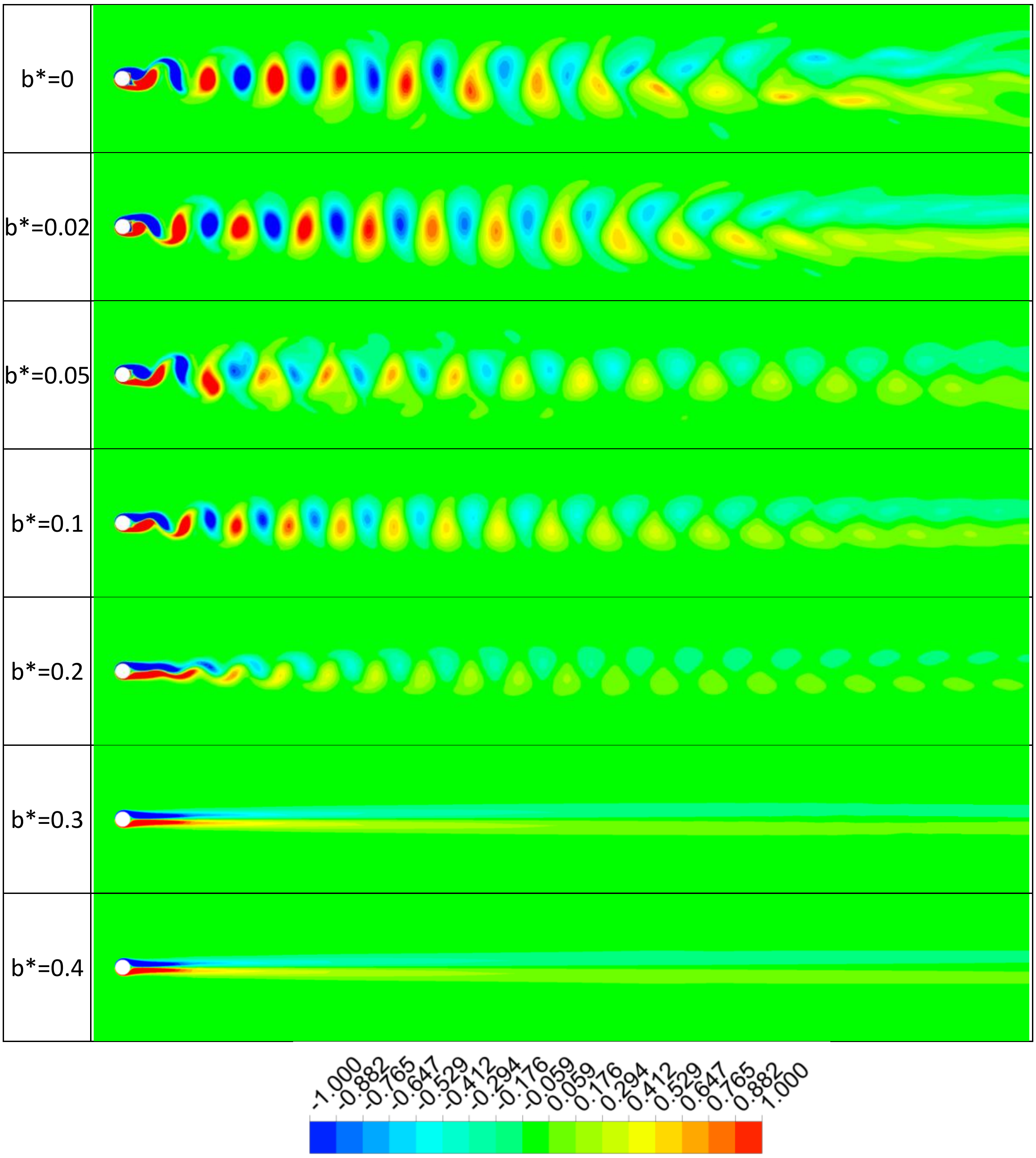

Fig. 26: Snapshots of instantaneous spanwise vorticity (ω_Z) at XY plane for each non-dimensional slip length considered.

Finally, figure 27 presents flow visualization in terms of instantaneous isosurfaces of streamwise and spanwise vorticity. The first two cases (i.e. uncontrolled case and hydrophobicity with slip length equal to 0.02) display the same flow structure and the

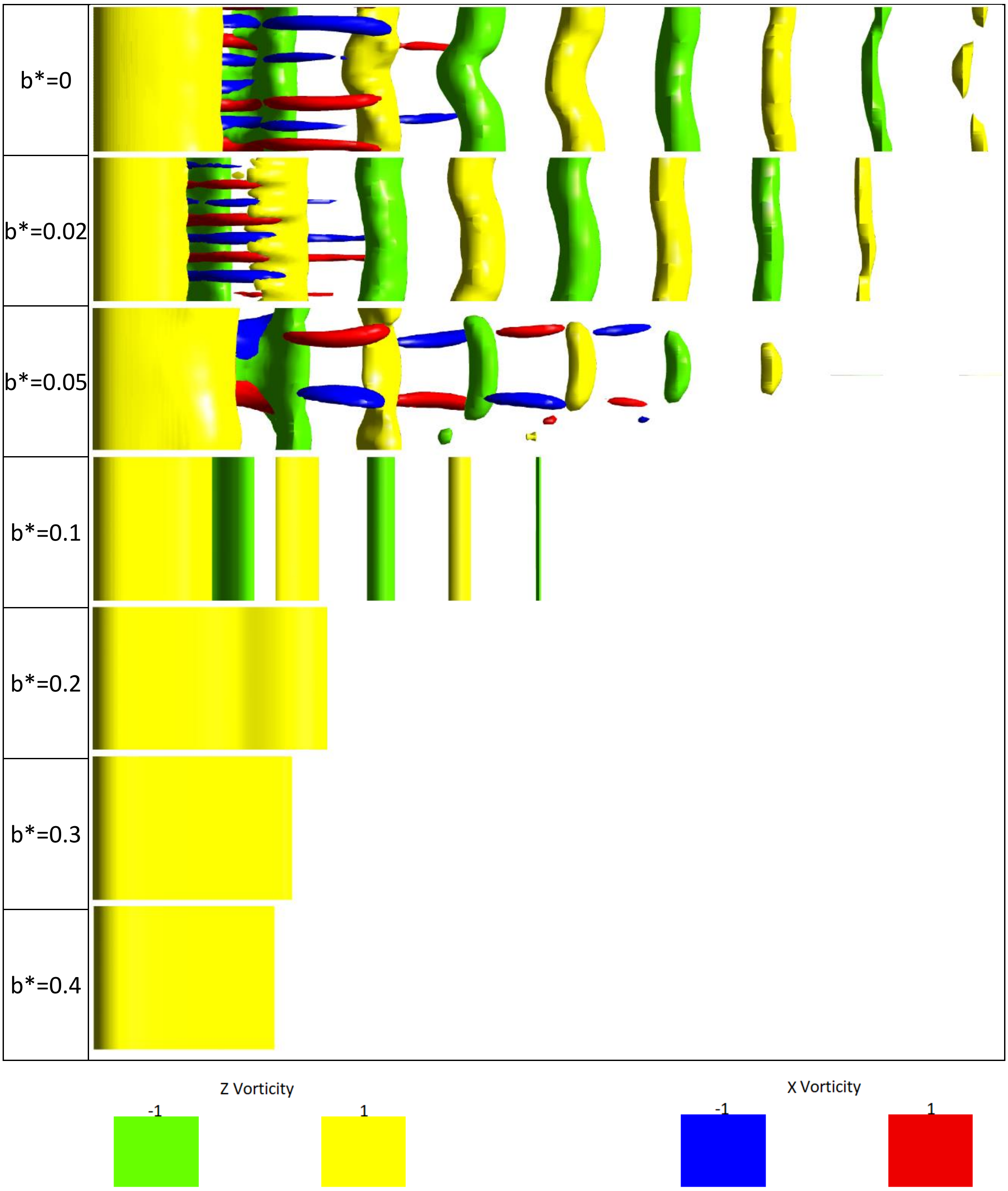

Fig. 27: Snapshots of instantaneous isosurfaces of spanwise (ω_Z) and streamwise (ω_X) vorticity for each slip length considered.

differences between them are due to phase difference, which is close to half period. This flow structure is representative of mode B of shedding, validated in the previous chapter. The third case presents totally different flow structure as the wavelength of spanwise periodic pattern is πD. The latter, combined with the fact that streamwise vortices follow a staggered arrangement, denotes that for b*=0.05 the mode A occurs. In addition, visualization from the computational work of Thompson et al (2000) and experimental work of Williamson (1995) validate that the occurring flow type is characteristic of mode A. To that point, it is worth to mention that the discontinuity in b*-St curve, for b*=0.05, may occur because mode A is the dominant shedding mode in this region. This assumption stems from the presence of similar discontinuity in Re-St curve in the region of mode A. However, in order to draw a solid conclusion more simulations are needed in this region. Furthermore, for slip length equal to 0.1, the flow becomes 2D. This is verified by the absence of streamwise vorticity and deformation of spanwise vortex tubes. Finally, for b*=0.2, vortex tubes disappear from the present visualization as their absolute vorticity is less than unity.

5.2.2 Heat transfer

Figure 28 presents the time average *Nu* as a function of non-dimensional slip length. Here, it is verified that the implementation of hydrophobicity can improve heat transfer rates. In particular, figure 28 shows that a slight increase in slip length results in a large increase of Nu, for small slip lengths. However, as the slip length increases, its contribution to heat transfer enhancement reduces. As a result, hydrophobicity is more efficient for small and moderate values of slip length. On the other hand, hydrophobicity becomes ineffective for large slip length (i.e. b*=0.1-0.2); for example doubling the slip length in this region returns a slight increase of *Nu*. To that point, it should be noted that *Nu* seems to be independent of changes in the flow structure, as the b*-*Nu* curve does not display discontinuities. However, discontinuities may be present, but may be not observable as in other plots. Finally, it is worth mentioning that an excellent agreement between the present results and those of Mastrokalos and Kaiktsis (2017) is demonstrated.

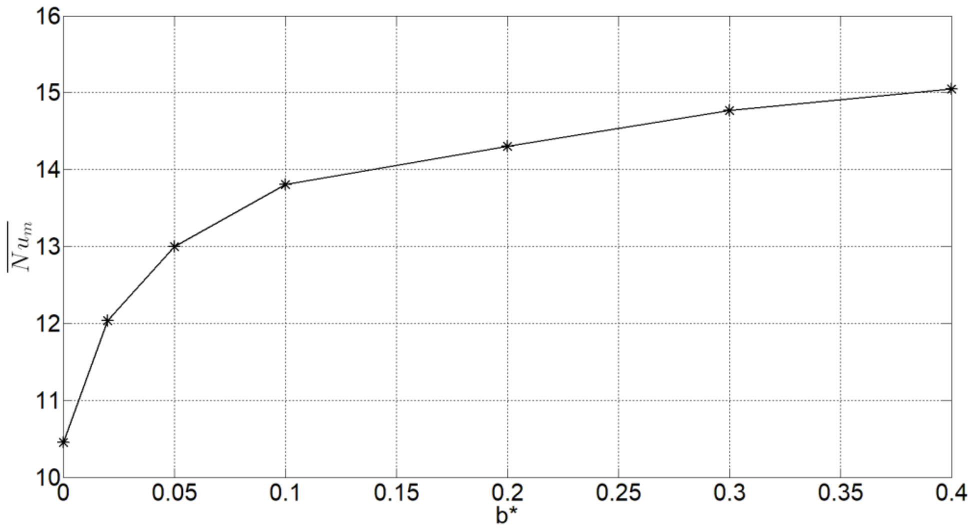

Fig. 28**:** Time average *Nu* versus non-dimensional slip length.

Moreover, figure 29 presents snapshots of instantaneous *Nu* distribution on cylinder surface for each slip length. For each case, two regions of the cylinder are presented, the region of the front stagnation point (denoted by F.S.P.) and the region of rear stagnation point (denoted by R.S.P.). Regarding the F.S.P. region, *Nu* increases with the increase of slip length for small b* (i.e. b*=0.1). However, for higher slip length values increase of b* returns a slight increase of *Nu* but a large spread of the area of high *Nu*. The latter denotes that thermal boundary layer attains a minimum thickness and after that increase of slip length leads boundary layer to maintain this thickness downstream. On the other hand, the *Nu* distribution

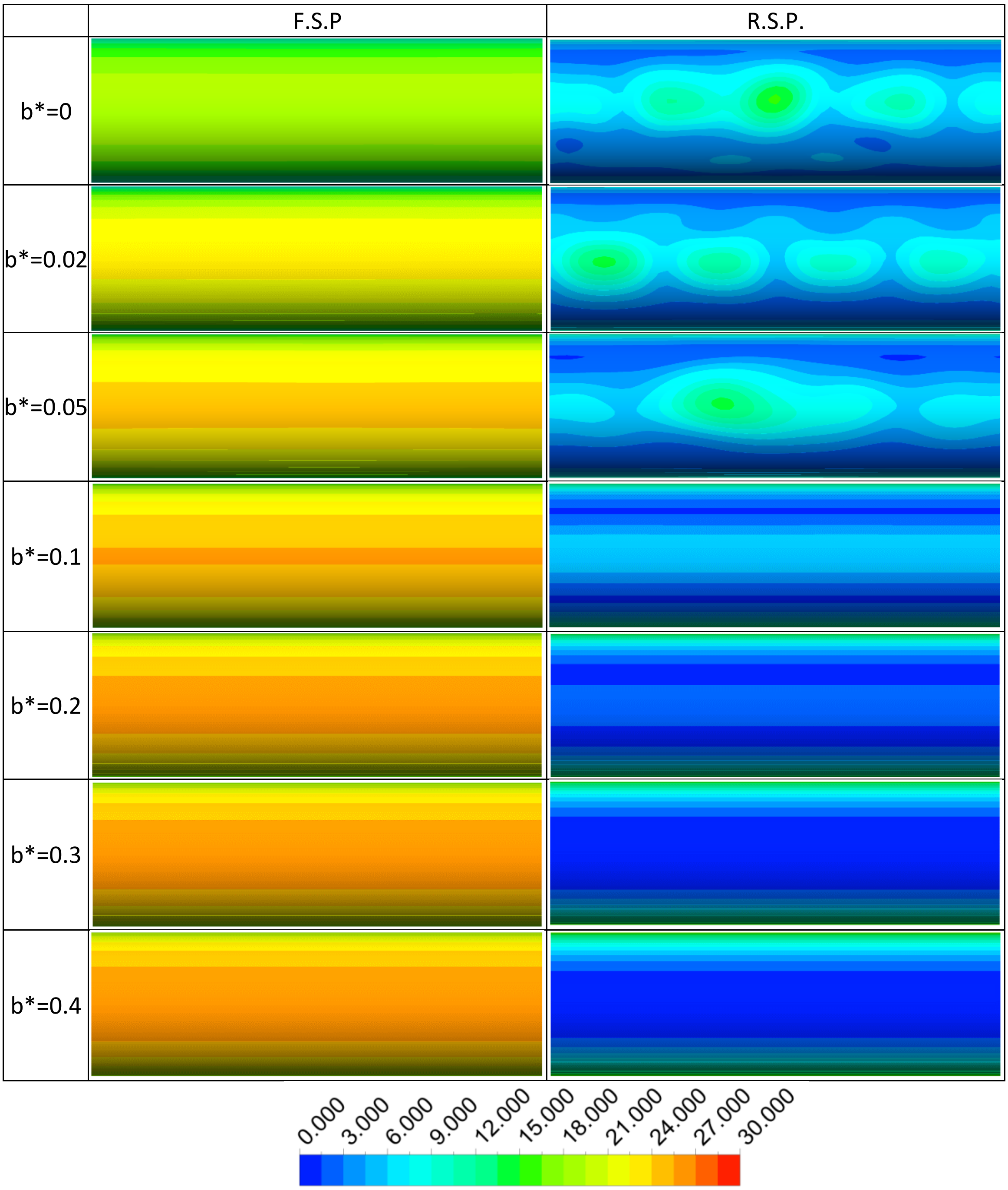

Fig. 29: Snapshots of instantaneous *Nu* distribution for each non-dimensional slip length considered.

at the region of rear stagnation point presents a different pattern. For b*=0, 0.02 and 0.05, a local maximum is observed at rear stagnation line. This maximum does not present a uniform distribution across the line but a periodic pattern whose wavelength is equal to the characteristic wavelength of the flow (i.e. equal to πD/4 for the first two cases and πD for the third case). This phenomenon caused by the primary vortices which present spots of earlier formation on cylinder surface increasing *Nu* at that point. For b*=0.1 and 0.2, *Nu* continuous to display a local maximum at rear stagnation line but it follows a uniform distribution across the line. The latter is caused by the suppression of three-dimensionality. Finally, for b*=0.3

and 0.4, the full cancellation of vortex street result in the disappearance of the local maximum at the rear stagnation line. To that point, it should be noted that increase of b* results in decreased values of *Nu* at the rear stagnation region.

Finally, figure 30 and 31 present the instantaneous temperature distribution at XY plane and the instantaneous isosurfaces of temperature equal to 0.04, respectively. It is obvious that temperature distribution follows similar structure with the vorticity distribution. This is attributed to the fact that the vorticity emanates from the region of cylinder where thermal energy is transferred to the fluid. On the other hand, temperature distribution shows that increase of b* reduce the transfer of energy within the medium. The latter can be explained by the fact that hydrophobicity suppresses the unsteadiness in the wake reducing the flow mixture. Indeed, in two last cases, heat is transferred only by diffusion in the far wake.

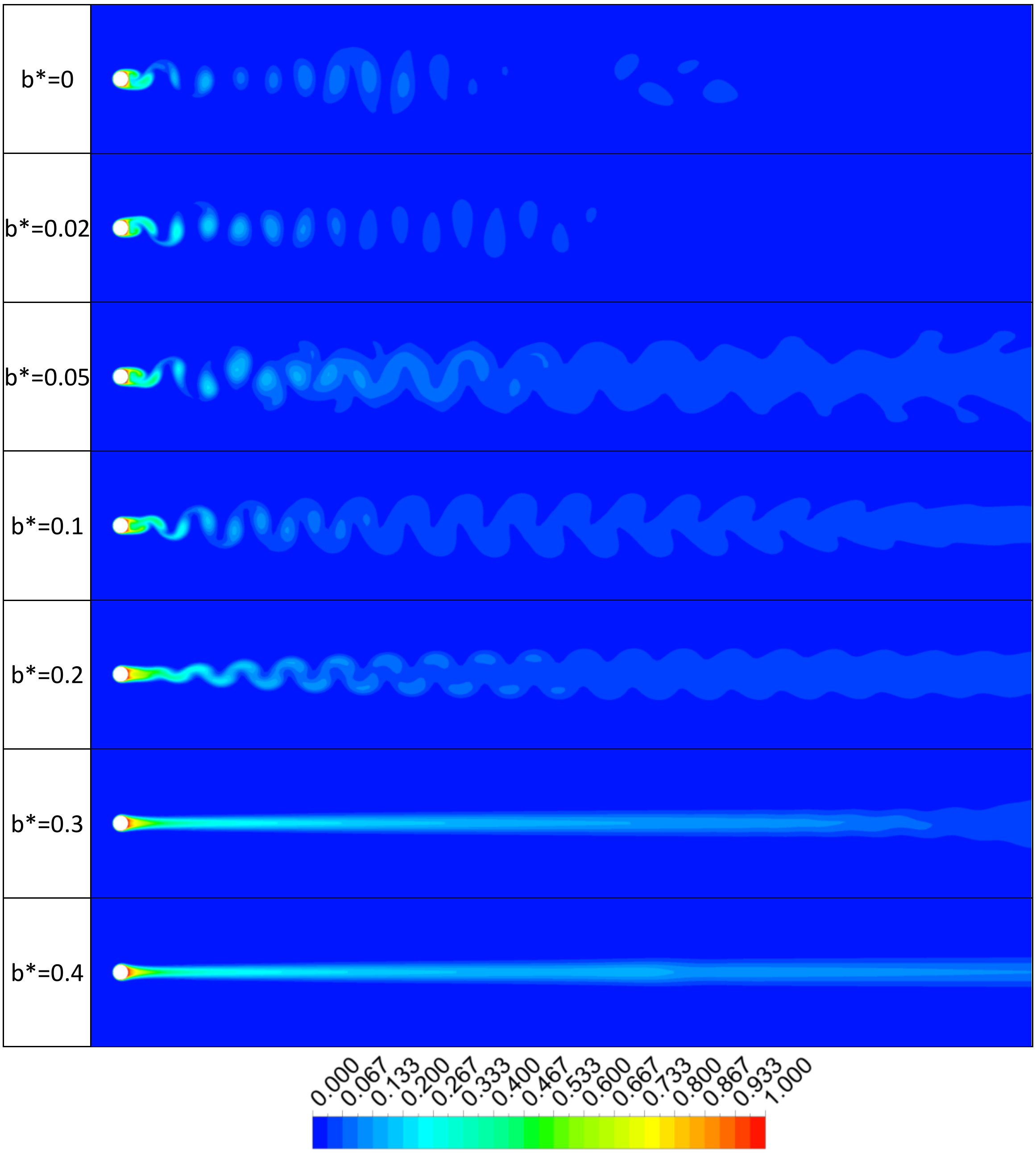

Fig. 30: Snapshots of instantaneous temperature distribution at XY plane for each non-dimensional slip length considered.

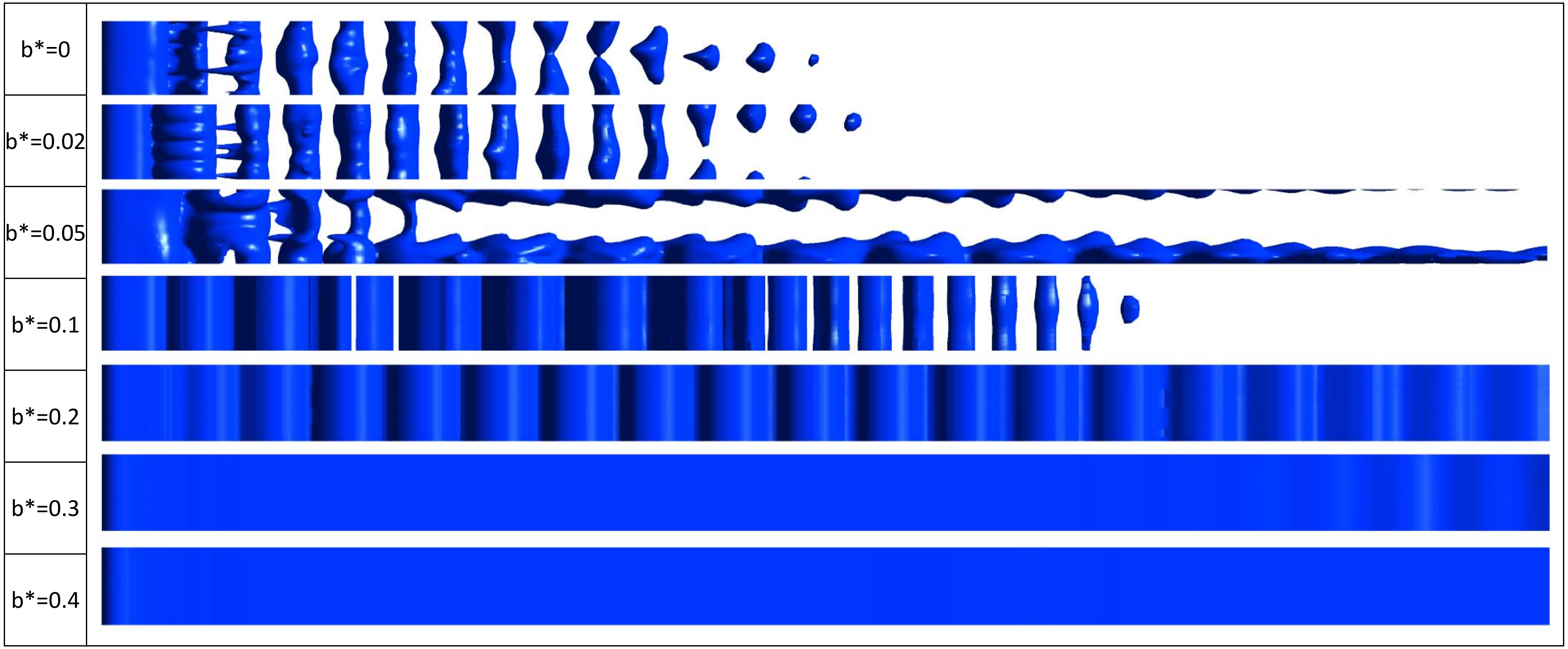

Fig. 31**:** Snapshots of instantaneous isosurfaces of temperature T=0.04.

5.2.3 Comparison between 2D and 3D results

Figure 33 presents the comparison between the results of 2D and 3D simulations for characteristic flow quantities. In more detail, these quantities are the time average drag coefficient (33a), the amplitude of lift (33b) and drag (33c) coefficient and the non-dimensional shedding frequency (33d) as a function of non-dimensional slip length. As shown in figure 28a, the 2D simulation slightly overpredicts the time average drag coefficient for the cases in which the flow is 3D. On the other hand, the other four cases evidently present identical results. The cause of this overprediction is that the 2D simulation imposes that the advection and diffusion of momentum takes place only on an XY plane. In more detail, setting the reference frame on the cylinder, initially the flow has momentum only in X direction. However, the cylinder causes the transfer of momentum to the other directions. When the natural flow is 2D the 2D simulation can accurately predict the transfer of momentum, however, when the natural flow is 3D the 2D simulation, not taking into account the transfer of momentum in Z direction, predicts stronger flow in XY plane (i.e. greater velocities and vortex stream which corresponds to higher *Re*) leading to the increase of drag. This is more prominent in the case of the amplitudes of lift and drag coefficient. As shown in figure 28b and 28c, 2D simulation fails to predict the correct amplitudes and also the predicted curve is smoother than the actual. This is attributed to the fact that the discontinuities are caused by the different shedding modes, which the 2D simulation cannot predict. Finally, it is observed, especially from the figure 33c, that the deviation between the 2D and 3D results is higher for b*=0.05. This is due to the presence of mode A in this region. In particular, as stated in chapter 1, mode B is more spanwise uniform than mode A. This means that the flow structure of mode B is closer to the 2D structure than the mode A.

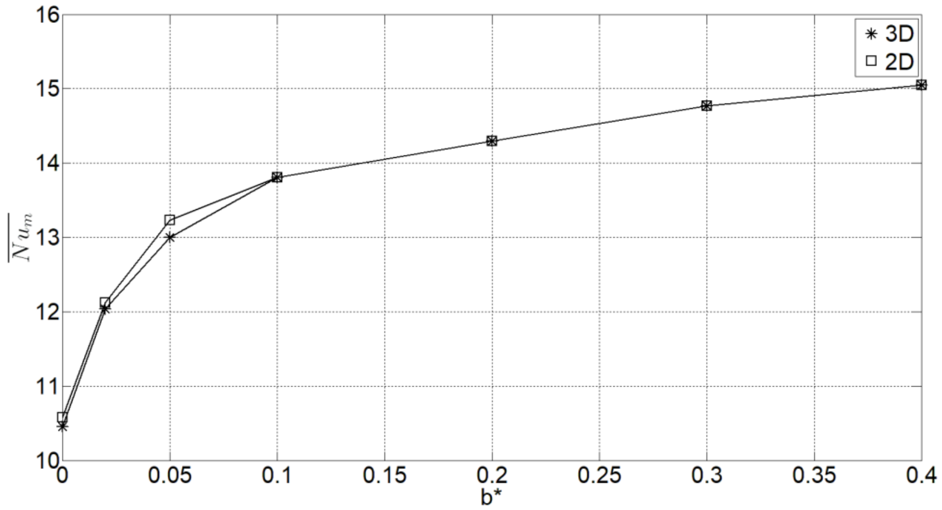

Fig. 32: Comparison between the results of 2D and 3D simulations for the time average *Nu* versus non-dimensional slip length.

Regarding the heat transfer rates that the two sets of simulations predict, figure 32 present the comparison of time average *Nu*. Here, the deviation between the values of 2D and 3D simulations is relatively low and for that reason 2D simulation can give very good estimations for the heat transfer. This is due to the relatively low dependency of *Nu* from the 3D structure as it is by far weaker than the primary vorticies.

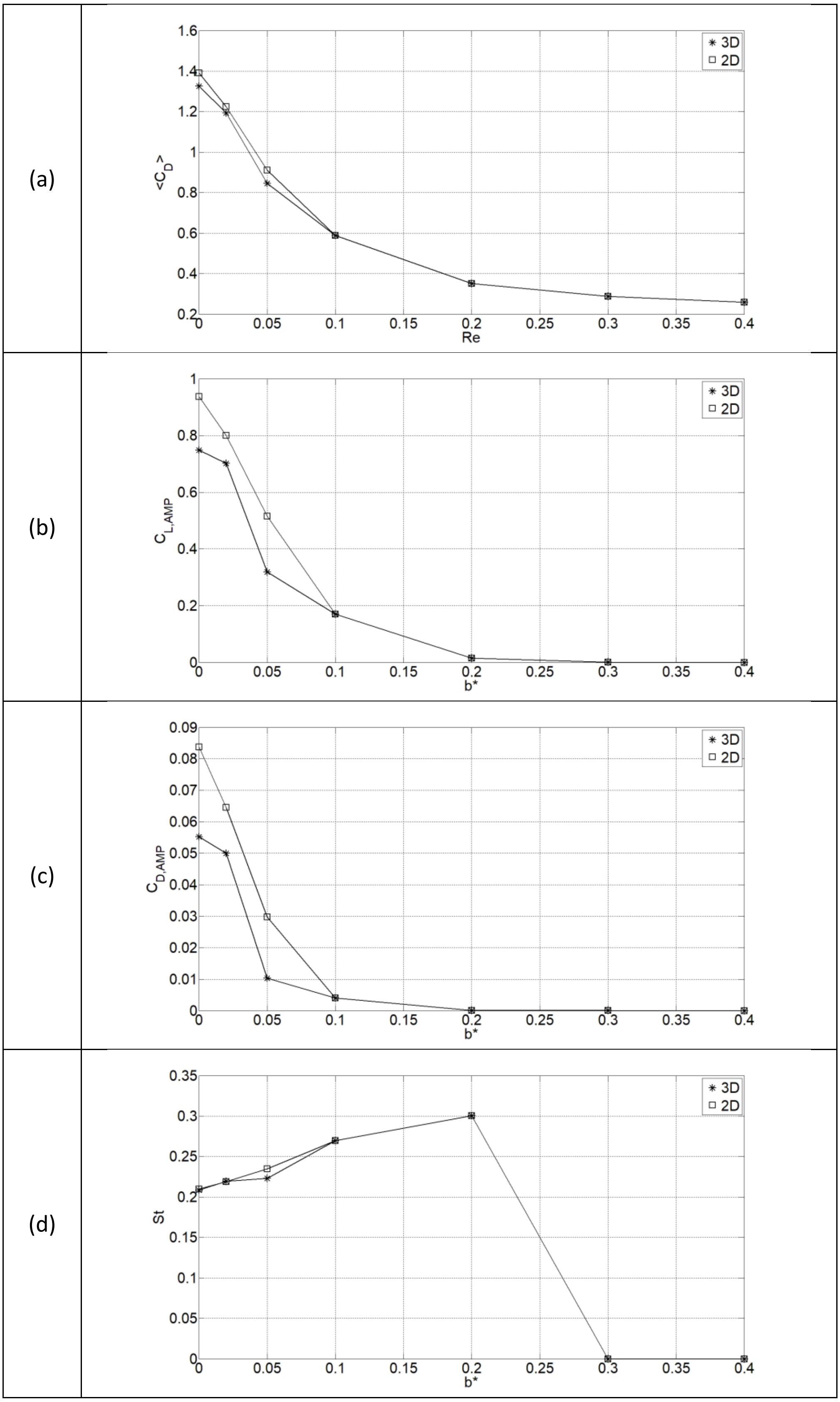

Fig. 33: Comparison between the results of 2D and 3D simulations. (a) Time average drag coefficient, (b) lift coefficient amplitude, (c) drag coefficient amplitude, (d) Strouhal number, versus non-dimensional slip length.

6 Implementation of circumferential hydrophobic bands

In this chapter, numerical simulation results are reported, corresponding to implementing alternating circumferential bands of slip and no-slip conditions. All simulations were performed for *Re*=300 and slip length equal to 0.02. The selection of this slip length is due to the three following facts. As shown in the previous chapter, in this region the effect of hydrophobicity on the flow stabilization and the heat transfer enhancement, compared to the control effort, is higher than other regions. In addition, this slip length corresponds to a feasible value because, appropriately fabricated, superhydrophobic surfaces display micrometer scale slip length (up to ~100μm) (i.e. this slip length correspond to a cylinder diameter about five millimeters). Finally, for this slip length, we can partially compare our results with those of You and Moin (2007) as they investigated the effects of hydrophobic bands, consisting of b^*=0.02, on the flow quantities. In the present study, we examined the effects of three different arrangements (fig.34). In these three cases, the bands had a width equal to $0.5\lambda_z$, λ_z and $2\lambda_z$, respectively (where λ_z is the spanwise wavelength equal to $\lambda_z=\pi D/4$). It should be noted that, in all cases, the area of the cylinder, at which hydrophobicity has been implemented, is the half of total area. The aim of this simulation is to investigate whether a reduction of the control effort by half could lead to a comparable with the full slip case regarding the flow quantities and heat transfer rates. In the next section, the results of the above mentioned simulations are presented and described in detail.

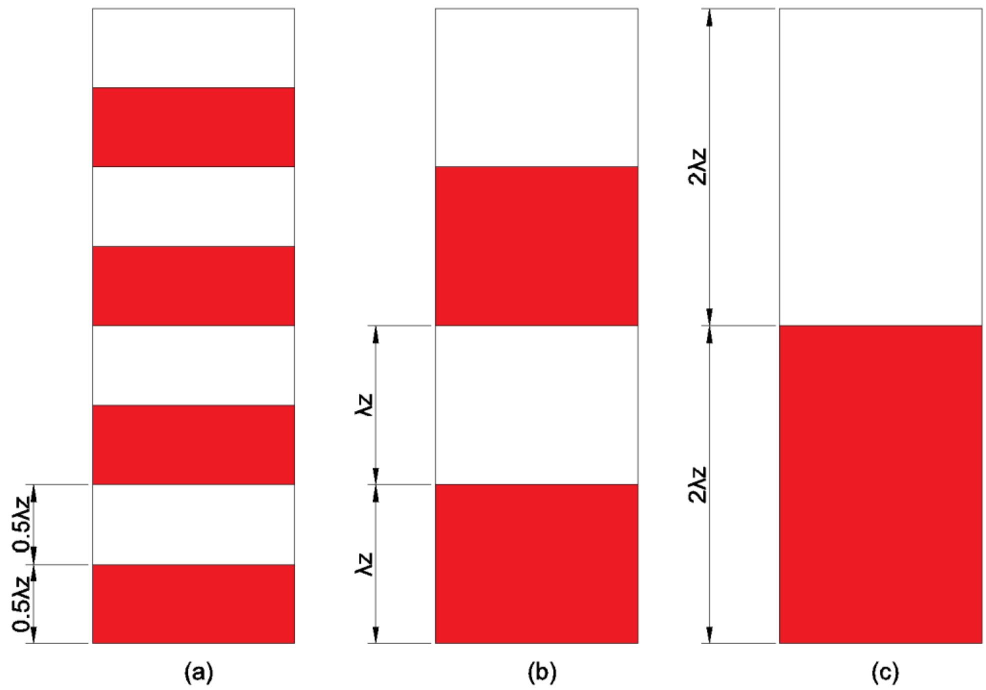

Fig. 34**:** Sketch of surface hydrophobicity patterns for the cases of the present study; red and white areas correspond to hydrophobic and non-hydrophobic regions, respectively.

6.1 Flow structure and characteristic flow quantities

Figure 35 presents the characteristic flow quantities, for the three cases considered, versus the percentage of hydrophobic area. In the figure, the uncontrolled case and the full slip case are included. . In more detail, these quantities are the time average drag coefficient (35a), the amplitude of lift (35b) and drag (35c) coefficient and the non-dimensional shedding frequency (35d). As regards the time average drag coefficient (fig.35a), the first two cases presents similar results and their values are close to the middle of the results of uncontrolled and full slip cases. However, case (c) presents great reduction at time average drag coefficient as the value of drag is even smaller than those of full slip case. In particular, case (c) display 15% reduction from uncontrolled case and 6% reduction from full slip case. This means that with the case (c) arrangement we can achieve lower drag by 6% using the haft control effort which results in the decrease of the associate cost. It should be noted that the cause of this drag reduction is the increase of flow instability. In other words, the increase of the band width results in higher flow mixture in Z direction. This means that the net momentum in XY plane is lower which leads to a weaker vortex street decreasing the drag force. This is more prominent in case of amplitudes of lift and drag coefficient. For example, the amplitude of lift coefficient in case (c) presents 52% reduction from the uncontrolled case and 49% reduction from the full slip case. In addition, the amplitude of drag coefficient presents even greater reduction (83% from uncontrolled case and 81% from the full slip case). Nevertheless, it should be noted that the amplitude of drag coefficient in figure 35c corresponds to the base frequency (i.e. double the shedding frequency). However, due to the high instability of the flow, in case (c), the drag signal is not a pure sine wave and low frequency harmonics appear. The amplitude of these harmonics is the same order of magnitude or slightly greater that the amplitude of base harmonic. The later implies that rms (route mean square) values are needed in order to produce reliable results. Indeed, if we compared the rms values the reduction would be close to those of amplitude of lift coefficient. Finally, as shown in figure 35d, shedding frequency presents a large reduction as it is lower than the shedding frequency of uncontrolled case. This is may be may be associated with flow structure and especially the shedding mode. Finally, it is worth to mention that in contrast to the presents study You and Moin report that the case (b) presents the best results regarding the time average drag coefficient and the amplitude of lift coefficient. However, this deviation may be due to the differences of computational domains.

Figure 36 illustrates the flow structure at XY plane with color-coded contours of instantaneous spanwise vorticity. Here, the flow structure is similar for all cases except from case (c). In particular, case (c) presents deformed vorticies (relatively to those of the other cases) and their magnitude is significant lower than in other cases. This is observable not only in the far wake but also in the region close to cylinder. The later validates the statement that the increase of flow instability by the implementation of hydrophobic bands results in the creation of a weaker vortex street. As regards the cases (a) and (b) the differences in their flow structure are negligible which interprets the small deviation in their results.

Finally, figure 37 presents the 3D flow structure, visualizing the isosurfaces of spanwise and streamwise vorticity. Here, the uncontrolled case and the case (a) present identical flow structure in both spanwise and streamwise vorticies. Ii this case, the alternating bands fails to destabilize the flow because the wavelength of the periodic pattern (one period includes two bands one hydrophobic and one hydrophilic) is equal to the natural wavelength

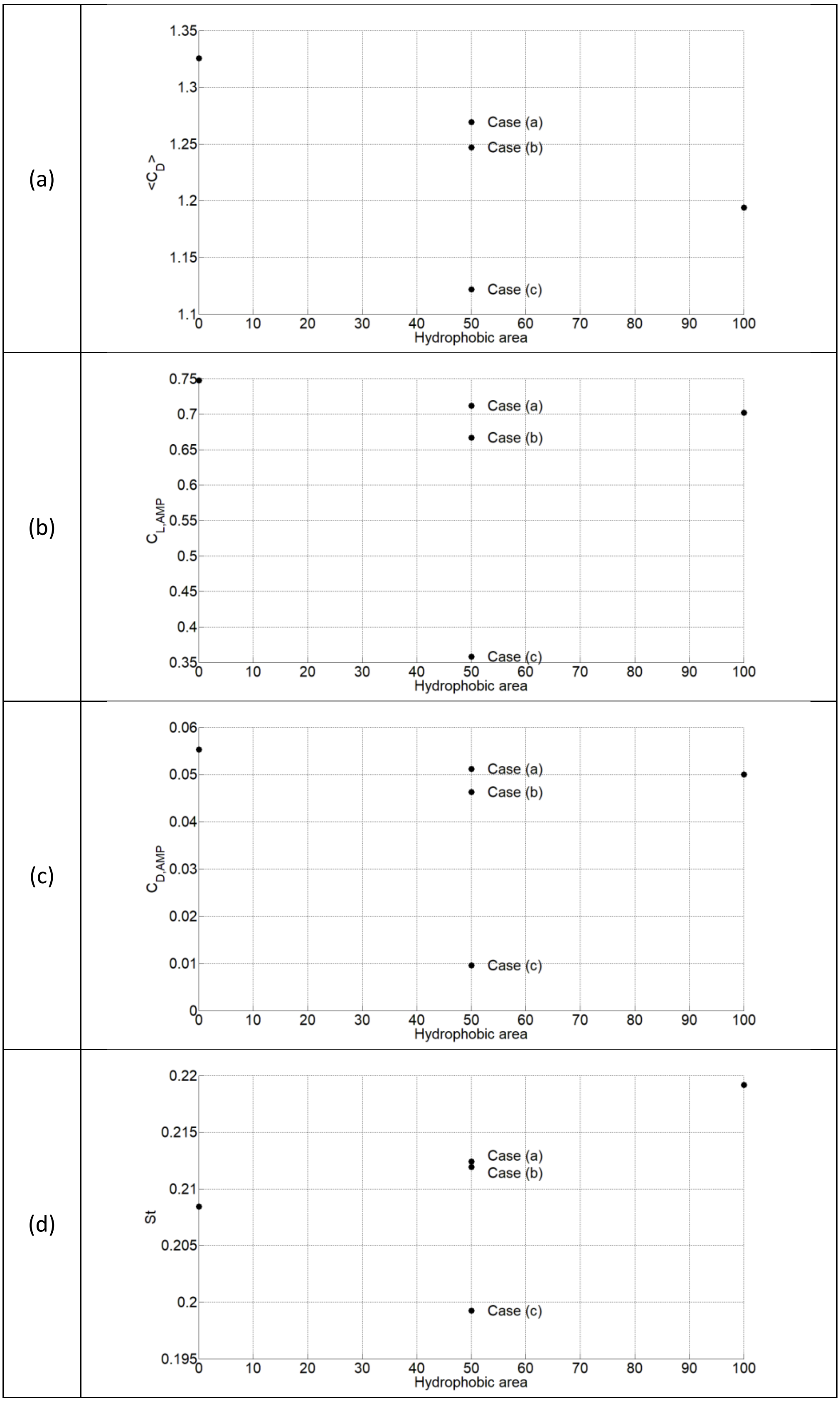

Fig. 35: Results of alternating bands of hydrophobicity implemented on cylinder (full slip and no-slip cases are included). (a) Time average drag coefficient, (b) lift coefficient amplitude, (c) drag coefficient amplitude, (d) Strouhal number, versus the percentage of hydrophobic area.

of the flow $\lambda_z=\pi D/4$. However, this arrangement may slightly strengthens the mode B but in order to observe that small change more accurate methods than visualizations are needed. For example, plotting the spectrum of velocity of a point in the wake or the spectrum of integral flow quantities such as drag coefficient, we may observe change in the amount of energy or shifting of the main energy to other frequencies. Moreover, case (b) presents similar flow structure with the uncontrolled case and the case (a) as the dominant shedding mode is the mode B. Nevertheless, it is clear that some streamwise vorticies are stronger than others. This is attributed to the fact that the wavelength of hydrophobic bands is double the natural wavelength, perturbing the flow stability. However, this perturbation cannot achive, as shown in the figure 37, destabilization of the flow. On the other hand, case (c) presents a total destabilized flow. Here, the dominant shedding mode is the mode A as the distance between two streamwise vorticies with the same rotation is πD and the vorticies follow a staggered arrangement. To that point it should be noted that the mode B has not disappeared but its contribution in the flow formation is negligible. The arrangement of case (c) achive to alter the shedding mode because its wavelength is equal to the natural wavelength of mode A.

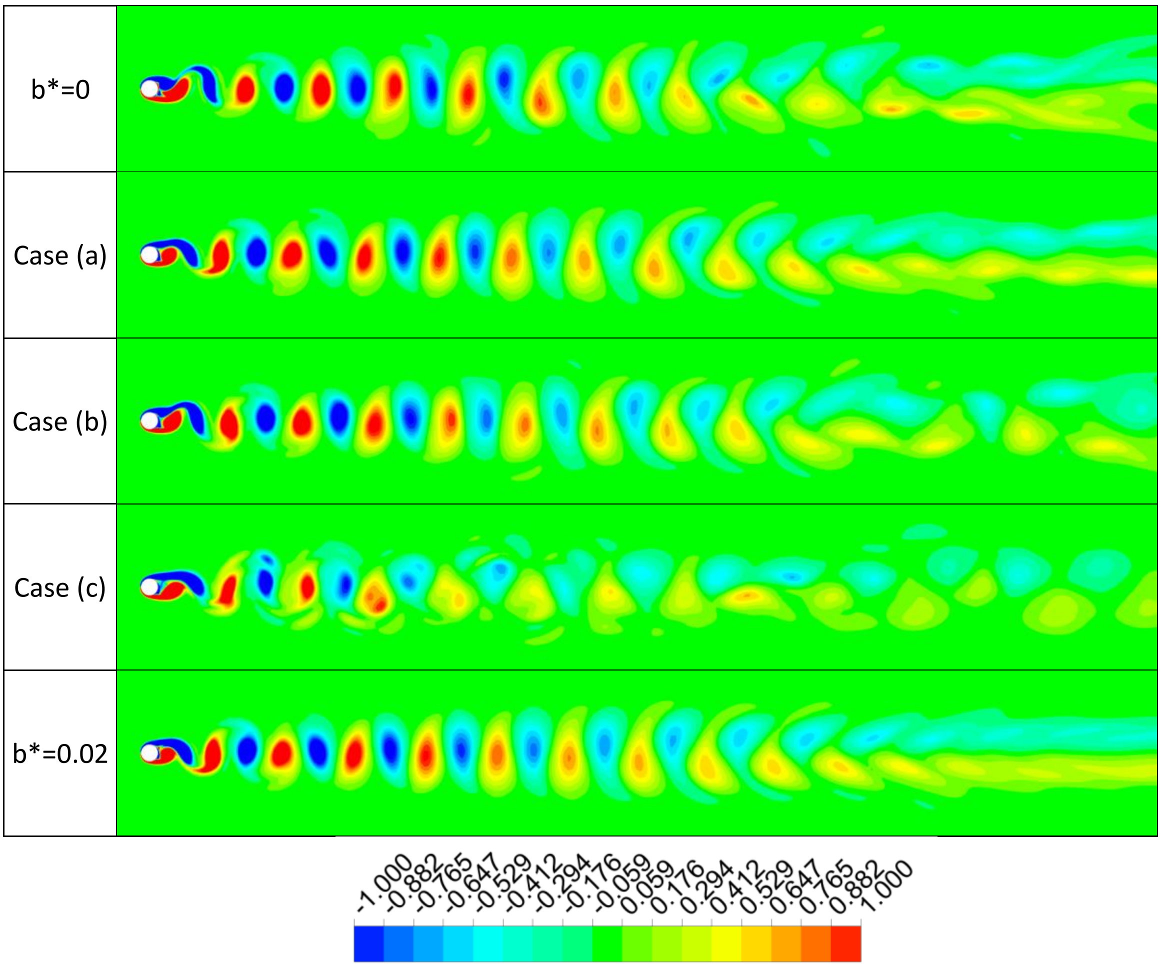

Fig. 36**:** Snapshots of instantaneous spanwise vorticity (ω_z) at XY plane for each case considered. The uncontrolled case (b*=0) and the full slip case (b*=0.02) are included.

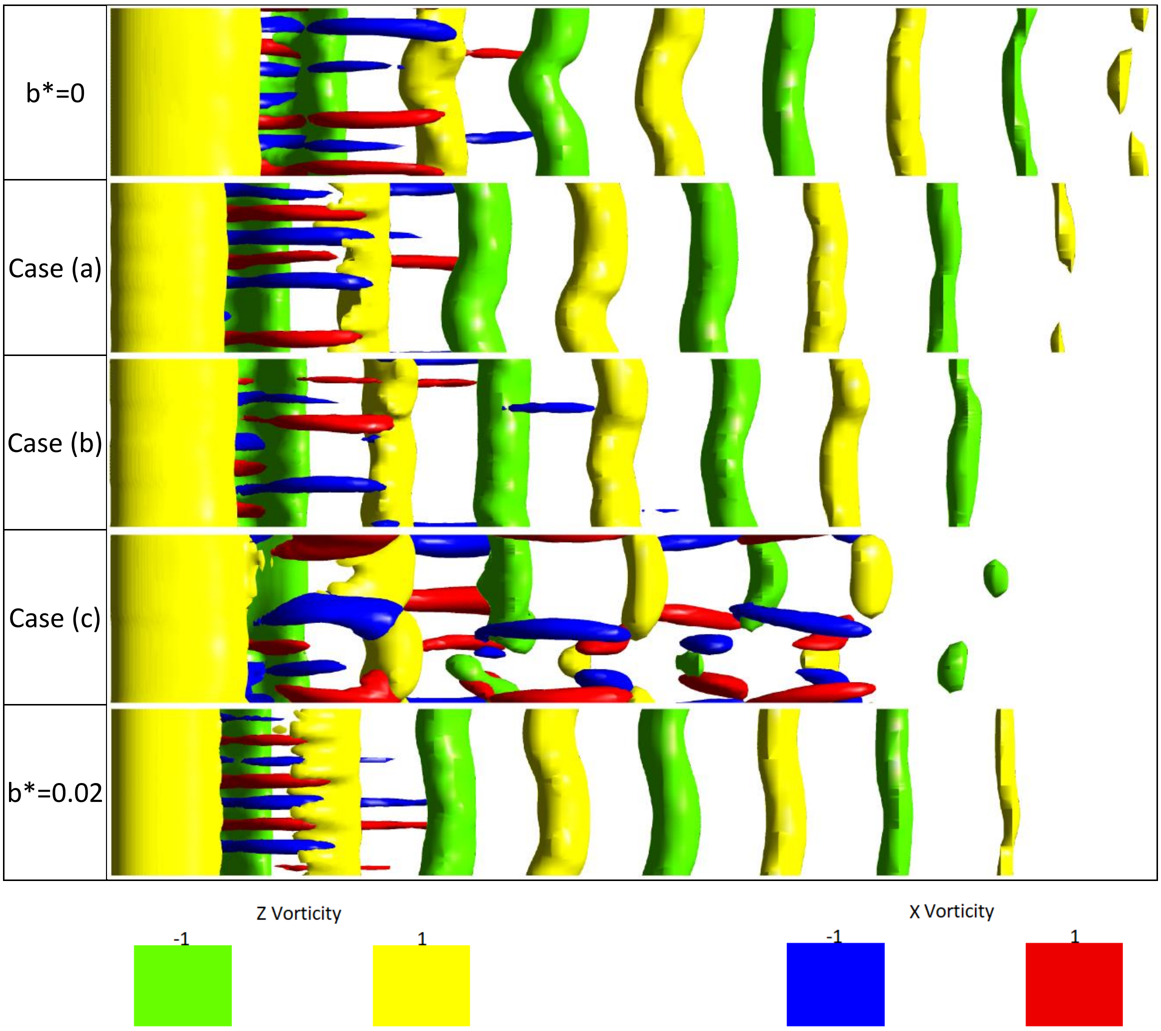

Fig. 37: Snapshots of instantaneous isosurfaces of spanwise (ω_Z) and streamwise (ω_X) vorticity for each slip length considered. The uncontrolled case (b*=0) and the full slip case (b*=0.02) are included.

6.2 Heat transfer

As the regards the rates of heat transfer, figure 38 presents the time average *Nu* versus the percentage of hydrophobic area, for each case considered. Similar with the characteristic integral flow quantities, presented in previous section, the cases (a) and (b) presents results close two the midline of the results of uncontrolled and full slip cases. However, case (c) displays slightly lower *Nu* value which indicates that the flow destabilization affects negatively the rate of heat transfer. This is expected because *Nu* decreases when the three-dimensionality of the flow increases. This behavior is also illustrated in figure 32 which presents the comparison between the 2D and 3D results. There, the largest deviation occurs for the case that produce the greater three-dimensionality in the wake (i.e. b*=0.05). Finally, it should be noted that the reduction of *Nu* is not significant because its value is still 4% higher than that of the uncontrolled case.

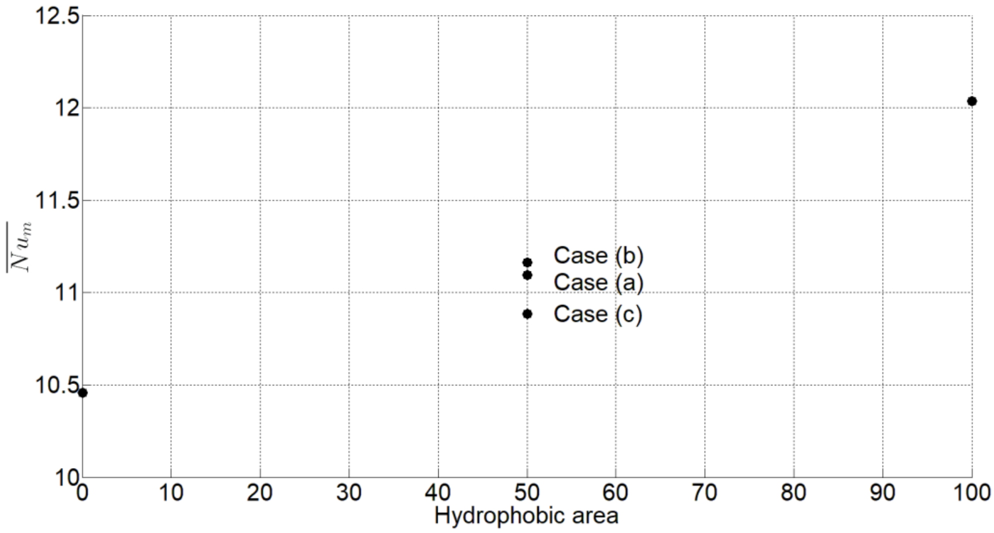

Fig. 38: Time average *Nu* versus the percentage of hydrophobic area (full slip and no-slip cases are included).

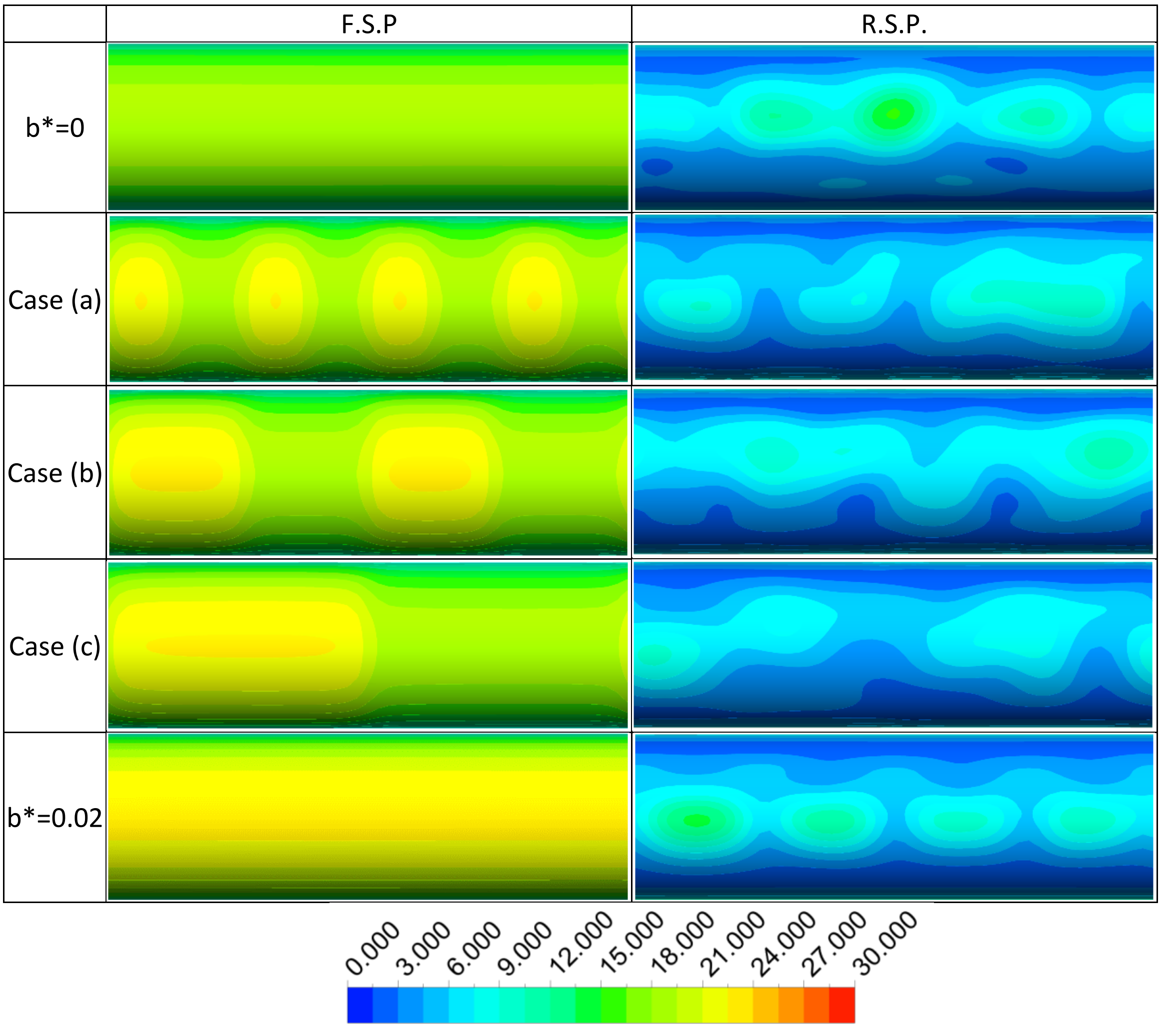

Fig. 39: Snapshots of instantaneous *Nu* distribution for each case considered (full slip and no-slip cases are included).

Furthermore, figure 39 presents snapshots of instantaneous Nu distribution on cylinder surface for each case considered. Here, it should be noted that the left column corresponds to the region around the front stagnation line, while the right column to the region around the rear stagnation line (covering a range of 180 deg. each). Regarding the distribution of *Nu* at the regions around the front stagnation line, it is clear that *Nu* displays higher values in the hydrophobic regions and significantly smaller in non-hydrophobic regions. In addition, none of the considered cases presents a clear advantage against the others, which partially explains the similar values of time average *Nu*. This behavior is attributed to the fact that the considered region is located earlier than the separation point and it is not affected by the structure of the wake. On the other hand, the distribution of *Nu* at the rear stagnation region shown lower independency from the arrangements of hydrophobic bands. In more detail, *Nu* displays slightly higher values in hydrophobic areas than in non-hydrophobic. The cause of this behavior is the three-dimensionality of the flow in this region. Finally, it is worth to mention that, in this region, the cases with bands presents lower *Nu* values than the uncontrolled and full slip cases.

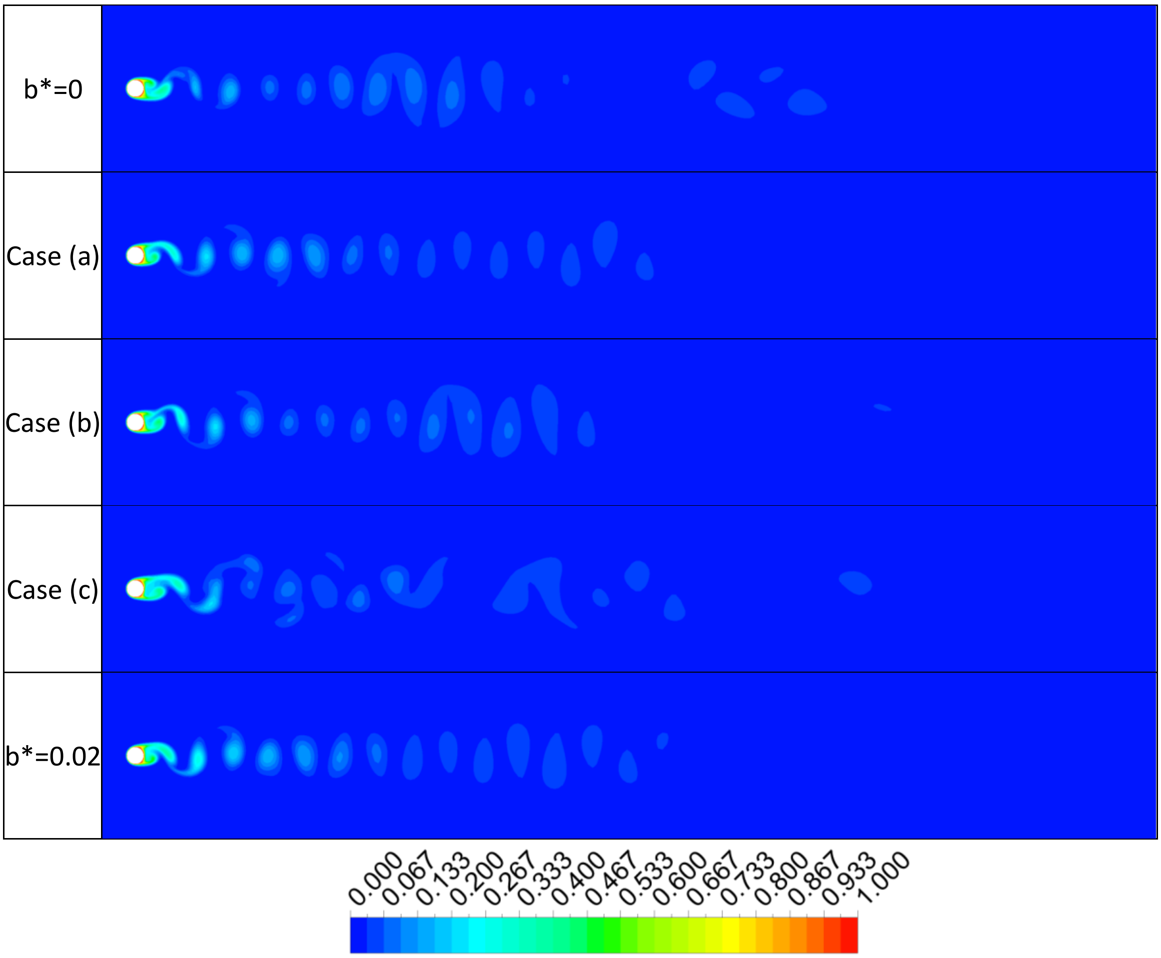

Fig. 40**:** Snapshots of instantaneous temperature distribution at XY plane for each case considered (full slip and no-slip cases are included).

Finally, figure 40 and 41 present the instantaneous temperature distribution at an XY plane and the instantaneous isosurfaces of temperature equal to 0.04, respectively. As stated in the previous chapter, temperature distribution follows similar structure with the vorticity distribution. In more detail, all cases except the case (c) present similar temperature distribution in the wake. As shown in figure 41, the temperature isosurfaces present cylindrical shape in the far wake because in this region only the primary vorticies are strong. In the region close to the cylinder, the iso-temperature tubes are connected due to the strong streamwise vorticity and the formation of vortex loops. On the other hand, case (c) presents a totally different image. This temperature distribution is similar with those of full slip case and b^*=0.05 which presents the same shedding mode. However, the concentration of high temperature in a line may be associated with the presence of the hydrophobic band. In other words, the hydrophobic band, suppressing the unsteadiness in this region, may lead to milder flow mixing, which results in lower heat transfer rates in this region.

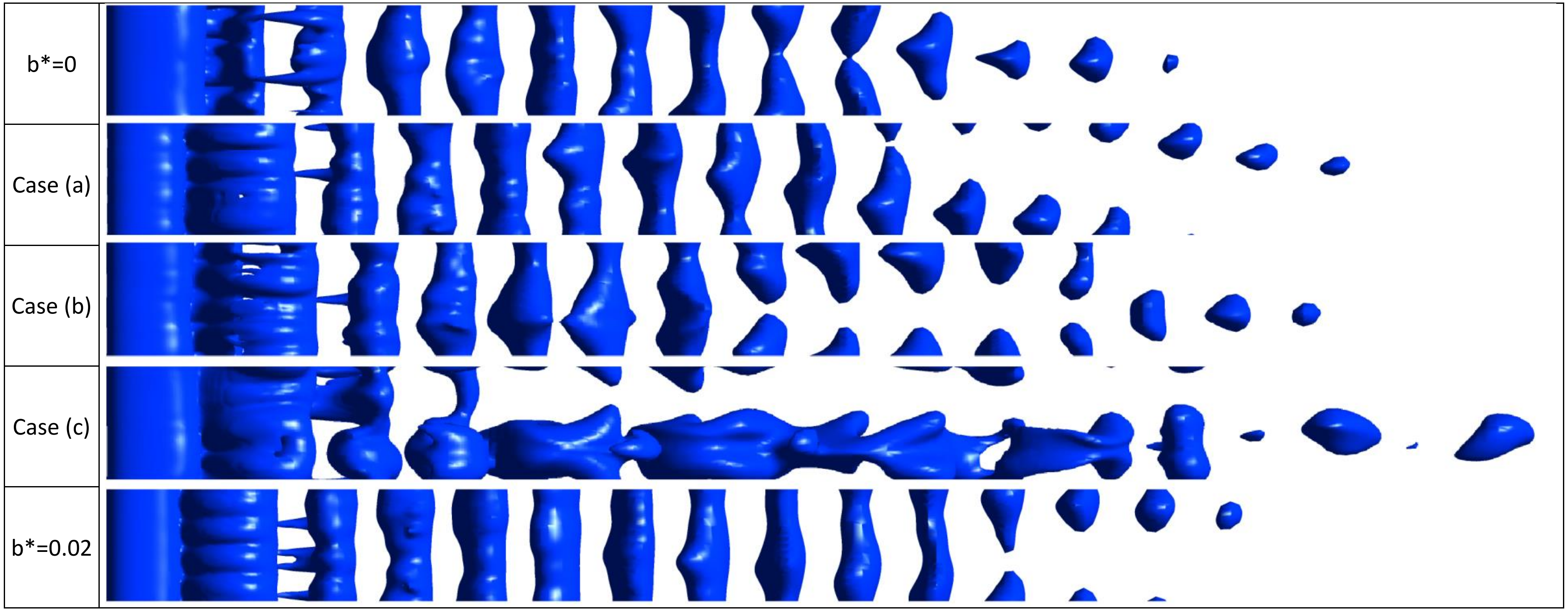

Fig. 41: Snapshots of instantaneous isosurfaces of temperature T=0.04 for each case considered (full slip and no-slip cases are included).

7 Implementation of partial spanwise uniform hydrophobicity

In the present chapter, the effects of partial spanwise uniform hydrophobicity on the cylinder surface were investigated. Similar with the previous chapter, the numerical simulations were performed for *Re*=300 and non-dimensional slip length equal to 0.02. Here, three case were considered (fig.42): (a) implementation of hydrophobicity only on the front stagnation region, for a hydrophobic area extending ±45 deg. from the front stagnation line, (b) implementation of hydrophobicity on the front half of the cylinder (i.e. hydrophobicity extending ±90 deg. from the frond stagnation line), and (c) implementation of hydrophobicity on the entire cylinder surface excluding the region extending ±45 deg. from the rear stagnation line. In these three cases, the percentage of hydrophobic area to total area of the cylinder was 20%, 50% and 75%, respectively. According to Kafarakis et al. (2016), Mastrokalos (2016), and Mastrokalos and Kaiktsis (20017), absence of hydrophobicity at the rear stagnation region may lead to similar results with the full slip case regarding the integral flow quantities and heat transfer rates. Taking this fact into account, the aim of the present simulations is to investigate whether a further reduction of hydrophobic area could lead to equivalent results.

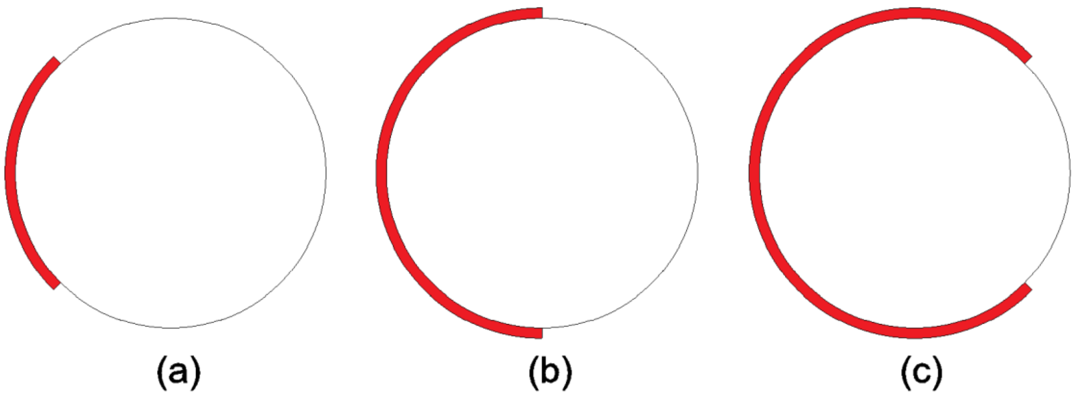

Fig. 42**:** Sketch of surface hydrophobicity patterns for the cases of the present study; red and white areas correspond to hydrophobic and non-hydrophobic regions, respectively.

7.1 Flow structure

Figure 43 presents the time average drag coefficient (fig. 43a), the amplitude of lift (fig.43b) and drag (fig.43c) coefficient and the shedding frequency in terms of *St* versus the percentage of hydrophobic area. Similar with the previous chapter, in order to evaluate the effectiveness of arrangement the uncontrolled and the full slip cases are included. As shown in figure 43a, case (a) presents slightly higher drag than the uncontrolled case. This is attributed to the fact the downstream end of the hydrophobic area increase the flow instability. Moreover, in this region flow abruptly slows down, which results in the increase of

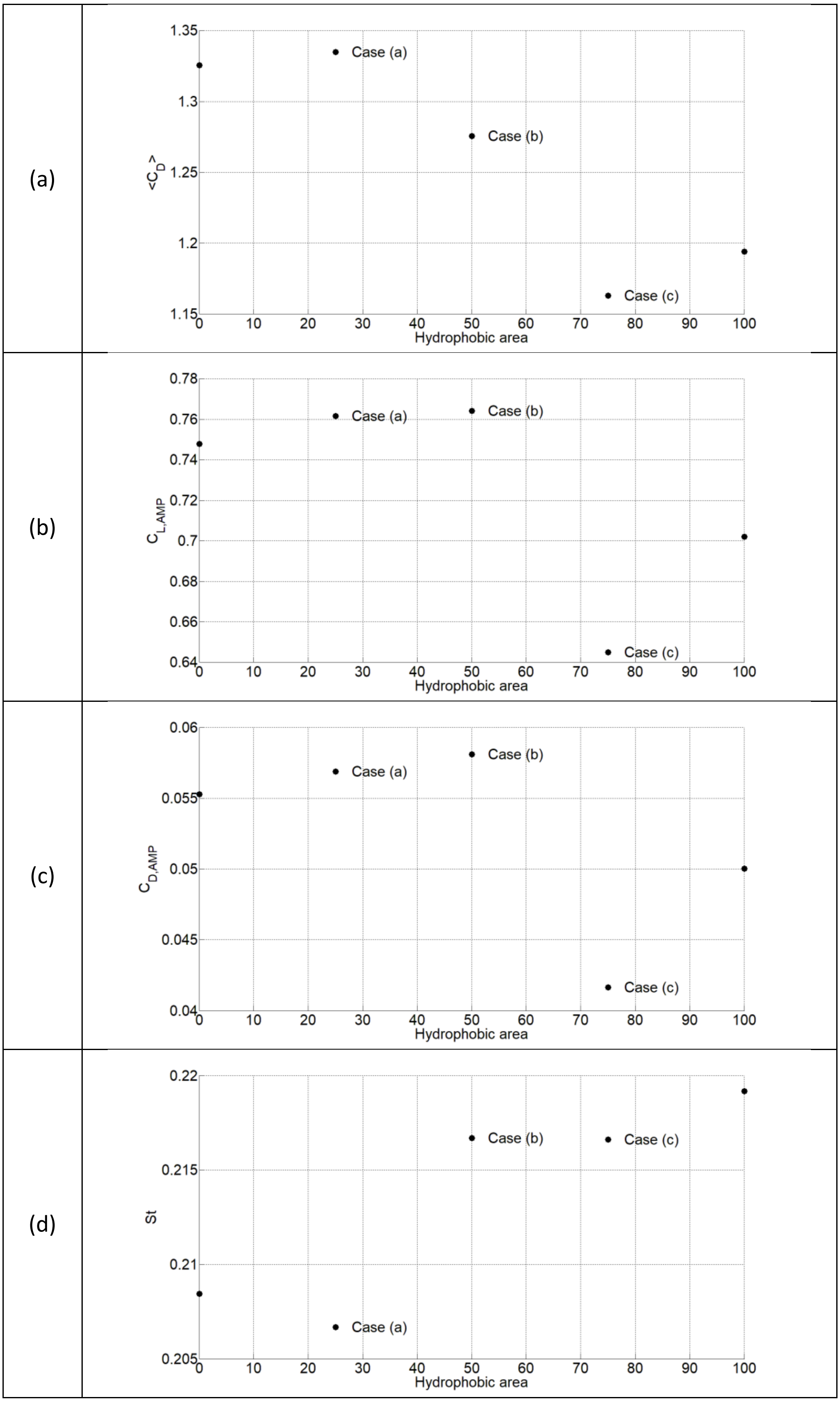

Fig. 43: Results of partial hydrophobicity implemented on cylinder (full slip and no-slip cases are included). (a) Time average drag coefficient, (b) lift coefficient amplitude, (c) drag coefficient amplitude, (d) Strouhal number, versus the percentage of hydrophobic area.

pressure. This pressure increase combined with the reduction of pressure at the rear stagnation region due to flow instability causes the total increase of drag. On the other hand, case (b) presents results close to the middle of results of uncontrolled case and full slip case. Finally, case (c) displays a large reduction at drag, as the its value is 12% lower than that of uncontrolled case and close to 3% lower than that of the full slip case. This is due to same separation point angle with the full slip case (the separation point angle of full slip case is higher than that of uncontrolled case) and the relatively lower velocities at the rear stagnation region. In other words, absence of hydrophobicity at the rear stagnation region results in the increase of pressure, which leads to drag reduction. Moreover, case (c) achieves better stabilization of the flow than the full slip case. This phenomenon has the same explanation with the drag reduction, and it is clearly illustrated in figures 43b and 43c. In particular, case (c) presents 8% reduction in lift amplitude and 17% reduction in drag amplitude from the full slip case. On the other hand, as stated before, the two other cases destabilize the flow causing the increase of lift and drag amplitudes. Finally, the lower shedding frequency is presented by the case (a), and it may be related to the shedding mode.

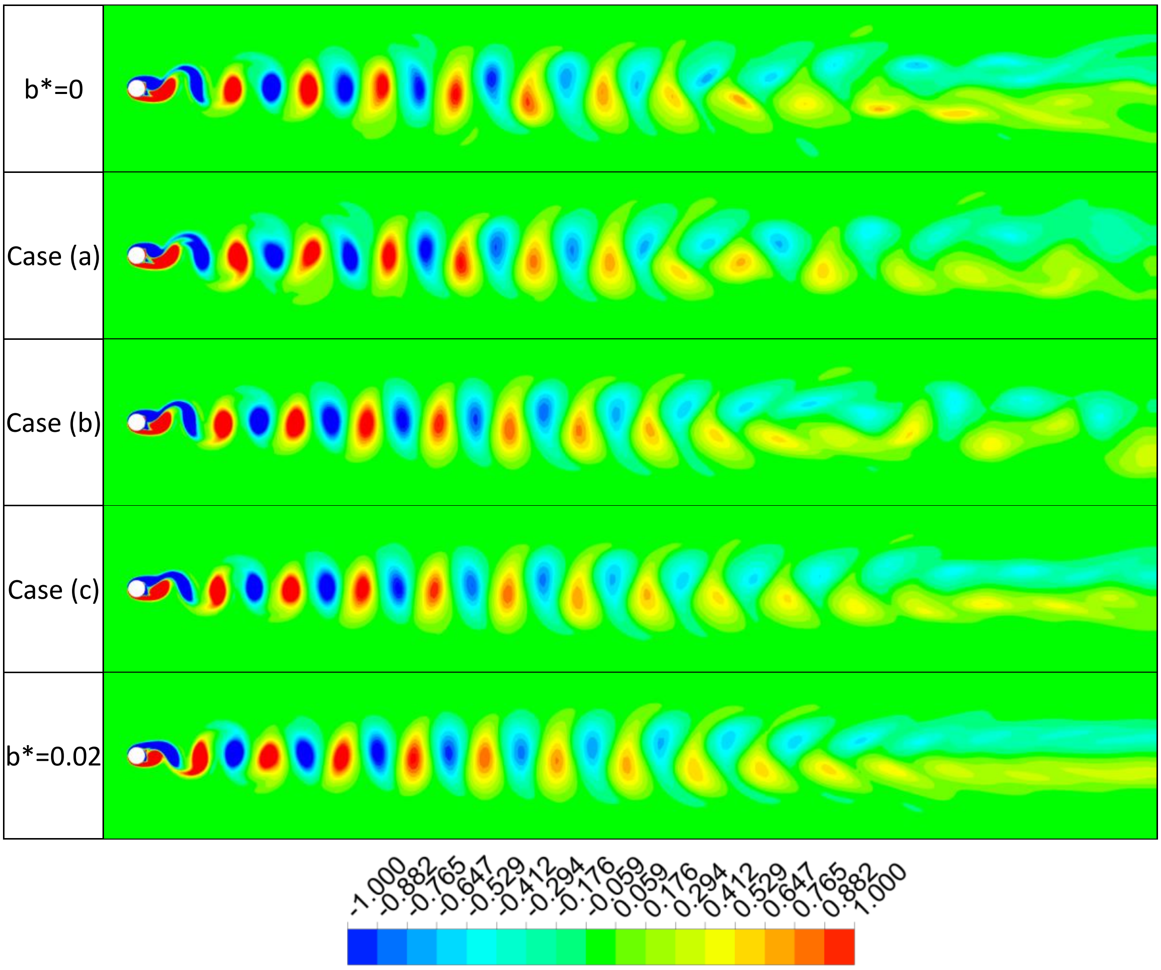

Fig. 44: Snapshots of instantaneous spanwise vorticity (ω_Z) at an XY plane for each case considered. The uncontrolled case (b*=0) and the full slip case (b*=0.02) are included.

Furthermore, figures 44 and 45 visualize the flow structure in terms of color-coded contours of spanwise vorticity and isosurfaces of spanwise and streamwise vorticity. As shown in figure 44, the three cases exhibit similar structure, with some small variations. As regards the 3D flow structure (fig.45), all cases display the same shedding mode (i.e. mode B with spanwise wavelength equal to $\lambda_Z=\pi D/4$) except case (a). In particular, in case (a), the spanwise wavelength is close to $\lambda_Z=\pi D/3$, which denotes that this arrangement of hydrophobicity increases not only the instability of the flow at XY planes but also the instability in the Z direction. Finally, it should be noted that the domain used may not be able to predict accurately the flow structure of case (a), as the streamwise vorticies at the periodic boundary of the domain present an unexpected deformation.

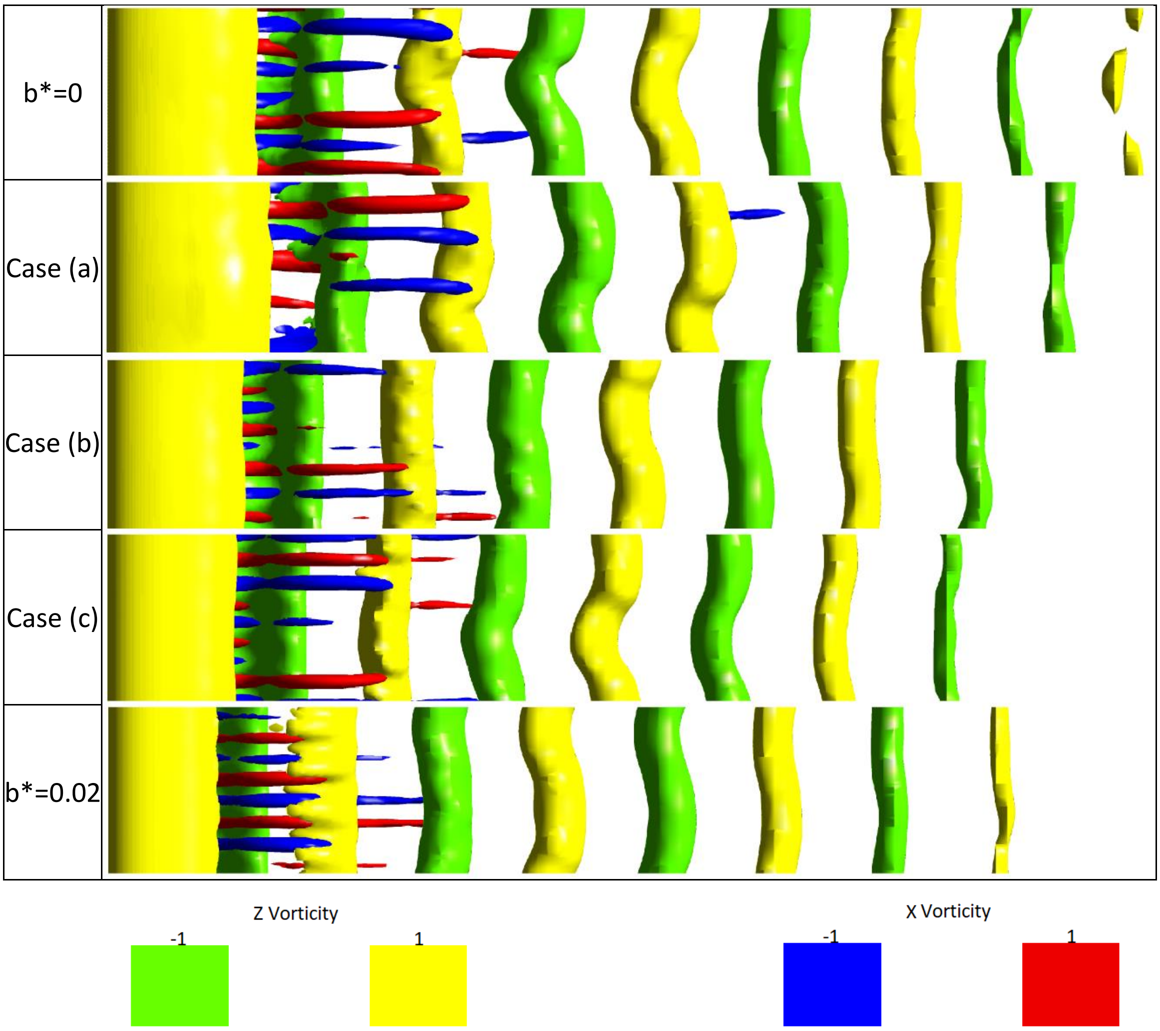

Fig. 45**:** Snapshots of instantaneous isosurfaces of spanwise (ω_Z) and streamwise (ω_X) vorticity for each slip length considered. The uncontrolled case (b*=0) and the full slip case (b*=0.02) are included.

7.2 Heat transfer

Figure 46 presents the time average *Nu* versus the percentage of hydrophobic area. Case (a) presents results close to the line connecting the results of uncontrolled case and full slip case. This means that the arrangement of case (a) does not achieve increased heat transfer rates. On the other hand, case (b) achieves a large increase. This is due to the relatively high mixture of the flow at the rear stagnation region because of the flow instability. Finally,

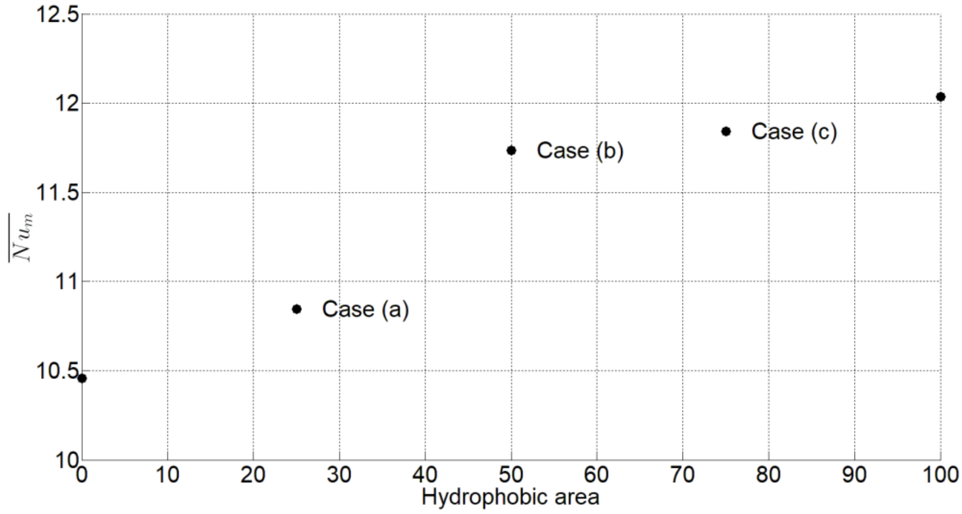

Fig. 46**:** Time average *Nu* versus the percentage of hydrophobic area (full slip and no-slip cases are included).

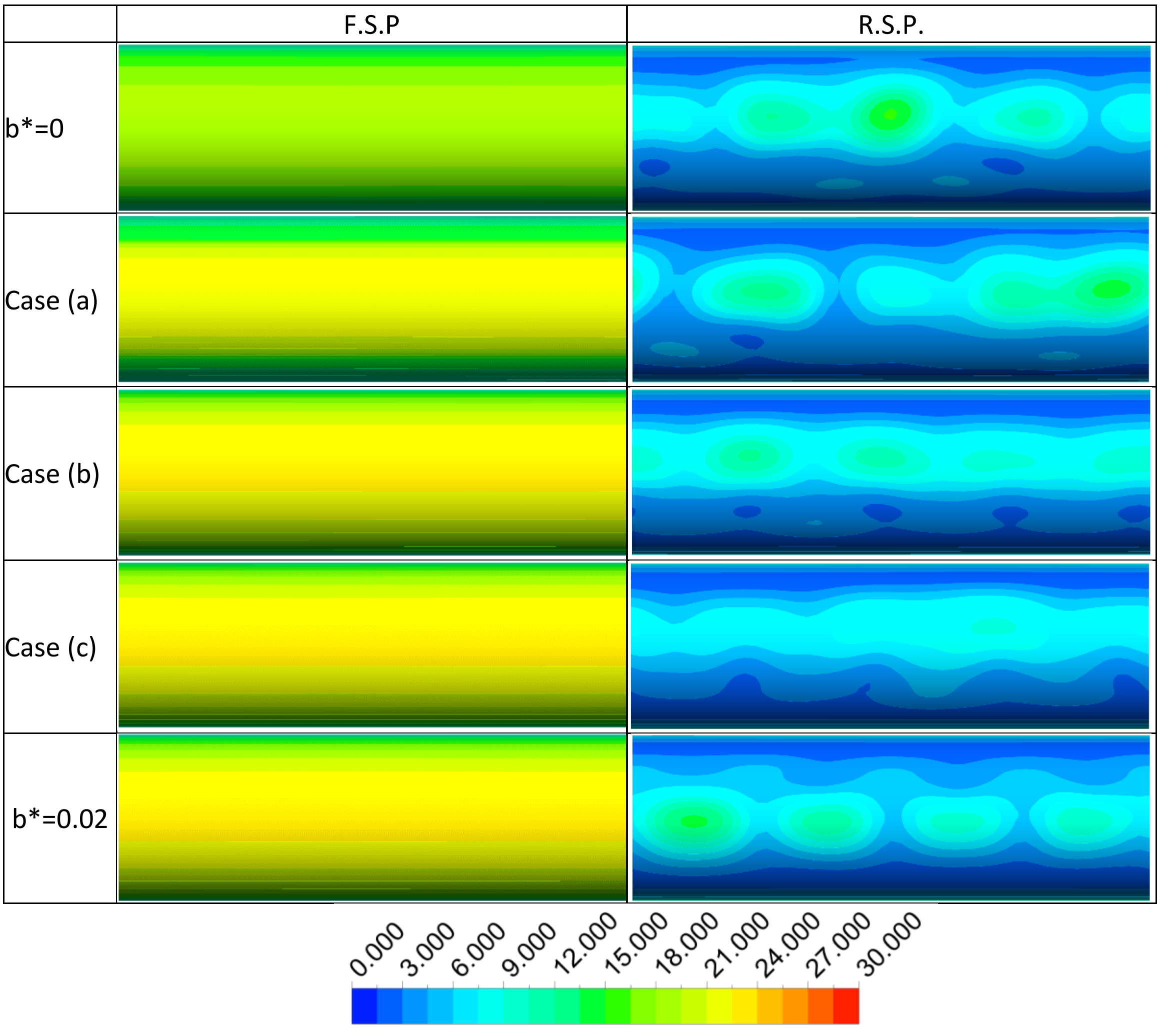

Fig. 47**:** Snapshots of instantaneous *Nu* distribution for each case considered (full slip and no-slip cases are included).

case (c) presents an intermediate heat transfer enhancement as the flow instability in this case is relatively low.

As regards the distribution of *Nu* over the cylinder, figure 47 presents snapshots of instantaneous *Nu* for each case considered. At the front stagnation region, all cases display similar distribution with the full slip case. However, at the rear stagnation region, the cases considered present deviation from both uncontrolled and full slip cases. In more detail, case (a) presents spot of high *Nu*, similar with uncontrolled case, which denotes that close to the cylinder flow has wavelength equal to $\lambda_z=\pi D/4$. Moreover, case (b) and case (c) exhibit a more uniform spanwise distribution of *Nu* because of the less intense instability in the Z direction.

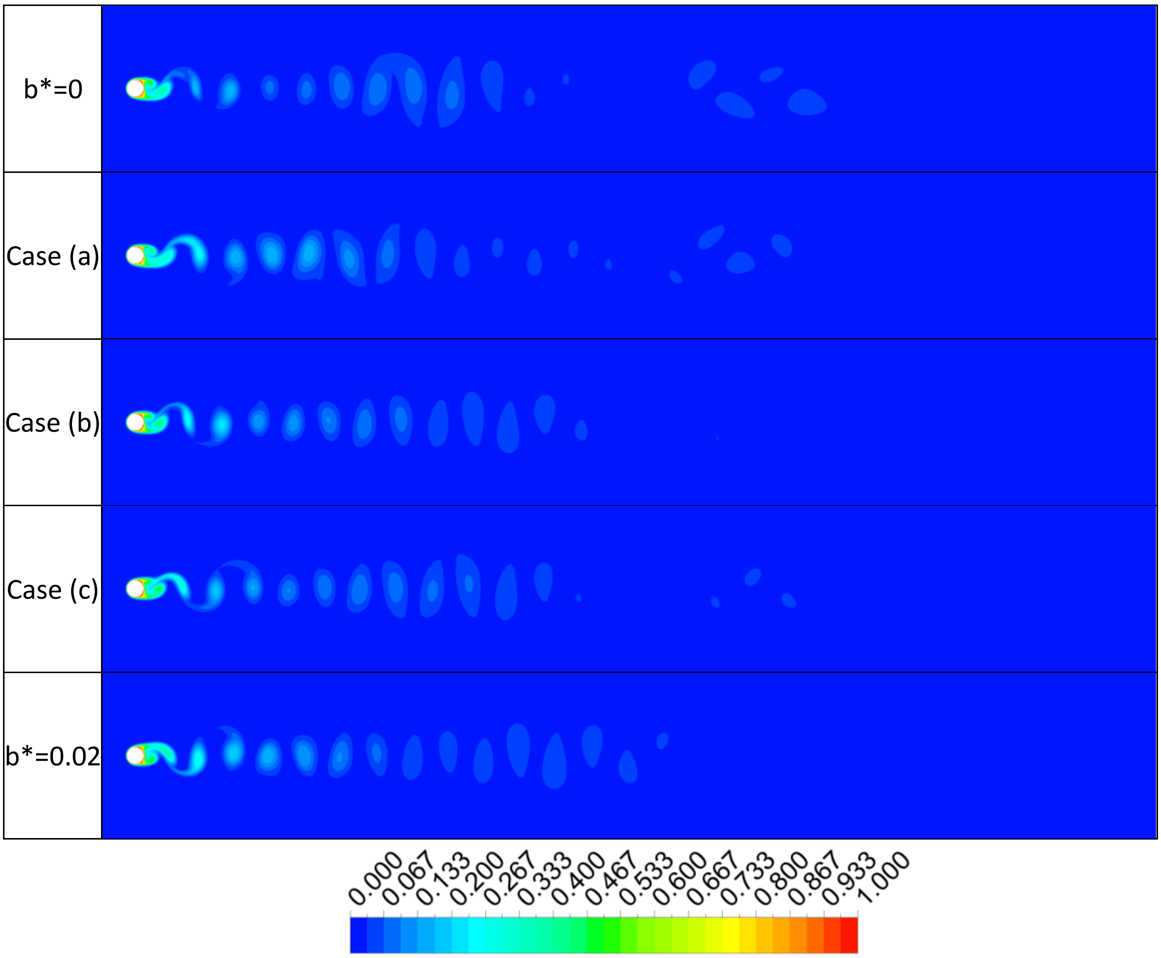

Fig. 48**:** Snapshots of instantaneous temperature distribution at XY plane for each case considered (full slip and no-slip cases are included).

Finally, figures 48 and 49 present the instantaneous temperature distribution at an XY plane and the instantaneous isosurfaces of temperature equal to 0.04, respectively. Here, it is clear that the distribution of temperature is almost identical in all cases. In particular, the figures illustrate that case (a), which induces flow instability in the Z direction, achieves better heat transfer in the wake due to the increased flow mixing.

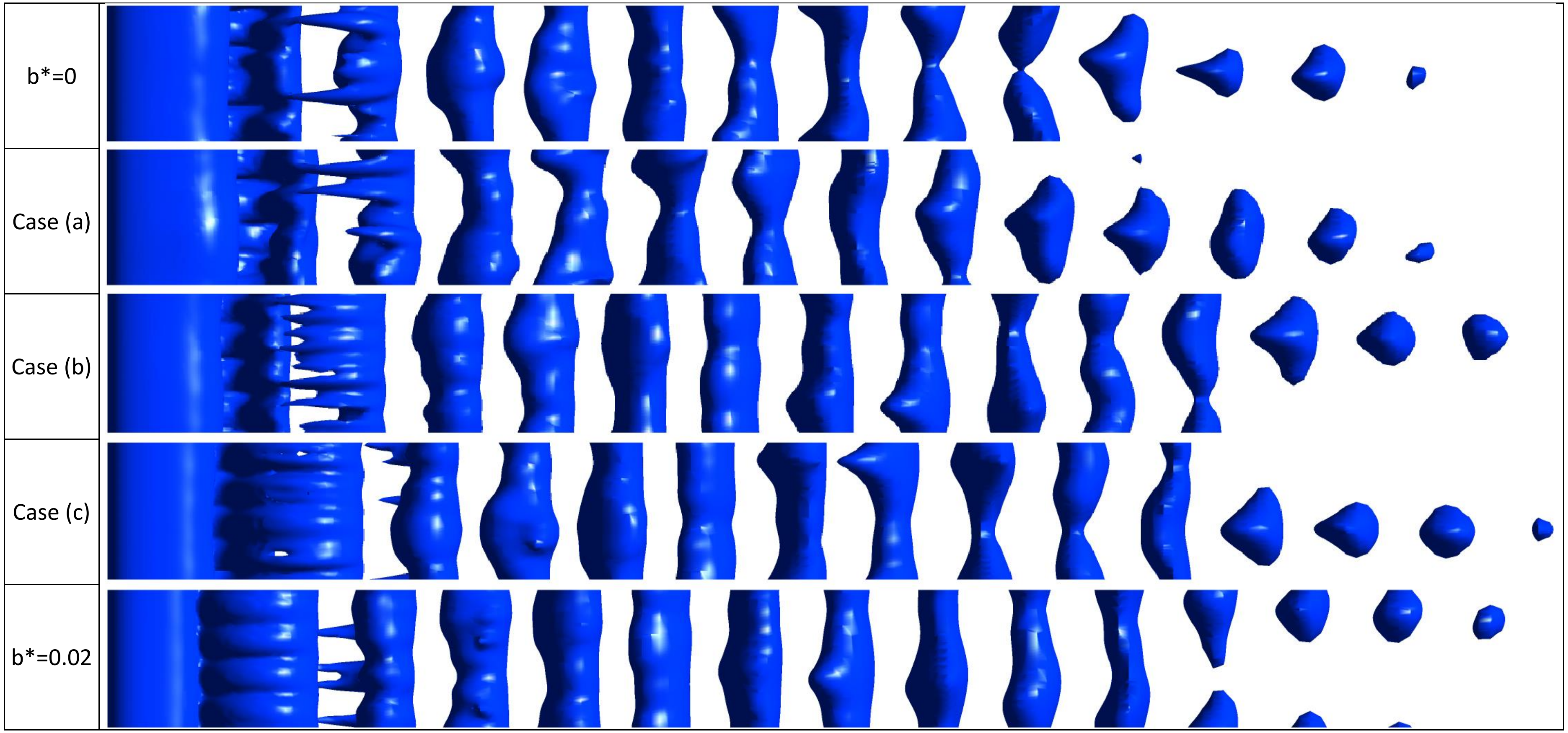

Fig. 49: Snapshots of instantaneous isosurfaces of temperature T=0.04 for each case considered (full slip and no-slip cases are included).

8 Conclusions – Suggestions for future work

The present study has investigated the effects of hydrophobicity on a circular cylinder surface on flow structure, characteristic integral flow quantities and heat transfer via 3-D time-dependent numerical simulations for low *Re*.

After an extensive investigation on spatial and temporal discretization, it was found that a grid with 50000 elements in the x-y plane and a numerical time step equal to Δt=0.01 can accurately predict all the associated phenomena of the cylinder wake for all *Re* values considered in the present study. Moreover, is was found that a computational domain extending πD in the z direction can sufficiently predict the correct shedding mode.

As regards the effects of hydrophobicity, first, hydrophobicity was implemented on the entire cylinder surface. It was demonstrated that increase of slip length leads to suppression of flow unsteadiness, and enhances heat transfer. In more detail, increase of slip length results in the reduction of effective *Re* because flow displays structures which corresponds to lower *Re*. However, it was noted that, at high values of slip length, integral flow quantities and heat transfer rates approach limit values, since the increase of slip length returns a negligible improvement in the considered quantities.

Next, in order to investigate how different spatial distributions of hydrophobicity affect the flow structure and heat transfer rates, alternating circumferential bands of slip and no-slip condition were implemented. It was found that these arrangements of hydrophobicity increase flow three-dimensionality, resulting in great reduction of time-averaged drag, and lift and drag amplitudes. In particular, bands with width equal to $2\lambda_z$, triggering the mode A, can achieve 15% reduction in time-averaged drag and 52% reduction in lift amplitude. However, the effects of this arrangement on heat transfer rates are not significant, as it can achieve 4% increase of *Nu*.

Finally, the effects of partial spanwise uniform hydrophobicity were investigated. It was found that implementation of hydrophobicity on the entire cylinder surface excluding the rear stagnation region can achieve improvements at all considered quantities. In more detail, this arrangement achieves 12% reduction of time-averaged drag coefficient, 14% reduction of lift amplitude and 13% increase of time averaged *Nu*.

Suggestions for future work mainly include extensions of the present work for high *Re*. This is of paramount importance as the heat exchangers operate at higher *Re* than those of the present study. However, this extension is not a straightforward procedure because at high *Re* the boundary layer becomes turbulent and the gradient of velocity near the wall is very large. Thus, the assumption of slip length being independence from shear rates is not valid. On the other hand, an optimization approach could be used in order to find arrangements of hydrophobicity which lead to additional improvement of heat transfer rates and flow stability. However, this method demands a large number of numerical simulation, and thus very powerful computational resources.

9 References

Abu-Nada E., Ziyad K., Salen M. & Ali Y. 2008. Heat transfer enhancement in combined convection around a horizontal cylinder using nanofluids. *J. Heat Transfer (2008), vol.130 / 084505.*

Apelt C. J., West G. S. & Szewczyk A. A. 1973. The effects of wake splitter plates on the flow past a circular cylinder in the range $10^4 < R < 5{\cdot}10^4$. *J. Fluid Mech, vol. 61, pp. 187-198*

Apelt C. J. & West G. S. 1975. The effects of wake splitter plates on the flow past a circular cylinder in the range $10^4 < R < 5{\cdot}10^4$ Part 2. *J. Fluid Mech.(1975), vol. 71, pp.145-160.*

Bovand M., Rashidi S., & Esfahani J.A. 2015. Enhancement of heat transfer by nanofluids and orientations of the equilateral triangular obstacle. *Energy Conversion and Management 97 (2015) 212–223.*

Cardel G.S. 1973. Flow Past a circular cylinder with a permeable wake splitter plate. *California Institute of Technology Pasadena, California.*

Chen W.L., Gao D.L., Yuan W.Y., Li H. & Hu H. 2015. Passive jet control of flow around a circular cylinder. *Exp Fluids (2015) 56:201.*

Chen W.L., Gao D.L., Li H. & Hu H. 2017. A Passive method to control the wake flow behind a circular cylinder. *American Institute of Aeronautics and Astronautics, Inc.*

Churchill S.W. & Bernstein M. 1977. A correlating equation for forced convection from gases and liquids to a circular cylinder in cross flow. *ASME J. Heat Transfer 99 (1977) 300–306.*

Delaunay Y. & Kaiktsis L. 2001. Control of circular cylinder wakes using base mass transpiration. *Physics of Fluids 13, 3285 (2001).*

Dong S., Triantafyllou G.S. & Karniadakis G.E. 2008. Elimination of vortex streets in bluff-body flows. *Physical Review Letters, 100, 20, 204501.*

Evangelinos C, & Karniadakis GE. 1999. Dynamics and flow structures in the turbulent wake of rigid and flexible cylinders subject to vortex-induced vibrations. *J Fluid Mech 1999; 400: 91–124.*

Fey U., Konig M. & Eckelmann H. 1998. A new Strouhal–Reynolds-number relationship for the circular cylinder in the range $47<Re<2{\cdot}10^5$. *Physics of Fluids 13, num. 7, July 1998.*

Bergman T. L., Lavine A. S., Incropera F. P. & Dewitt D. P. 2011. Fundamentals of Heat and Mass Transfer. *978-0470-50197-9.*

Haase A. S., Chapman S. J., Tsai P. A.,Lohse D. & Lammertink R. G. H. 2015. The Graetz-Nusselt problem extended to continuum flows with finite slip. *J. Fluid Mech. (2015), vol. 764, R3*.

Hammache M. & Gharib M. 1991. An experimental study of the parallel and oblique vortex shedding from circular cylinders. *J. Fluid Mech. (1991), vol. 232, p p . 567-590.*

Henderson R. D. 1995. Details of the drag curve near the onset of vortex shedding. *Phys. Fluids, Vol. 7, No. 9, September 1995.*

Homescu C., Navon I. M. & Li Z. 2002. Suppression of vortex shedding for flow around a circular cylinder using optimal control. *Int. J. Numer. Meth. Fluids 2002; 38:43–69.*

Igarishi T. & Tsutsui T. 1992. Flow control around a circular cylinder by a small cylinder. *11th Australasian Fluid Mechanics Conference University of Tasmania, Hobart, Australia 14-18 December 1992.*

Jonathan P. R. 2009. Slip on superhydrophobic surfaces. *Annu. Rev. Fluid Mech. 2010. 42:89–109.*

Kafarakis S. T., Mastrokalos M. E., Papadopoulos C. I. & Kaiktsis L. 2016. Heat transfer enhancement for heat exchanger applications: use of surface hydrophobicity. *ASME 2016 Pressure Vessels and Piping Conference, Volume 4, Paper 63899.*

Kahwaji G. & Ali O. M. 2015. Numerical investigation of natural convection heat transfer from square cylinder in an enclosed enclosure filled with nanofluids. *Rochester Institute of Technology RIT Scholar Works.*

Kaiktsis L., Triantafyllou G. S., & Ozbas M. 2007. Excitation, inertia, and drag forces on a cylinder vibrating transversely to a steady flow. *Journal of Fluids and Structures 23 (2007) 1–21.*

Kang S. & Choi H. 1999. Laminar flow past a rotating circular cylinder. *Phys. Fluids, Vol. 11, No. 11, November 1999.*

Kim T. S. & Kim J. S. 2010. Numerical analysis of the three-dimensional wake flow and acoustic field around a circular cylinder. *Int'l J. of Aeronautical & Space Sci. 11(4), 319–325 (2010).*

Labbe D. F. L. & Wilson P. A. 2007. A numerical investigation of the effects of the spanwise length on the 3-D wake of a circular cylinder. *Journal of Fluids and Structures 23 (2007) 1168–1188.*

Legendre D., Lauga E. & Magnaudet J. 2009. Influence of slip on the dynamics of two-dimensional wakes. *J. Fluid Mech. (2009), vol. 633, pp. 437–447.*

Li G., Zheng Y., Hu G., Zhang Z. & Xu Y. 2016. Experimental study of the heat transfer enhancement from a circular cylinder in laminar pulsating cross-flows. *Heat Transfer Engineering, 37(6):535–544, 2016.*

Li G., Zheng Y., Yang H. & Xu Y. 2015. Numerical investigation of heat transfer and fluid flow around the rectangular flat plane confined by a cylinder under pulsating flow. *Journal of Applied Fluid Mechanics, Vol. 9, No. 4, pp. 1569-1577, 2016.*

Mastrokalos M. E. 2016. Application of control methods to fluid mechanics problems: flow past a cylinder. *PhD Thesis, National Technical University of Athens 2016*.

Mastrokalos M. E. & Kaiktsis L. 2017. Heat transfer enhancement in three-dimensional flow past a hydrophobic cylinder for heat exchanger applications. *ASME 2017 Pressure Vessels and Piping Conference Vol. 4, paper 65525.*

Mastrokalos M. E., Papadopoulos C. I. & Kaiktsis L. 2015. Optimal stabilization of a flow past a partially hydrophobic circular cylinder. *Computers & Fluids 107, 256–271.*

Maynes D., Webb B. W. & Davies J. 2008. Thermal transport in a microchannel exhibiting ultrahydrophobic microribs maintained at constant temperature. *Journal of Heat Transfer, ASME February 2008, Vol. 130 / 022402.*

McDonald P. & Persoons T. 2017. Numerical characterisation of active drag and lift control for a circular cylinder in cross-flow. *Appl. Sci. 2017, 7, 1166.*

Mittal S. & Kumar B. 2003. Flow past a rotating cylinder. J. *Fluid Mech. (2003), vol. 476, pp. 303-334.*

Mittal S. & Raghuvanshi A. 2001. Control of vortex shedding behind circular cylinder for flows at low Reynolds numbers. *Int. J. Numer. Meth. Fluids 2001; 35: 421-447.*

Nakamura H. & Igarashi T. 2004. Variation of Nusselt number with flow regimes behind a circular cylinder for Reynolds numbers from 70 to 30000. *Int. J. Heat Mass Transfer 2004, 47:5169-5173.*

Oruc V. 2012. Passive control of flow structures around a circular cylinder by using screen. *Journal of Fluids and Structures 33 (2012) 229–242.*

Oruc V., Akilli H. & Sahin B. 2016. PIV measurements on the passive control of flow past a circular cylinder. *Experimental Thermal and Fluid Science 70 (2016) 283–291.*

Ozkan G. M., Oruc V., Akilli H. & Sahin B. 2012. Flow around a cylinder surrounded by a permeable cylinder in shallow water. *Exp Fluids (2012) 53:1751–1763.*

Patnana V. K., Bharti R. P. & Chhabra R. R. 2009. Two-dimensional unsteady flow of power-law fluids over a cylinder. *Chemical Engineering Science 64 (2009) 2978-2999.*

Patnana V. K., Bharti R. P. & Chhabra R. R. 2010. Two-dimensional unsteady forced convection heat transfer in power-law fluids from a cylinder. *International Journal of Heat and Mass Transfer 53 (2010) 4152–4167.*

Peppa S. 2012. Computational study of flow-structure interaction. *PhD Thesis, National Technical University of Athens 2012.*

Rios F. 2011. Hydrophobicity and its applications. *PhD Thesis, New Mexico State University Las Cruces New Mexico 2011.*

Roshko A. 1954. On the drag and shedding frequency of two-dimensional bluff bodies. *National advisory committee for aeronautics, Technical note 3169.*

Sheikholeslami M., Gorji-Bandpy M. & Ganji D. D. 2015. Review of heat transfer enhancement methods: Focus on passive methods using swirl flow devices. *Renewable and Sustainable Energy Reviews 49 (2015) 444–469.*

Strykowski P.J. and Sreenivasan P.R. 1990. *On the formation and suppression of vortex 'shedding' at low Reynolds numbers*. Journal of Fluid Mechanics 218, 71-107,

Thompson M. C., Leweke T. & Williamson C. H. C. 2000. The physical mechanism of transition in bluff body wakes. *Journal of Fluids and Structures (2001) 15, 607-616.*

Tokumaru P.T. & Dimotakis P.E. 1990. Rotary oscillation control of a cylinder wake. *J . Fluid Mech. (1991), vol. 224, pp. 77-90.*

Turk A. Y. 1984. Heat transfer enhancement downstream of vortex generators on a flat plate. *PhD Thesis, Iowa State University 1984.*

Unal M. F. & Rockwell D. 1988. *On vortex formation from a cylinder. Part 2. Control by splitter-plate interference*. Journal of Fluid Mechanics 190, 513-529.

Van Dyke, M., An Album of Fluid Motion.

Vegada M., Satadiab S., Pradipb P., Chiragb P. & Bhargavb P. 2014. Heat transfer characteristics of low Reynolds number flow of nanofluid around a heated circular cylinder. *Procedia Technology 14 (2014) 348 – 356.*

Voronov R. S., Papavassiliou D. V. & Lee L. L. 2007. Slip length and contact angle over hydrophobic surfaces. *Chemical Physics Letters 441 (2007) 273–276.*

Wijayanta A. T., Istanto T., Kariya K. & Miyara A. 2017. Heat transfer enhancement of internal flow by inserting punched delta winglet vortex generators with various attack angles. *Experimental Thermal and Fluid Science 87 (2017) 141–148.*

Williamson C. H. K. 1989. Oblique and parallel modes of vortex shedding in the wake of a circular cylinder at low Reynolds numbers*. J. Fluid Mech. (1989), vol. 206, pp. 579—627.*

Williamson C. H. K. 1995a. Three-dimensional wake transition behind a cylinder*. J. Fluid Mech. Volume 328, 1996, pp. 345-407*

Williamson C. H. K. 1996. Vortex dynamics in the cylinder wake. *Annu. Rev. Fluid. Mech. 1996.28:477-539.*

You D. & Moin P. 2007. Effects of hydrophobic surfaces on the drag and lift of a circular cylinder. *Physics of Fluids, 19, 081701, (2007).*

Zhang R., Di Q., Wang X., Ding W. & Gong W. 2012. Numerical study of the relationship between apparent slip length and contact angle by lattice Boltzmann method. *Journal of Hydrodynamics, 2012, 24(4):535-540.*

Zhang W., Meng G. & Wei X. 2012. A review on slip models for gas microflows. *Microfluid Nanofluid (2012) 13:845–882*